T.R.
GEBZE TECHNICAL UNIVERSITY
GRADUATE SCHOOL OF NATURAL AND APPLIED SCIENCES

REACTIVE SINTERING OF TiC-BASED CERMETS BY USING IRON, TITANIUM AND CARBON POWDERS

MAMMADHUSEYN MAMMADZADA
A THESIS SUBMITTED FOR THE DEGREE OF
MASTER OF SCIENCE
DEPARTMENT OF MATERIALS SCIENCE AND ENGINEERING

GEBZE
2021

T.R.

GEBZE TECHNICAL UNIVERSITY

GRADUATE SCHOOL OF NATURAL AND APPLIED SCIENCES

REACTIVE SINTERING OF TiC-BASED CERMETS BY USING IRON, TITANIUM AND CARBON POWDERS

MAMMADHUSEYN MAMMADZADA

A THESIS SUBMITTED FOR THE DEGREE OF MASTER OF SCIENCE

DEPARTMENT OF MATERIALS SCIENCE AND ENGINEERING

THESIS SUPERVISOR

PROF. DR. MEHMET TARAKÇI

GEBZE

2021

T.C.
GEBZE TEKNİK ÜNİVERSİTESİ
FEN BİLİMLERİ ENSTİTÜSÜ

DEMİR, TİTANYUM VE KARBON TOZLARI KULLANILARAK TiC BAZLI SERMETLERİN REAKTİF SİNTERLENMESİ

MAMMADHUSEYN MAMMADZADA
YÜKSEK LİSANS TEZİ
MALZEME BİLİMİ VE MÜHENDİSLİĞİ
ANABİLİM DALI

DANIŞMANI
PROF. DR. MEHMET TARAKÇI

GEBZE
2021

GEBZE TEKNİK ÜNİVERSİTESİ	YÜKSEK LİSANS JÜRİ ONAY FORMU

GTÜ Fen Bilimleri Enstitüsü Yönetim Kurulu'nun 05/02/2021 tarih ve 2021/06 sayılı kararıyla oluşturulan jüri tarafından 01/03/2021 tarihinde tez savunma sınavı yapılan Mammadhuseyn MAMMADZADA 'ın tez çalışması Malzeme Bilimi ve Mühendisliği Anabilim Dalında YÜKSEK LİSANS tezi olarak kabul edilmiştir.

JÜRİ

ÜYE
(TEZ DANIŞMANI) : Prof. Dr. Mehmet RATAKÇI

ÜYE : Prof. Dr. Yücel GENÇER

ÜYE : Doç. Dr. Mediha İPEK

ONAY

Gebze Teknik Üniversitesi Fen Bilimleri Enstitüsü Yönetim Kurulu'nun
…..…/…..…/..…..… tarih ve ……/…….. sayılı kararı.

İMZA/MÜHÜR

SUMMARY

It has been carried out to investigate the production parameters of TiC-reinforced iron-based cermets through the reactive sintering technique in the present MSc thesis. Based on the analysis of reactive sintering parameters, it was tried to improve the physical property such as density and mechanical property such as hardness according to the results obtained. The cermet which was produced with optimum parameters as a result of the study is planned to be a ready-to-use.

The reaction between Ti and C occurring on sintering is highly exothermic and the energy which was released in the reaction was considered as an extra driving force for sintering. In this respect, it was aimed to observe an enhancement on the final physical and mechanical properties as a result of reactions taking place during sintering processes.

In experiments, titanium, graphite, and iron were used as raw materials. Mixing operations were applied as uniaxial mixing in a dry medium to homogenize raw materials. Various ratios of raw materials were used to obtain different TiC percentages in final products. Powder mixtures were pressed in a uniaxial press under constant pressure to obtain green pellets. Interactions between reactant powders were investigated by developing thermochemical models at high temperatures. In the next step, the reactive sintering processes were realized for the same duration at various synthesis-sintering temperatures. Reactive sintering experiments were conducted in a vacuum sintering furnace allowing carrying out experiments under an inert gas atmosphere. Depending on these experimental parameters, density and hardness measurements were conducted in sintered pellets. To take micrographs from sintered pellets, the SEM-EDS technique and optical microscopy were used. XRD method was also be utilized to characterize final phase properties. The results were compared to the literature for benchmarking. In this thesis, together with obtaining high mechanical properties, it is economical and bulk producibility is aimed.

Key Words: Metal Matrix Composite, SHS, Reactive Sintering, TiC Based Cermet, TiC-Fe Composite

ÖZET

Bu yüksek lisans tezinde reaktif sinterleme tekniği ile TiC takviyeli demir esaslı sermetlerin üretim parametrelerinin incelenmesi gerçekleştirilmiştir. Reaktif sinterleme parametrelerinin analizine dayanılarak elde edilen sonuçlara göre yoğunluk gibi fiziksel özellikler ve sertlik gibi mekanik özellikler iyileştirilmeye çalışılmıştır. Çalışma sonucunda optimum parametrelerle üretilen sermetin kullanıma hazır olması planlanmıştır.

Sinterlemede meydana gelen Ti ve C arasındaki reaksiyon oldukça ekzotermiktir ve reaksiyonda açığa çıkan enerji sinterleme için ekstra bir itici güç olarak kabul edilmiştir. Bu bağlamda, sinterleme işlemleri sırasında meydana gelen reaksiyonlar sonucunda nihai fiziksel ve mekanik özelliklerde bir artış gözlemlenmesi amaçlanmıştır.

Deneylerde ham madde olarak titanyum, grafit ve demir kullanıldı. Karıştırma işlemleri, hammaddelerin homojenize edilmesi için kuru bir ortamda tek eksenli karıştırma şeklinde uygulanmıştır. Nihai ürünlerde farklı TiC yüzdeleri elde etmek için çeşitli hammadde oranları kullanılmıştır. Toz karışımları, yeşil topaklar elde etmek için sabit basınç altında tek eksenli bir preste preslendi. Reaktif tozlar arasındaki etkileşimler, yüksek sıcaklıklarda termokimyasal modeller geliştirilerek incelenmiştir. Bir sonraki aşamada, çeşitli sentez-sinterleme sıcaklıklarında aynı süre boyunca reaktif sinterleme işlemleri gerçekleştirilmiştir. Reaktif sinterleme deneyleri, inert bir gaz atmosferi altında deneylerin yapılmasına izin veren bir vakumlu sinterleme fırınında gerçekleştirildi. Bu deneysel parametrelere bağlı olarak sinterlenmiş peletlerde yoğunluk ve sertlik ölçümleri yapılmıştır. Sinterlenmiş peletlerden mikrograflar almak için SEM-EDS tekniği ve optik mikroskopi kullanıldı. Nihai faz özelliklerini karakterize etmek için XRD yöntemi de kullanıldı. Sonuçlar, kıyaslama için literatürle karşılaştırıldı. Bu tezde yüksek mekanik özellikler elde etmekle birlikte ekonomik ve toplu üretilebilirlik hedeflenmektedir.

Anahtar Kelimeler: Metal Matris Kompozit, KYYSS, Reaktif Sinterleme, TiC Bazlı Sermet, TiC-Fe Kompozit

ACKNOWLEDGEMENTS

First of all, I would like to endless thanks my family for their moral support throughout my education. I am grateful to my supervisor - Prof. Mehmet TARAKÇI for guiding me to be successful. I would also like to thank Prof. Yücel GENÇER and Asst. Prof. Ahmet TURAN for his special interest throughout my thesis. I really appreciate to Mr. Yusuf ALAN from KÖRFEZ DÖKÜM A.Ş. and Dr. Uğur DEMİRLER from KÖRFEZ SANTRİFUJ BORU DÖKÜM LTD. ŞTI. to provide me with various opportunities and assistance during my graduate studies.

TABLE of CONTENTS

	Page
SUMMARY	v
ÖZET	vi
ACKNOWLEDMENTS	vii
TABLE of CONTENTS	viii
LIST of ABBREVIATIONS and ACRONYMS	x
LIST of FIGURES	xi
LIST of TABLES	xiv
1. INTRODUCTION	1
1.1. Definition of Metal Matrix Composites	1
1.1.1. Reinforcement Phase of Cermet Structure	2
1.1.2. Binder Phase of Cermet Structure	5
1.1.3. Fabrication Techniques of MMCs	6
1.2. TiC-Based Cermet	9
1.2.1. Self-Propagating High Temperature Synthesis of TiC (SHS)	9
1.2.2. Fabrication of TiC-Based Cermet	10
1.2.3. Reactive Sintering Tic-Based Cermet Structure	11
2. MATERIALS AND METHODS	21
2.1. Properties of Reactant Powders	21
2.2. Production Process of Cermets	22
2.3. Characterization Methods of Cermets	28
3. RESULTS AND DISCUSSIONS	31
3.1. Characterization of Reactant Powders	31
3.2. Thermochemical Modelling of Cermets	38
3.3. Hardness of Cermets	40
3.4. Density of Cermets	42
3.5. XRD Analysis of Cermets	44
3.6. OM and SEM Analysis of Cermets	48
5. CONCLUSION	107

REFERENCES 110
BIOGRAPHY 114
APPENDICES 115

LIST of ABBREVIATIONS and ACRONYMS

Abbreviations and Acronyms		**Explanations**
Ø		Diameter
Δ G˚	:	Gibbs Free Energy
g	:	Gram
h, min , s	:	Hour, Minute, Second
J, kJ	:	Joule, Kilojoule
K,˚C	:	Kelvin, Degree Celsius
mol	:	Mole
nm, μm, mm, cm, dm, m	:	Nanometer, Micrometer, Millimeter, Centimeter, Decimeter, Meter
Pa, MPa	:	Pascal, Megapascal
A.P.S	:	Average Particle Size
DTA	:	Differential Thermal Analysis
HIP	:	Hot Isostatic Pressure
HRC	:	Hardness Rocwell C
HV	:	Hardness Vickers
MMC	:	Metal Matrix Composite
S.D.	:	Standard Deviation
SEM-EDS	:	Scanning Electron Microscopy with Energy Dispersive Spectroscopy
SHS	:	Self-Propagating High-Temperature Synthesis
SPS	:	Spark Plasma Sintering
TiC	:	Titanium Carbide
XD	:	Exothermic Dispersion
XRD	:	X-Ray Diffraction
XRF	:	X-Ray Fluorescence

LIST of FIGURES

Figure No:		Page
1.1:	Manufacturing methods of in-situ MMCs.	8
1.2:	Theoretical thermocalculated phase diagram for TiC/TiCN-based cermets with steel binder.	11
1.3:	Curves of the standard forming Gibbs free energy of the possible products in Fe-Ti-C system as a function of temperature.	16
1.4:	Effects of temperature on the relative densities and hardness of the specimens.	17
1.5:	The temperature–time profiles of 20 wt.% Ni–Ti–C systems with different C particle sizes (∼1 μm, ∼38 μm and ∼150 μm) during SHS process.	18
2.1:	Production scheme of the reactive sintering of the TiC-based cermets	23
2.2:	Uniaxial mixing for preparation of powder mix.	24
2.3:	Powder forming equipment, a) Compression mold, b) Hydraulic press.	25
2.4:	Examples for shaped green cermets, a) KB 1200-3 b) KB 1200-5 c) KB 1200-7	25
2.5:	Cermet samples after sintering.	27
3.1:	The average particle size distribution of metallic powders, a) Fe and b) Ti.	31
3.2:	SEM micrographs of Fe powder, a) 1000X, b) 2000X.	33
3.3:	SEM-EDS results of Fe powder	34
3.4:	SEM micrographs of Ti powder; (a) 1000X, (b) 2000X.	35
3.5:	SEM-EDS results of Ti powder.	36
3.6:	SEM micrographs of graphite powder; (a) 1000X, (b) 2000X	37
3.7:	XRD patterns of reactant powders.	38
3.8:	Results of thermochemical modeling for the different variations of TiC in the iron matrix, a) 30%, b) 50% and c) 70% TiC.	39-40
3.9:	Examples for hardness indents, a) KB 1200-3, b) KB 1350-5, c) KB 1500-7.	41

3.10:	Hardness change of the cermets depending on sintering temperature.	42
3.11:	Density change of the cermets depending on sintering temperature.	43
3.12:	XRD patterns of the cermets containing 30 wt.% TiC.	44
3.13:	XRD patterns of the cermets containing 50 wt.% TiC.	45
3.14:	XRD patterns of the cermets containing 70 wt.% TiC.	45
3.15:	XRD patterns of cermets sintered at 1200 ^{o}C.	46
3.16:	XRD patterns of cermets sintered at 1275 ^{o}C.	46
3.17:	XRD patterns of cermets sintered at 1350 ^{o}C.	47
3.18:	XRD patterns of cermets sintered at 1425^{o}C.	47
3.19:	XRD patterns of cermets sintered at 1500 ^{o}C.	48
3.20:	Micrographs of KB 1200-3 at a) 50X b) 500X c) 1000X d) 2000X e) 5000X and f) tipical particle sizes of TiCs at 5000X.	52-54
3.21:	Micrographs of KB 1200-5 at a) 50X b) 500X c) 1000X d) 2000X e) 5000X and f) tipical particle sizes of TiCs at 5000X.	55-57
3.22:	Micrographs of KB 1200-7 at a) 50X b) 500X c) 1000X d) 2000X e) 5000X and f) tipical particle sizes of TiCs at 5000X.	58-60
3.23:	Micrographs of KB 1275-3 at a) 50X b) 500X c) 1000X d) 2000X e) 5000X and f) tipical particle sizes of TiCs at 5000X.	61-63
3.24:	Micrographs of KB 1275-5 at a) 50X b) 500X c) 1000X d) 2000X e) 5000X and f) tipical particle sizes of TiCs at 5000X.	64-66
3.25:	Micrographs of KB 1275-7 at a) 50X b)500X c) 1000X d) 2000X e) 5000X and f) tipical particle sizes of TiCs at 5000X.	67-69
3.26:	Micrographs of KB 1350-3 at a) 50X b) 500X c) 1000X d) 2000X e) 5000X and f) tipical particle sizes of TiCs at 5000X.	70-72
3.27:	Micrographs of KB 1350-5 at a) 50X b) 500X c) 1000X d) 2000X e) 5000X and f) tipical particle sizes of TiCs at 5000X.	73-75
3.28:	Micrographs of KB 1350-7 at a) 50X b) 500X c) 1000X d) 2000X e) 5000X and f) tipical particle sizes of TiCs at 5000X..	76-78
3.29:	Micrographs of KB 1425-3 at a) 50X b) 500X c) 1000X d) 2000X e) 5000X and f) tipical particle sizes of TiCs at 5000	79-81
3.30:	Micrographs of KB 1425-5 at a) 50X b) 500X c) 1000X d) 2000X e) 5000X and f) tipical particle sizes of TiCs at 5000X.	82-84

3.31:	Micrographs of KB 1425-7 at a) 50X b) 500X c) 1000X d) 2000X e) 5000X and f) tipical particle sizes of TiCs at 5000X.	85-87
3.32:	Micrographs of KB 1500-3 at a) 50X b) 500X c) 1000X d) 2000X e) 5000X and f) tipical particle sizes of TiCs at 5000X.	88-90
3.33:	Micrographs of KB 1500-5 at a) 50X b) 500X c) 1000X d) 2000X e) 5000X and f) tipical particle sizes of TiCs at 5000X.	91-93
3.34:	Micrographs of KB 1500-7 at a) 50X b) 500X c) 1000X d) 2000X e) 5000X and f) tipical particle sizes of TiCs at 5000X.	94-96
3.35:	SEM micrographs from the outer surface of the KB 1350-3 at a) 125X b) 500X.	98
3.36:	SEM micrographs from the outer surface of the KB 1425-3 at a) 125X b) 500X.	99
3.37:	SEM micrographs from the outer surface of the KB 1425-5 at a) 125X b) 500X.	100
3.38:	SEM micrographs from the outer surface of the KB 1500-3 at a) 125X b) 500X.	101
3.39:	SEM micrographs from the outer surface of the KB 1500-5 at a) 125X b) 500X.	102
3.40:	SEM-EDS results of KB 1500-5 sample in mapping mode	106

LIST of TABLES

Table No:		Page
1.1:	Properties of important wear-resistant hard materials.	3
1.2:	Contact angles of matrix metal on TiC-Metal systems depending on sintering atmosphere.	5
1.3:	Physical properties of TiC .	10
1.4:	Chemical compositions of reactants used by Raghunath's study.	12
1.5:	The starting powders of 75(Ti+17C) – 25NiMo (2:1) cermet in the study of Joeleht.	13
1.6:	Effects of used C /Ti ratio of in-situ TiC/Fe alloy composites on mechanical properties.	19
2.1:	Chemical composition of raw powder materials, a) Fe, b) Ti, c) Graphite.	21
2.2:	The average particle size of raw materials.	22
2.3:	Chemical compositions of reactive sintering of TiC-based cermet	23
2.4:	Grinding parameters applied in surface preparation.	29
3.1:	The average measured hardness and standard deviation values of the samples.	41
3.2:	The average measured bulk and relative density values of the samples.	43
3.3:	Average particle sizes of TiC particles.	103
3.4:	Average of C/Ti ratio at EDS points of TiC.	105

1. INTRODUCTION

1.1. Definition of Metal Matrix Composites

In today's conditions, it is expected that the life and performance values of the materials will be maximized. Due to reduced resources, materials must provide superior performance under service conditions as well as rapid and easy production with low costs. Multiple features are tried to be obtained in materials developed for many engineering applications. It has been proven that mechanical properties such as high hardness, strength, toughness, wear resistance, as well as chemical properties such as chemical stability, cannot be achieved with only conventional material types (metals, ceramics, and polymers). Cermet materials developed to provide these properties are a type of metal matrix composite consisting of ceramic phases and metal phases [1-2].

If we consider cermet structure under a more specific subgroup, it is seen that metal matrix composites are widely used in many engineering fields today. Metal matrix composites (MMCs) are reinforced with ceramic materials, especially in applications where there is exposure to mechanical forces [2][3]. Just to define it in more detail, metal matrix composite materials are a large group of materials formed from the combination of many different systems, scales, and microstructures. The only common point of the members of this group of materials is that there is a metallic phase that connects the structure. Ceramic materials can be used generally as reinforcing constituents, however, in exceptional cases, refractory metals, intermetallic, and semiconductors are also used instead of ceramics to meet different properties by the composite material. Metal matrix composites are defined according to structural features under three different subtitles based on reinforcement variety;

- Particles, distributed homogeneous or nonhomogeneous,
- Short fibers, with or without a degree of alignment,
- Long aligned fibers [4].

Particulate reinforced metal matrix composites are also defined as cermets and, they are used in many different industries. The structure of cermets, a special type of MMC, was obtained by attaching the ceramic in the particle form with a metallic phase together. Also known as ‘’Hardmetals’’, cermet materials combine the most favorable

characteristics of ceramics and metals, high hardness and elastic moduli of ceramics, the ductility and toughness of metals. Studies on cermet materials started at the beginning of the 20th century and were patented for the first time in 1923 by the German company "Osram Studiengesellschaft". The first commercial product intended for use in metal cutting applications was released to the market by F. Krupp in 1927 under the name "Widia (from" wie Diamant "- like a diamond). The evolution of cermets is continuing thanks to different research and development, and today, it is allowed to be used in a broad range of demanding wear and/or corrosion applications, as both bulk materials and coatings. Cermet uses include tools for grinding, cutting, and machining; mechanical seals; friction surfaces; aviation coatings; are the largest and also specific parts such as ball-point pens, punches, dies, nozzles, or valves for the oil-gases industry. More than 80 percent of the cermets produced today are used especially for metal cutting and processing purposes [5–7,4,8]. Recently, discontinuous MMCs reinforced with particles are more preferred and developed thanks to the advantages below.

- Availability of various types of reinforcement at competitive costs,
- Successful development of manufacturing processes to produce MMCs with reproducible structure and properties,
- Availability of standard or near-standard metalworking methods which can be utilized to fabricate these MMCs.

Especially, ceramic particle reinforced MMCs have the most common usage due to their ease of manufacture, lower costs, and isotropic properties [2].

1.1.1. Reinforcement Phase of Cermet Structure

In the first cermet production in history, WC was used as a strengthening reinforcing phase. TiC reinforced cermets were used for higher hardness property as a result of developments to meet different requirements. Nowadays, complex ceramic forms formed by chromium, titanium, tungsten, vanadium, molybdenum, aluminum, and similar metals with carbon, nitrogen, oxygen, boron are used as reinforcement phases in cermet production in line with industry needs. In Table 1.1., the properties of the materials found as reinforcing phase in the most common cermet structures used in the cutting and metalworking fields are shown [5,1,4,6–8,10–14,9,15,16].

Table 1.1. Properties of important wear-resistant hard materials.

Property	High-speed steel	WC–Co cemen-ted carbides	TiC-based carbides	Ceramics (oxides, nitrides)	Poly-crystal-line cubic BN	Poly-crystal-line diamond
Density (g/cm^3)	8.0-9.0	9.0-15.0	5.0-9.0	3.2-5.0	3.45	3.5
Vickers hardness (HV)	750-800	800-1900	1500-2200	1500-2500	4000	8000
Transverse rupture strength (N/mm^2)	3000-4000	1000-3000	900-1800	400-600	500-800	600-1100
Hot transverse rupture strength (at 1000 °C, N/mm^2)	500	900-1500	600-1500	400-600	500-700	600-1000
Compressive strength (N/mm^2)	3500-4000	4000-7000	3000-5000	3000-4000	6000	7600
Modulus of elasticity (kN/mm^2)	210	400-680	300-450	300-400	680	850
Thermal expansion coefficient ($10^{-6}/K^{-1}$)	12	5.0-7.0	6.0-8.0	2.5-7.5	3.5	1.2

Carbide-based reinforcing phases are chemically stable and their dissolution in binder metal phases is very low, especially at high temperatures. Carbide and cemented carbide materials have sufficient fracture toughness together with the high hardness they exhibit. Their thermal and electrical conductivity and thermal expansion coefficient values are closer to metal materials, causing them to be preferred more in cermet materials. Besides, especially carbides are better heated by the metal phases, so the efficiency of the liquid phase sintering process is higher. WC-Co, TiC-Fe, TaC-Co, Mo_2C-NiMo, TiN-Ti(CN)-Co, Cr_2C_3-Ni, (Ti,Mo)C-Ni, (W,Ti)C-Ni, WC-TiC-Co,

TiC-TiCN-Ti which are widely used in the industry, is the most familiar example of carbide cermet structures [5–7,17,4,8].

Oxide materials could be insufficiently wetted by metals which situation is explained by weak bonding at metal-oxide interfaces and, they also tend to react to form complex oxides at high temperatures. Therefore, the percentage of use in cermet production is low and very difficult. Due to the low thermal shock and fracture toughness, was usually predicted the use of hard binder metals with oxide-based reinforcements, but this situation has disadvantages for hardening the metal with different processes. However, oxide cermets show some clear advantages in terms of their use in applications which at resistance to oxidation or chemicals and high temperature must be ensured. Thanks to these properties, oxide based cermets have specific usage areas in the industry, Al_2O_3-Ni_3Al, Al_2O_3-Cr, Al_2O_3-TiC-Ni are used as wear parts at high temperature, Zr_2O-Ti, ZrO_2-Mo are used in wear and chemical applications, ZrO_2-Mo are also used in thermocouple sheaths and extrusion dies, Yttria-stabilized zirconia (YSZ)-Ni cermet are used as anodes in solid oxide fuel cells [6–8].

The chemical stability of borides is almost more than carbides, so this feature creates an opportunity for use in applications requiring extreme heat and corrosion resistance. Thanks to their strength of over 200 MPa, borides have competitive use in the production of cermets by increasing the toughness by using metallic binders. Molds or crucibles used for reactive metals such as copper, bronze, lead, and zinc are made of cermets consisting of reinforcement such as TiB_2, ZrB_2, CrB_2, MoB_2, and binders such as iron, nickel, chromium, or molybdenum [7,8,18,19].

The hardest ceramics are also found among nitride compounds of metalloid elements. Silicon nitride (Si_3N_4) and cubic boron nitride (cBN) are the most important among these. The use of nitride-based cermets is often limited to abrasive and cutting applications. Practically, one of the reasons why such reinforced cermets are of less interest is the extreme difference in elastic modulus and thermal expansion values between matrix and reinforcement. AlN is also a different important nitride but it has wide usage, unlike others, especially in integrated circuits. AlN, which is a very good electrical insulator, is also a good thermal conductor. Liquid phase sintering is widely preferred in the production of AlN-based cermets, this is achieved by the easy wetting of AlN ceramics of molten metals such as Al and Ni [7].

1.1.2. Binder Phase of Cermet Structure

Metals such as nickel, titanium, cobalt, aluminum, copper, chromium, iron, and also steel are widely used in cermet structures as matrix components. The key parameter to choose metal as a binder is the low surface energy difference between metal and ceramic particles for a continuous network structure. This network structure depends on the chemical properties, amount, and dihedral angle of the binder used. As shown in Table 1.2., the wettability angle of binder metals varies according to different sintering atmosphere conditions. The mechanical properties of the metal binder are also affected by solute impurities or precipitates deriving from the elements contained in the original ceramic powders [7,1,9–14].

Table 1.2. Contact angles of matrix metal on TiC-Metal systems depending on sintering atmosphere.

Metal	Hydrogen	Helium	Vacuum
Fe	49	36	41
Co	36	39	5
Ni	17	32	30

Cobalt is the most commonly used and preferred binder in WC-based cermets as it wets the WC easily, exhibits a temperature-dependent solubility that aids in sintering and leading to products with superior strength and ductility. Cobalt as a ferromagnetic binder also facilitates the magnetic nondestructive evaluation of the metallurgical alloy composition by the measurement of coercitivity and magnetic saturation [6].

Iron-based binders have been intensively researched and developed for more than 50 years, but they have been used in specific applications. The amount of carbon contained in the structure of iron-based binders can be effective on important properties, nevertheless, essential information about the raw materials, phase diagrams, manufacturing stages, material properties, and application conditions of these types of cermets have been obtained. Iron-based binders have a large application area in metal-rich-TiC based cermets. It is also known that iron matrices are perfectly compatible with TiB2 reinforcement ceramics. Fe-based metal matrices alloyed with

metals such as Mn, Cr, Al are also suitable for WC ceramic phases. Fe-based binder cermets exhibit superior features compared to their competitors in applications where abrasion resistance is important. Iron-based binders have also a wide application area in thermal spray coatings together with the production of bulk cermet thanks to their properties. Cermets with Fe-based binder are gaining superiority in application use in metal cutting, non-ferrous and woodworking, stone processing, road planing, mining, chipless forming, and wearing parts. The fact that iron-based binder phases have more environmentally and at the same time relatively inexpensive production methods is another driving force for the widespread acceptance of this class of materials shortly [6].

Nickel-based binder phases are generally used to create resistance against acidic corrosion. This type of binder exhibits nonmagnetic properties and can only be examined metallographically. It is known that the strength of the binder phase can be increased by metallurgical alloying methods such as solid solution strengthening and dispersion hardening applied to nickel.[6]

1.1.3. Fabrication Techniques of MMCs

Powder metallurgy, spray deposition, mechanical alloying (MA) and various casting techniques (squeeze casting, rheocasting and compocasting) are well-known standard production technics of discontinuously reinforced MMCs. In all of these conventional techniques, the matrix phases consist of molten or powder form and the added ceramic reinforcement phases are prepared separately, regardless of the structure. In conventional MMCs called ex situ, the dimensions of the reinforcement phase are determined by the size of the starting powders and these sizes are usually micron to tens of microns and rarely less than 1 mm. Poor wettability between reinforcements and matrix due to interfacial reactions between reinforcements and matrix and surface contamination of reinforcements are other main disadvantages that must be overcome. Particle size and their volumetric ratio to the matrix are the main variables that determine the mechanical properties of MMCs, however these changes also balance the reinforcement-matrix interface quality. An optimum set of mechanical properties can be achieved when fine and thermally stable ceramic particulates are dispersed uniformly in the metal matrix.

Obtained in the synthesis of the reinforcement phase inside a metallic matrix by chemical reactions between elements or between elements and compounds during composite fabrication are known as in-situ MMCs. In-situ MMCs provide advantages given below as a list in comparison with those produced by conventional ex-situ MMCs.

- the in-situ formed reinforcements are thermodynamically stable at the matrix, leading to less degradation in elevated-temperature services,
- the reinforcement-matrix interfaces are clean, resulting in a strong interfacial bonding,
- the in-situ formed reinforcing particles are finer in size and their distribution in the matrix is more uniform, yielding better mechanical properties.

Therefore, many production techniques for in-situ MMCs are being developed, as they have a wide range of uses and promise great potential [2,20–25,3,26].

Koczak and Premkumar's suggestion consisted of the classification of in-situ reactions in terms of starting phases, such as gas-liquid, liquid-solid, liquid-liquid, etc. [27].

Categorized by Tjong and Ma the fabrication methods of MMCs were based on temperatures of metallic matrix and reactants during the process. Classified under four process groups (solid-liquid reaction, vapor-liquid-solid reaction, solid solid reaction, and liquid-liquid reaction) are detailed in Fig. 1.1 [2].

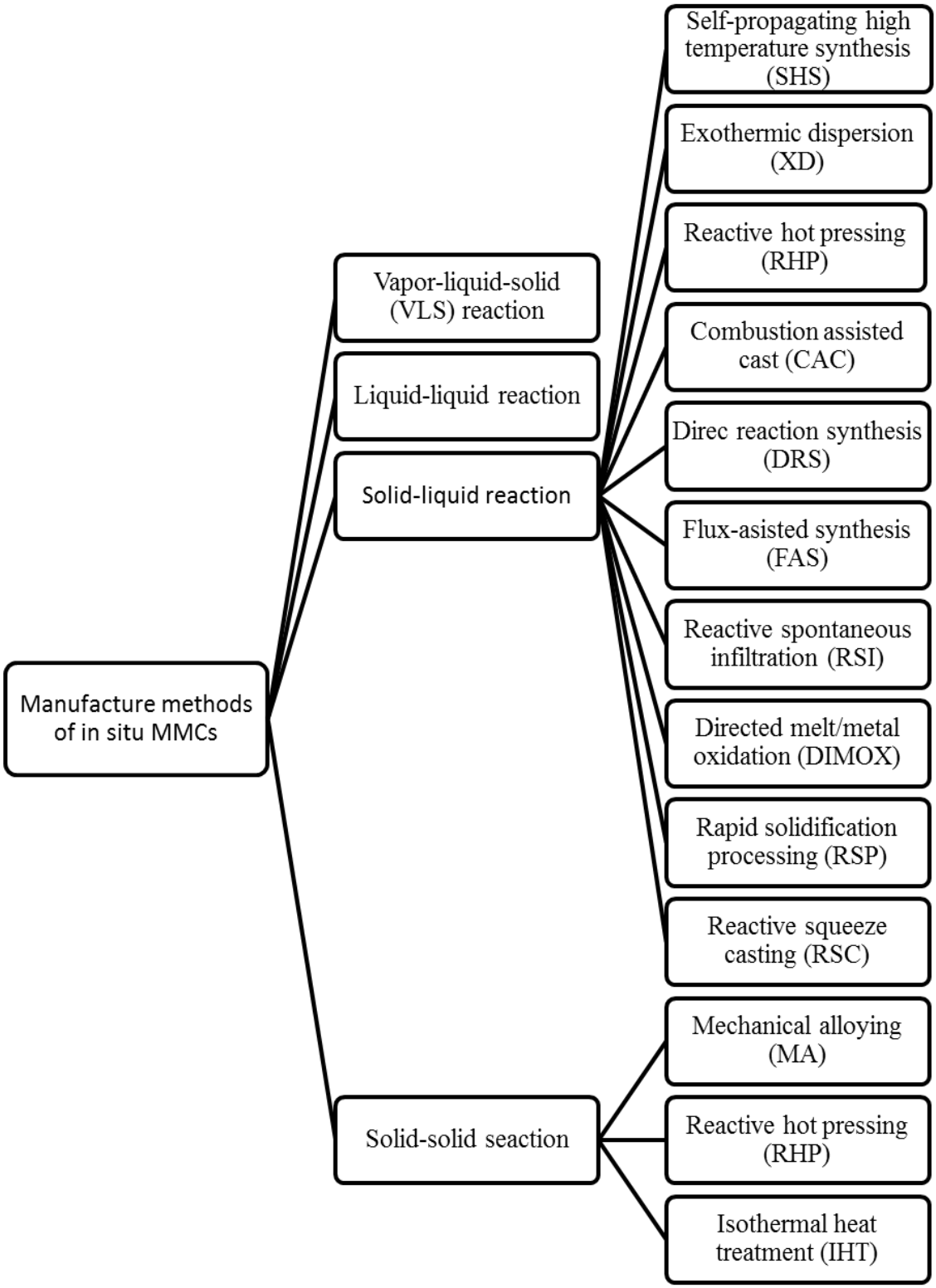


Figure 1.1. Manufacturing methods of in-situ MMCs.

1.2. TiC-Based Cermet

1.2.1. Self-Propagating High Temperature Synthesis of TiC

At the end of the 1960s, Merzhanov's team developed self-propagating high-temperature synthesis (SHS), synthesis can be explained as reactants that have sufficiently high heat of formation are synthesizing with help of ignition energy, and the reactants are converting to the products during spontaneously propagates throughout the reaction. The most important advantage of SHS reactions is that they are self-sustaining reactions and three essential requirements must be met for the continuity of the reaction. The first requirement is about the exothermic properties of the reaction have to be high. The heat released during the reaction must be enough help to protect the extension front by heating the unreacted part of the sample to its ignition temperature. The heat of reaction of the order of -167 kJ/g mol is sufficient to maintain a propagating front. One of the reactants is passing to the liquid or vapor phase to be helpful of diffusion of fluid phase reactant to the front of reaction are the main second requirement of SHS reaction. The third requirement is about the rate of heat loss via conduction and radiation, so must be less than generated ones. It has an importance on the reaction will not be extinguished due to extreme heat losses to the surroundings. The self-generation of energy required for the process, the high-purity products due to volatilization of low boiling point impurity at elevated temperature, and high productivity due to very high reaction rates are the most attractive sides of the SHS fabrication technique [28–30,18,19].

The SHS reaction between Ti and C is one of the most widely studied. Detailed researches can be found on the structural, physical, and thermodynamic properties of the reaction and its product. A homogeneous phase is displayed when the carbon content is between 0.47-1% in the TiC composition. The lattice structure of TiC is similar to NaCl type as known as face-centered cubic, and the value of lattice parameter (a_0) decreasing with decreasing carbon content equals 0.4329. TiC looks black and has main physical properties as given in Table 1.3. [31–33].

Table 1.3. Physical properties of TiC.

Density (g/cc)	Melting point (°C)	Modulus of eslasticity (GPa)	Coefficient of thermal expansion
4.93	3067	439	$8.15\text{-}9.45 \times 10^{-6}$ (25-1500 °C)

This type of reaction method is also used to obtain reinforcement phases of reactive sintering TiC-based cermet in this thesis**.**

1.2.2. Fabrication of TiC-Based Cermet

Superior corrosion and high temperature wear resistance are important advantageous features of TiC based cermets. In general, besides its use in metal cutting tools, TiC-based cermets attract the attention of material design engineers thanks to their superior properties. Compared with other cemented carbides, TiC-based cermets have low toughness and bending stress. TiC-based cermets in erosion and wear resistance properties lag behind common ones such as WC-Co [16,34].

Nevertheless, TiC has very commercial interests with the help of properties of ultra-hardness (known hardest metal carbide, under 1N, TiC–3200 HV, WC-2200), excellent thermal stability, very high melting temperature (TiC- 3080 °C, WC-2850 °C), and good wettability. So it is shown as suitable for Fe, Ni, Ti, TiNi, and Al matrixes as a reinforcer. Most commonly, TiC/TiCN ceramic particles are held together by steel-based binders, the phase balance diagram between steel and TiC/TiCN prepared by Alvaredo et al. in Fig 1.2. is one of the most comprehensive ones prepared on this subject [35].

At the same time, the difficulty of production of TiC makes it difficult to use it more widely in commercial applications. Industrial powder production of TiC is obtained from TiO_2, which is reduced with carbon at temperatures of 1900-2100 °C. There are also disadvantages of this method, such as high power consumption due to high synthesis temperature and high equipment [36].

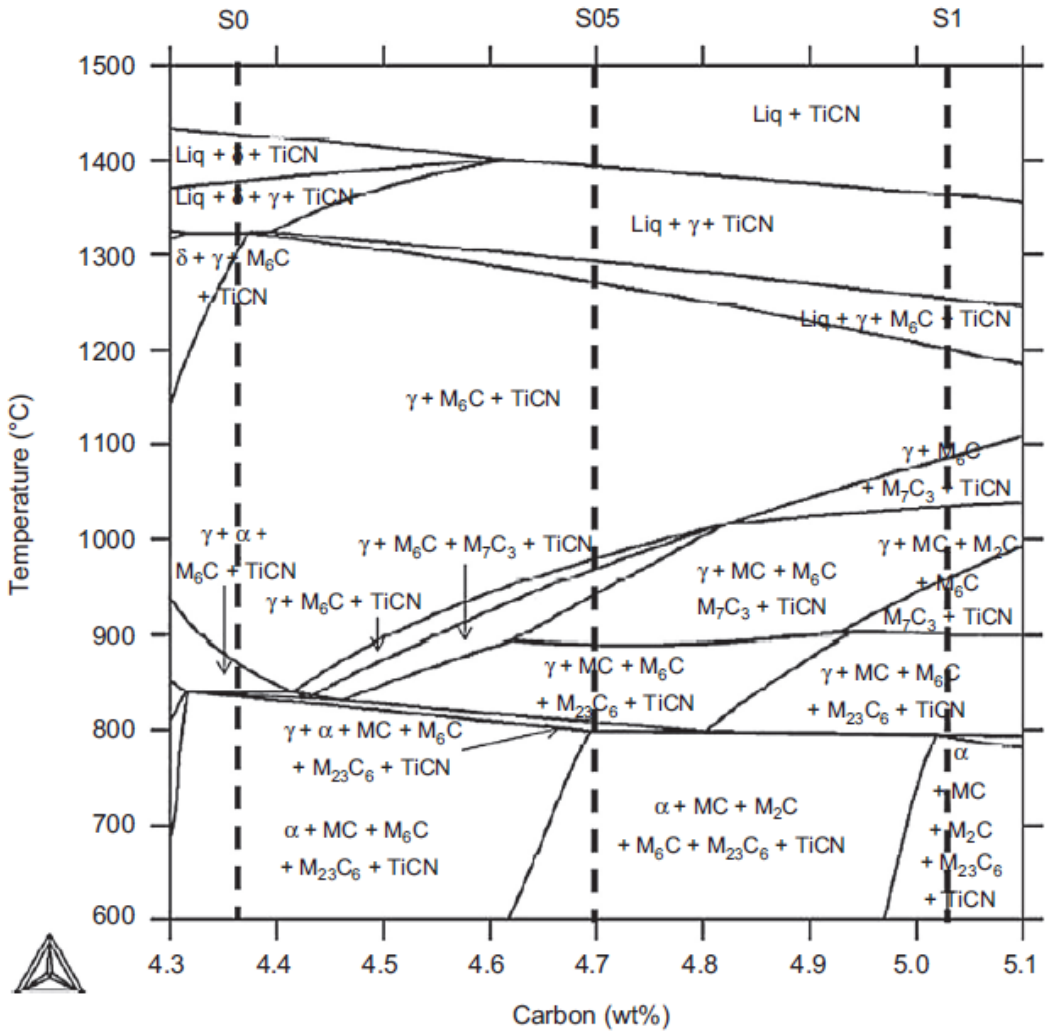


Figure 1.2. Theoretical thermocalculated phase diagram for TiC/TiCN-based cermets with steel binder.

1.2.3. Reactive Sintering TiC-Based Cermet Structure

When the studies conducted are examined, it is determined that TiC has many advantages and disadvantages. However, TiC cermets have been the subject of many academic studies and industrial applications. Especially, the number of studies and applications related to TiC cermet products produced with SHS is increasing day by day.

Studies about TiC based MMCs fabricated with the help of the SHS method can be examined in different directions such as reactant material, synthesis techniques, pre-activation processes, etc. With the reactive sintering process, Fe, Ti, FeTi, TiH2, graphite, carbon black, cast iron, and steel powders are generally used as reactants in iron matrix TiC-based cermet manufacturing. Mechanical alloying, pressing, plastic

forming, preheating, igniting, and similar processes applied as pretreatment are utilized to improve the overall product quality and also sometimes to obtain specific features. TiC-based cermets with iron alloy matrix are produced by using the energy of the liquid metal during casting, sintering in an atmosphere-controlled furnace, synthesizing with SPS, HIP methods, SHS combustion systems.

In the study of Raghunath et al., Fe-TiC composites synthesized with in-situ technique have been researched adding ferrotitanium (average size >60 μm) to melted ductile iron inside induction furnace under shielding nitrogen gas, chemical compositions are given below in Table 1.4.

Table 1.4. Chemical compositions of reactants used by Raghunath's study.

Material	C %	Ti %	S %	P %	Si %	Al %	V %	Mn %	Fe %
Ductile iron	3.7	-	2.5	0.21	-	-	-	0.38	Bal.
Ferro-Titanium	0.09	70.65	0.013	0.012	0.112	0.014	0.88	-	Bal.

To solidify composite under 1000 psi was treated again by remelting and solidification under vacuum (10^{-6} torr). The outputs obtained in this study are as follows,

- Synthesized composite up to 30 vol % of TiC in the ferrous based matrix with the aforementioned method was succeeded with the help of identify in-situ forms of TiC,
- Only TiC-based composites up to 10% by volume can be cast statically, for more, gas pressure must be applied during solidification,
- Vacuum synthesis of composites many acts as helpful to eliminate the foaming problems.
- It was observed distributed uniformly spherulitic carbides in the metal matrix of composite microstructures.
- When there is more than 0.45% TiC in the melt, the viscosity of the phase mixture increases and it becomes difficult to control the temperature of the melt [37].

In the study of Joeleht et al., different milling times (4, 6, 8 and 10 hours, 540 RPM, 10:1, Ø 6 WC-Co balls) were applied to the reactants with the constant composition (Ti, C black, Ni, and Mo) and details were given Table 1.5.

Table 1.5. The starting powders of 75(Ti+17C) – 25NiMo (2:1) cermet in the study of Joeleht.

	Titanium	Carbon	Nickel	Molybdenum
Composition of powder mixture (wt.%)	62.2	12.8	16.7	8.3
Content of main element (wt.%)	99.7	99.8	99.8	99.8
Avarage particle size (μm)	20	6.5	6.0	2.5

After milling powder was subjected to a two-stage sintering process (0-1270 ^{o}C, 4 ^{o}C/min, 1 h, and 1270-1500 ^{o}C, 10 ^{o}C/min, 1 h). After the transformation of the nickel from solid to liquid phase, sintering continued under isostatic pressure (15 MPa) of argon gas for 30 minutes. Explained as conclusions of the study, it was shown shorter milling (4 h) causes to occur a three-phased system where TiC is in the core and surrounded by the double carbide form as (Ti,Mo)C and nickel binder respectively. On the other hand, increased milling durations (8 and 10 h) are affective on the composion of two phases, dual-carbide grains of (Ti,Mo)C and nickel matrix. Despite applied the 15 MPa of isostatic argon gas pressure along period of the liquid phase sintering, long milling time increases the pore formation, so this issue can be explained as oxygen contamination occurring at milling. The optimal milling duration based on this research and attrition mill was found to be 6 h [38].

In the article published by Ding et al., selected Ti, C and Ni powders (>99.5 wt.%, Ti-3 μm, C-2.8 μm, Ni-1 μm) were mixed and mechanical activated by high energy milling with 800 rpm (ball to powder ratio 10:1, WC balls) under Ar gas. Filled in vacuum glove box mold powder mix was sintered in the Spark Plasma Sintering Furnace (SPS) with a heating rate of 100 ^{o}C/min in the range of 1000 ^{o}C - 1250 ^{o}C for 8 min under 50 MPa pressure. As a result, the chemical reaction between Ti and C in TiC-Ni cermet with fabrication method of spark plasma reaction sintering has not happened entirely, formation of TiC was not completed at low temperatures of 1000 ^{o}C - 1100 ^{o}C. High porosity leading to a low hardness was also observed at low

sintering temperatures. With the increase of the sintering temperature (above 1200 °C) the reaction is known to be complete and densification reaching 92% has been explained, maximized bending strength of TiC cermet was obtained. Fully connected TiC particles with each other leading to the formation of framework structure were seen when temperature increase to 1300 °C. The more uniform microstructure was the main reason to improve hardness to the maximum. But evaporation of the Ni binding phase and exposed pores were supported with increasing temperature. It has been reported that there is a decrease in bending strength of cermets depending on this situation [39].

A study conducted by Jing and Yisan is about the in-situ production of Fe-TiC composite. Raw materials consisted of 28 wt.% Ti, 7.2 wt.% C, 64.8 wt.% Fe and, mixed by planetary ball milling (ball to powder ratio 6:1, stainless steel balls) at 180 rpm for 24 h. Sintering performances in a vacuum furnace for 1 h of uniaxially pressed samples with a diameter of 16 mm and a height of 10 mm under a pressure of 350 MPa were examined in the 1380 °C – 1440 °C range. The iron base matrix was reinforced with uniformly dispersed in-situ generated TiC particles. The maximum density value was measured from the sample sintered at 1420 °C and, the reason may be explained as improving wettability property between a liquid phase and TiC reinforcement with increasing temperature. On the other hand, during the vacuum sintering process increased temperature can be helpful to easily volatilization of metal and due to occurring voids or pores in sintered samples thereby decreasing densification. The allotropic change reaction schemes described with DTA analysis by Jing and Yisan occurred in the following order; [40].

$$Fe_{\alpha} \rightarrow Fe_{\gamma} \quad \text{at } 765.6\ ^{o}C \tag{1}$$
$$2Fe + Ti \rightarrow Fe_2Ti \quad \text{at } 1078.4\ ^{o}C \tag{2}$$
$$Fe_2Ti_{(molten)} + C \rightarrow TiC + Fe \quad \text{at } 1138.2\ ^{o}C \tag{3}$$
$$Fe_{\gamma} + C \rightarrow Fe_3C \text{ at } \quad 1146.4\ ^{o}C \tag{4}$$

In the research of Olejnik et al., Ti powder (99.95 % purity, 44 μm) and flake graphite (>96 % purity, 3 μm) were used with an atomic ratio of 1:1 for formation in-situ TiC. Moderator has consisted of high chromium cast iron composition and adding 30, 50, 70, and 90 wt.% to control reactive infiltration. Weighted, mixed, dried powder portions are pressed under 500 MPa pressure using a uniaxial hydraulic press. Samples were placed in a mold were filled with molten low alloy middle carbon steel at the

1823 K. As results of the mechanic and chemical characterizations, the local composite reinforcement which was known as in-situ synthesized TiC were obtained by casting molten steel. Limited reactive infiltration and then occurring dimensionally stable composite zones were provided wit the help of the composition of high chromium cast iron used as a moderator. It was observed increasing homogeneity of the microstructure was related to increasing amounts of moderator in the initial powder mixture. The average size of in-situ TiC particles synthesized in the mold with the energy of the casting decreased with increasing percentages of the moderator. Differences in hardness between base alloy and each of composite zones obtained in-situ were more than 200 units [41].

In the study of Zhu et al., in-situ iron matrix composite was produced using exothermic dispersion (XD) method and Fe (40-50 μm), Ti (3-5 μm) and C (3-5 μm) powders with high purity values were used as raw materials. With the help of the reaction equation of Ti+C→TiC, determined TiC volume fraction of 30 vol.% in composite was produced from Fe, Ti, and C powders. Powder mix was exposed to ball-milling for 2 h under vacuum condition and compacted (Ø 30 mm, L 5 mm, at 180 MPa). Heated to 1473 K and then held 10 min cylindrically shaped specimens were cooled down to room temperature in the furnace. According to the thermodynamics analysis, the possible reactions occurred and Gibbs free energy variation of the products of reactions was given below in the Fe-Ti-C system.

$Ti(s) + C(s) = TiC(s)$	$\Delta G^0_{TiC} = -184500+12.17T$	(5)
$3Fe(s) + C(s) = Fe_3C(s)$	$\Delta G^0_{Fe3C} = 25100 -17.02T$	(6)
$2Fe(s) + Ti(s) = Fe_2Ti(s)$	$\Delta G^0_{Fe2Ti} = -87450 +10.73T$	(7)

The formation of possible products as TiC, Fe_3C, and Fe_2Ti and standard Gibbs free energy values depending on the temperature is shown in Fig. 1.3. Since it has the lowest energy, TiC is most likely to occur at all temperatures compared to other products.

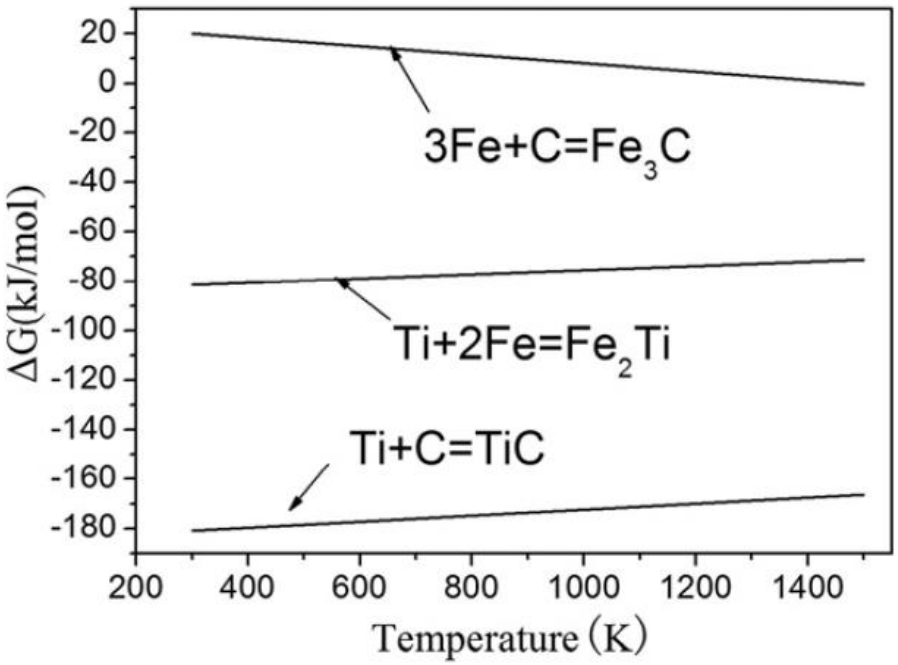


Figure 1.3. Curves of the standard forming Gibbs free energy of the possible products in Fe-Ti-C system as a function of temperature.

As reported in this study, 2586.5 kJ/mol was calculated as the activation energy of reaction to formation 30 wt.% TiC –Fe. This value seems too much than given examples in the literature which have 50 vol.% Fe and pointed out to difficulty of occurrence in Fe, Ti, and C system, so in this case, the reaction was unlikely to occur below 1300 K. The increase in the percentage of matrix absorbed more energy released by the reaction between Ti and C and prevents diffusion between Ti and C. Therefore, the reactivity between Ti and C decreases and the required activation energy value increases. A significantly decreasing reaction times (720 s, 350 s, 120 s) was observed with the increasing heating rates (10 K/min, 20 K/min, 30 K/min), thus chemical reaction rate is linearly related to heating rate. Besides, Fe_3C, Fe in lamellar of perlite and TiC phases were found in the XRD characterization [42].

In the study of Li et al., commercial ferrotitanium (FeTi) (88.6 wt.% purity) and carbon black (99.8 wt.% purity, ~0.1 μm) powders were raw materials. FeTi powders were activated by a high-energy planetary ball mill with stainless steel balls (3:1) in acetone for 2 h. FeTi and C mixtures were obtained by mechanical mixing in acetone for 1 h on the ratio of stoichiometric TiC. After vacuum drying at 50 ^{o}C, compacted about 12 g and with dia. 20 mm under the pressure of 30 MPa specimens were performed for in-situ reaction and densification using spark plasma sintering system

(SPS). Sintering processes were applied as 800-1200 ^{o}C, 80 ^{o}C/min for 5 min with holding pressure of 30 MPa under vacuum. It was found that relative densities of samples increase with sintering temperature, then achieved maximum density observed on specimen sintered at 1150 ^{o}C as 99.2 % with the help of activation of plasma. Liquefied matrix was the main reason to helpful for wettability properties. Nevertheless, high sintering temperature could be hazardous effective on severe volatilization of the liquefied metal matrix under vacuum. The hardness values of sintered cermets are exactly related to the density and the relationship is shown in Fig. 1.4.

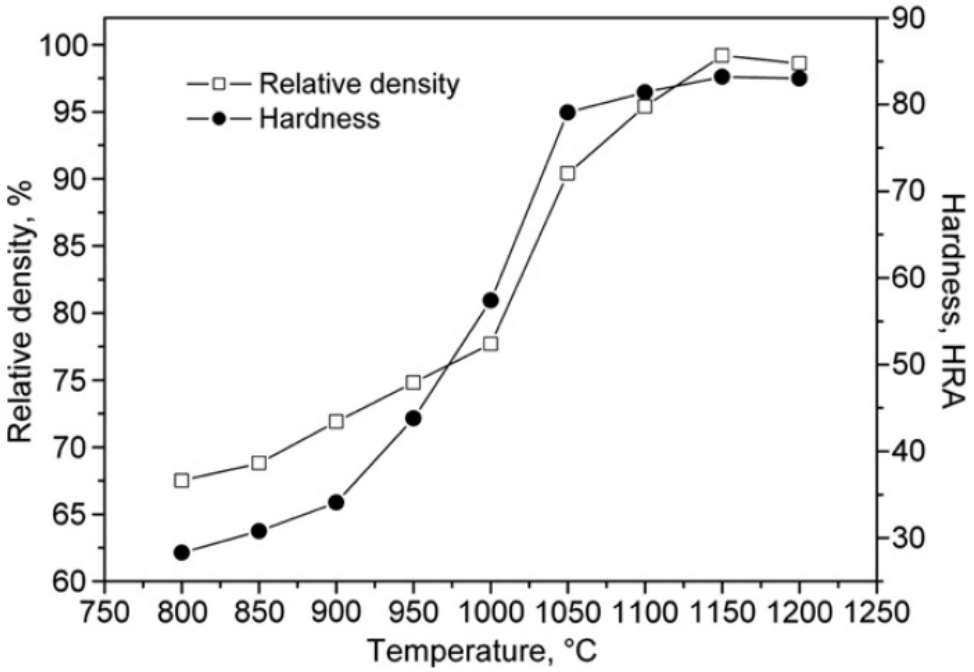


Figure 1.4. Effects of temperature on the relative densities and hardness of the specimens.

XRD diffractions of sintered samples were enough to explain the formation mechanism of in-situ TiC particulates reinforced Fe-based composites from initial reactants (Fe_2Ti and C) and sequences of formation mechanism are listed below.

- A small amount of TiC was formed as a result of the solid-solid diffusion reaction between Fe_2Ti and C below 1000 ^{o}C.

- Solid-liquid solution precipitation in the Fe-Ti-C system was accepted as the second step. The liquid phase emerges from 1085 ^{o}C in the Fe-Fe_2Ti system, but spark plasma activation was effective in observing the liquid phase much earlier. Came out

energy from the exothermic reaction between Ti and C may be supportive to the increasing temperature of the inner side of specimens. Supersaturated Ti and C in liquids can conduce to nucleation of TiC, then formatted and precipitated TiC from the liquid may be distributed homogeneously as spherical particulars about 1 μm.

The formation of in-situ TiC reinforced Fe- based composites was consist of a combination of solid-solid and solid-liquid reactions pronounced as hybrid formation mechanism [43].

It is illustrated by Yang's work, 20 wt.% Ni (99.5 % purity, 45 μm), 64 wt.% Ti (99.5 % purity, 25 μm) and three different 14 wt.% graphite (99.5 % purity, (1) ~ 150 μm, (2) ~ 38 μm, (3) ~ 1 μm) were used as raw materials to mixing for 8 h and pressed like cylindrical preforms (Ø 20 mm) until reached 75 % of theoretical density. Placed preforms into SHS combustion chamber were ignited with the help of arc and heated on the graphite flat. It has been shown in Fig. 1.5., that the decreases in the particle size of the carbon, then the increase in the combustion temperature, and the decrease in the ignition time are directly proportional. The contact surface area increasing as the grain size gets thinner is explained as the reason for the acceleration of the surface reaction between Ti and C. The increase in the reaction progress velocity reduces the effect of the constant heat loss and therefore the combustion temperature increases by accumulating.

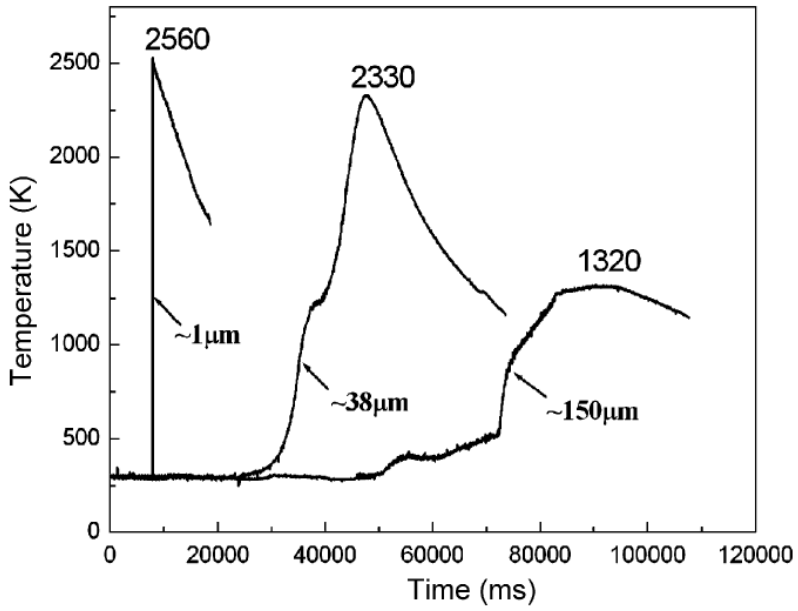


Figure 1.5. The temperature–time profiles of 20 wt.% Ni–Ti–C systems with different C particle sizes (~1 μm, ~38 μm and ~150 μm) during SHS process.

The SEM and XRD characterizations resulted in the usage of ~1 μm C any intermediate phases were not observed. But in the usage of ~38 μm C a small amount of $TiNi_3$, in the usage of ~150 μm C a large amount of Ti_2Ni and also unreacted Ti and C phases were detected. This situation was directly related to the exothermic reaction performances of the powder mixtures [44].

In the study of Lee et al, selected raw materials consisted of powders, carbon black (50-100 nm), titanium hydride (TiH_2, A.P.S. ~ <10 μm), and atomized Fe-based AISI D2 steel (A.P.S. ~ <7 μm). Powder mix was prepared with the help of wet ball milling for 40 h (60 rpm, 5:1 Ø 9 mm steel ball/powder ratio, *n*-hexane medium). For targeted 30% TiC concentration, added carbon black and TiH_2 were calculated to acquire C/Ti ratios of 0.8, 0.9, 1, and 1.1 in the mixture. Uniaxial pressed preforms under 5 MPa were sintered with a heating rate of 4 ^oC/min at1400 ^oC for 1 h in the vacuum of 10 Pa. For densification sintered samples it was utilized the hot isostatic press (HIP) at at 1320 ^oC for 1.5 h under the pressure of 118 MPa Ar atmosphere. As given in Table 1.6, the results of the study were explained following. In the comparison of unreinforced Fe-based steel alloy and in-situ TiC-Fe alloy composites structure, the difference in values of the mechanical properties was determined, so this reason was explained with in-situ TiC. Higher values can be achieved when the C/Ti ratio of the reactant was closer to gets similar to the stoichiometry of the in-situ synthesized TiC. However, one of the causes of the decrease in stiffness and flexural strength is that the unreacted carbon from the excess carbon source disrupts the matrix structure. In the case of used less C in the C/Ti ratio, to complement the carbon deficiency of stoichiometric TiC needed carbon is provided by matrix and it also causes reductions in mechanical properties [45].

Table 1.6. Effects of used C /Ti ratio of in-situ TiC/Fe alloy composites on mechanical properties.

	Hardness (HRc)	Flexural strength (MPa)	Flexural strain (%)
C/Ti = 1.1	66.8 ± 0.6	1219 ± 53	1.99 ± 0.06
C/Ti = 1	67.0 ± 0.6	1247 ± 35	2.05 ± 0.03
C/Ti = 0.9	67.4 ± 0.3	1394 ± 65	2.30 ± 0.14
C/Ti = 0.8	63.7 ± 0.3	1547 ± 140	2.68 ± 0.04
Unreinforced Fe alloy	60.7 ± 0.3	1360 ± 40	2.33 ± 0.2

In the study of Li et al., selected raw materials were commercial powders three different Ti content included ferrotitanium (FeTi) (~44 μm, (1) 28 wt.% FeTi, (2) 48 wt.% FeTi, (3) 68 wt.% FeTi) and carbon powder (~38 μm, 99.5 % purity). FeTi powders were mixed with carbon powders at the rate of the corresponding stoichiometry of TiC with the help of a mechanical rotator (steel jar, S.S ball/powder 5:1, 40rpm, 6 h). Pressed cylindrical preforms (Ø 20, 8 ±1 mm) by 70-75 MPa were dried in a vacuum oven at 300 oC for 3 h. After placed preforms in a sand mold, the SHS reaction to obtain in-situ TiC was started with the help of heat energy of molten low alloyed steel (~1600 ^{o}C) to consist matrix of the cermet. The outputs shared by the researchers, as a result, are as follows, it has been observed that 2 different types of TiC particles synthesized by different mechanisms are partially uniform distributed in locally strengthened regions [3]. The first of these types, the large rectangular TiC particles, have an average size of 2 μm and above. Occurred as mainly present this type TiC in the local reinforcing region of the composite which was consisted from (28 Ti, Fe)-C system and observed in matrix region nearby the interface between steel and reinforcing region was composed by the nucleation growth mechanism through the contact reaction region.Another type of TiC – fine spherical/near-spherical shaped particulates which are fabricated by solution and precipitation mechanism during SHS reaction, are mainly existent in the reinforcing region. Increasing Ti contents in reactant of ferrotitanium are effective on the growth of average particle size of TiC, for example as the range of 28-48 % to ~0.1-0.5 μm, 48-68 % to ~0.5-1 μm.

2. MATERIALS AND METHODS

2.1. Properties of Reactant Powders

In this thesis, TiC was the reinforcement phase synthesized from titanium (Ti) and graphite (c) powders by the reactive sintering method, and iron (Fe) powder as the matrix phase was chosen. The production process of reactive sintered TiC based cermets was started with the selection of raw material powders and their characterization. Chemical analysis, particle size calculations, and phase structures of the reactant powders were examined, respectively.

Powders used in this study were supplied by Nanografi Nano Teknoloji A.Ş. Given in Table 2.1., the chemical composition of metallic raw material was analyzed with Thermo Scientific Niton XL5 800 device using the XRF technique. The chemical contents of graphite powder were also shared in Table 2.1., as a result of the analyses made by the supplier.

Table 2.1. Chemical composition of raw powder materials, a) Fe, b) Ti, c) Graphite.

a) Fe powder

Fe %	Ni %	Si %	Mn %	Cu %	Cr %	P %	Sn %	Mo %
96.65	1.29	0.55	0.24	0.3	0.29	0.24	0.18	0.17

b) Ti powder

Ti %	Fe %	V %	Zr %	Cu %	Al %	Ni %	Si %	Mo %
98.16	0.42	0.40	0.34	0.18	0.18	0.17	0.08	0.07

c) Graphite powder

Graphite %	Ash %	Moisture %	Sulphur %
≥ 99.99	< 0.01	<0.003	<0.002

Particle size and distribution of powder as metallic raw materials were examined with Microtrac S3500 particle size measuring device. The average particle size of graphite powder was also shared in Table 2.2., as a result of the analyses made by the supplier.

Table 2.2. The average particle size of raw materials.

Raw Materials	A.P.S. (μm)
Fe	60.03
Ti	50.54
C	1

X-ray diffraction spectrometry analysis method was used to determine the phases contained in metallic powders, the patterns obtained were provided by the PANalytical EMPYREAN Series 2 XRD device.

The metallic powders used were also examined with scanning electron microscopy (SEM-EDS, Vega Tescan - Bruker) technique. In these examinations, the particle size, distribution, geometric shapes, and chemical content of the powders were investigated. The micrographs at 100X, 250X, 500X, 1000X, 2500X magnifications and EDS analysis from 3 different points of reactant powders were obtained by the SEM.

2.2. Production Process of Cermets

The production process of reactive sintering of TiC-based cermets was planned according to the parameters specified in Table 2.3. below and carried following the production scheme given in Fig. 2.1. The total weight of titanium and carbon defined as reactive reactants in terms of chemical content ranges from 30%, 50%, 70%, and cermet structures were completed by the iron base alloy as a matrix.

Table 2.3. Chemical compositions of reactive sintering of TiC-based cermets.

Sample Code	Reinforcement Reactant Content Matrix Content		
	Ti (wt.%)	C (wt.%)	Fe (wt.%)
KB 1200-3	24	6	70
KB 1200-5	40	10	50
KB 1200-7	56	14	30
KB 1275-3	24	6	70
KB 1275-5	40	10	50
KB 1275-7	56	14	30
KB 1350-3	24	6	70
KB 1350-5	40	10	50
KB 1350-7	56	14	30
KB 1425-3	24	6	70
KB 1425-5	40	10	50
KB 1425-7	56	14	30
KB 1500-3	24	6	70
KB 1500-5	40	10	50
KB 1500-7	56	14	30

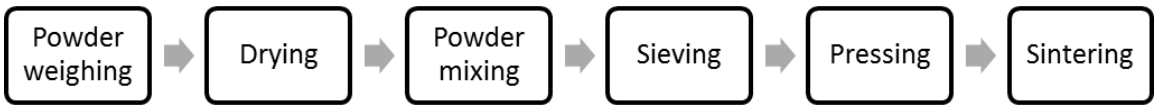


Figure 2.1. Production scheme of the reactive sintering of the TiC-based cermets.

The weighed powders were dried at 105 ^{o}C for 2 h in the drying oven. Dried powders were mixed in a cylindrical plastic container (Ø 10 cm, height 20 cm) as determined proportions with 3-5 mm diameter alumina balls in a ratio of 1:1 by weight. Containers with 30% occupancy were rotated for 12 hours in a uniaxial mixer rotating at 50 rpm in the horizontal axis, Fig.2.2. The powder mixture was sieved through a 1 mm sieve at 100 rpm for 5 minutes and separated from the balls. Sieving was applied at the same time to re-decompose the agglomerated powders that may have formed during mixing to achieve more homogeneity. In the next step, powder mix was pressed under unidirectional pressure of 600 Mpa and shaped samples in weighing 3 g were obtained. The press mold was designed in 3 parts (upper, lower jaw, and body) and

was manufactured from DIN 1.2379 steel to obtain a hardness of 60 HRc. All moving surfaces were subjected to smooth grinding. Any binders and lubricants were not used in the compression process, Fig. 2.3.



Figure 2.2. Uniaxial mixing for preparation of powder mix.



a)



b)

Figure 2.3. Powder preforming equipments, a) Compression mold, b) Hydraulic press.

Filled powder mix to press mold took the form of coin in15 mm diameter as a result of the compression process between the upper and lower jaws. The thickness of the coin-shaped samples was decreased from 5 mm to 3 mm in proportion to the increased iron content in the powder mix. As also shown in Fig. 2.4., the change in dimension is directly related to the density of cermet composition.

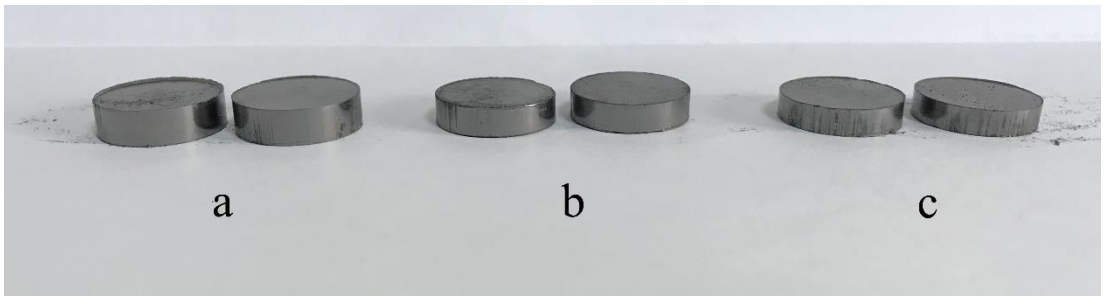


Figure 2.4. Examples for shaped green cermets, a) KB 1200-3 b) KB 1200-5 c) KB 1200-7

The shaped specimens were placed in the center of the furnace for sintering on graphite pads. Preformed green cermet groups were sintered in 5 different sintering temperatures increasing 75 ^{o}C between the ranges of 1200-1500 ^{o}C. After the samples were placed in the furnace, the sintering furnace was first vacuumed at 2 mbar. The vacuuming process was repeated twice and the oxygen in the environment was tried to be minimized. Argon gas with hydrogen addition was used in all processes. The heating, holding and even cooling parts of the sintering process were all carried out under 0.5 L/min flow of 5 vol.% H_2 + Ar gas mixture. During the sintering processes, a constant heating rate of 10 ^{o}C/min and 60 min holding time was applied to all samples. The cooling was started from the end of the heating regime and continued until the temperature of the furnace dropped to 60 ^{o}C supported by the effect of gas flow. Vacuum and atmosphere controlled furnace VF_1700 supplied by MSE company was used in the sintering process.



Figure 2.5. Cermet samples after sintering.

2.1. Characterization Methods of Cermets

The densities of the sintered samples were calculated based on the Archimedes density measurement method. In addition to the Archimedes method, samples were weighed first and then boiled in distilled water for 2 hours and cooled to room temperature before density measurement. This stage is especially applied in the density measurement of porous ceramics, and by ensuring that the pores are filled with water, the bulk density of the material is calculated more accurately. After removing the water on the surface of the sintered samples extracted from boiled and cooled water, density measurement by Archimedes method was measured with a precision scale. With this method, density measurement is calculated based on the formulation below.

M_d (dry weight in air, g);
M_w (wet weight in air, g);
M_{ww} (wet weight in water, g);
V (volume, cm^3);
ρ_{bulk} (bulk density, g/cm^3);

$$\rho_{bulk} = \left(\frac{M_d}{M_w - M_{ww}}\right) / V$$

Thermomac TM 19-D hot plate was used in the boiling stage of the density measurement, and Precisa LS 220A precision scale with Archimedes density measurement kit was used in the weighing stage. The calculated bulk densities of the sintered samples were also compared with the theoretical density of TiC + Fe in the same chemical composition, and the relative density was calculated.

Sintered samples were subjected to grinding for surface examinations and hardness measurements. Grinding of the sample surfaces was carried out with diamond particulate ceramic grinding disc and with SiC grinding paper, respectively. Abrasive grain sizes, rotation speeds, and times applied in coarse and fine grinding are given in Table 2.4. below. All stages of the surface preparation process were done manually in ATM Saphir 250 M2 device.

Table 2.4. Grinding parameters applied in surface preparation.

No:	Grinding types	Abrasive grain sizes (μm, grit)		Rotation speed (rpm)	Time (s)
Coarse Grinding					
1	Ceramic grinder	125	132	300	120
2	Ceramic grinder	54	322	300	120
Fine Grinding					
3	Grinding paper	30	600	300	300
4	Grinding paper	18	1000	300	300
5	Grinding paper	8	2500	600	420
6	Grinding paper	5	4000	600	420

A hardness measurement of sintered samples was performed by using the Qness Q250c device and Vickers measurement method. The diagonal lengths of the impression obtained from the measurements performed by applying 1 kgf (HV1) force were measured by the hardness device and the hardness results values were calculated based on the formulation given below. The indenter employed in the Vickers test is a square-based pyramid whose opposite sides meet at the apex at an angle of 136°.

F (applied load, kgf);
d (average of two diagonals, mm);
HV (hardness in Vickers, HV);

$$HV = 1.854\, x\, \frac{F}{D^2}$$

Sintered cermet samples were subjected to some pre-preparation processes before surface examinations. To obtain more accurate results, cermet samples in coin form were cut in half in a semicircle before the optical examination. The cutting process was carried out by the electrical discharge machining (EDM) method using molybdenum wire. The plastering of the wire material on the cutting surface, which can be defined as the disadvantage of the method, was removed by the grinding process as stated above. Samples cut in a semicircle were first cold molded to aid in surface imaging techniques. Optical microscope samples prepared from sintered cermets were examined and imaged at magnifications of 50X, 100X, 200X, 500X, and 1000X respectively. Significant outcomes and findings were attempted to be obtained by performing examinations of matrix-reinforcement phases and their distribution, porous and dense areas, and other microstructures. Nikon Eclipse E600 optical microscope was used for these examinations.

The X-Ray Diffraction (XRD) characterization of cermets produced by the reactive sintering method was performed. The phases formed via the reaction between pure titanium, carbon, and iron powders after sintering were investigated. The results of the reinforcement phase and matrix have been tried to obtained and explained with the effect of variables such as different chemical composition ratios and sintering temperatures by the XRD analysis method. The phases of sintered cermet samples were identified in the range of 5 – 90^{o} by using Rigaku D/Max 2200 X-ray diffractometry Cu (40 kV, 40mA) radiation.

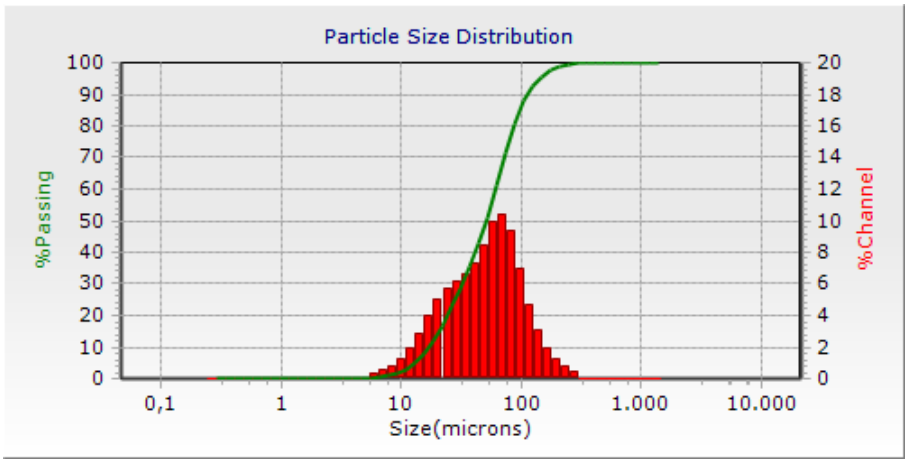
The examinations of titanium carbide based cermets produced by reactive sintering were finished out with help of a scanning electron microscope (SEM). In this examination, micrographs of cermet samples were obtained at 125X, 250X, 500X, 1000X, 2000X, 5000X, and 10000X magnification, respectively, using the Philips XL 30S FEG SEM device. The energy-dispersive X-ray spectroscopy technique was used to determine chemically differentiates between the inside of reactive sintered TiC grain and intergranular matrix. At the same time, the elemental distribution of the cermet sample having the optimum mechanical and density values was examined with the SEM - Elemental mapping mode. Also, the particle size of TiCs formed in the cermet structure was measured using SEM micrographs at 5000X magnification.

Thermochemical modeling studies were done by using HSC Chemistry 6.12 software to simulate possible products for the expected 30%, 50%, and 70% TiC and the iron matrix. The graphics were plotted by using the ‘‘Equilibrium Compositions’’ module to determine molar ratios of possible products with an increase in temperature from 1100 ºC to 1600 ºC. The module uses the Gibbs minimization method for calculations.

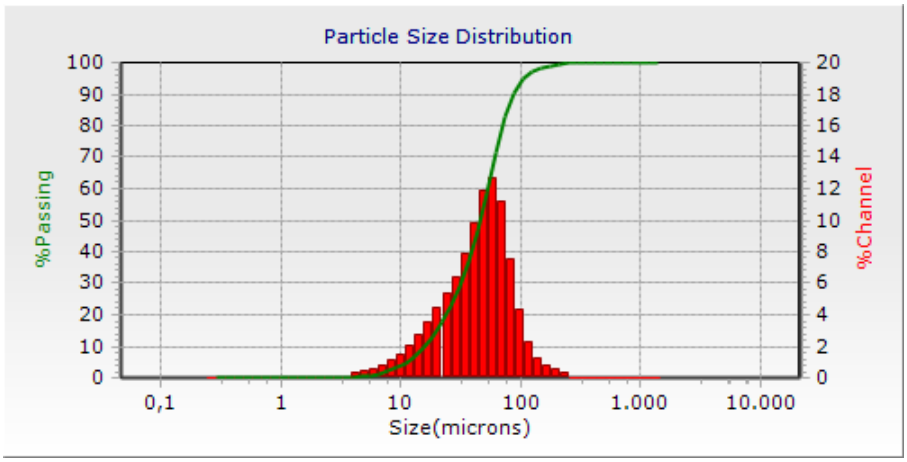
3. RESULTS AND DISCUSSIONS

3.1. Characterization of the Reactant Powders

In Fig. 3.1., the measurement results of the average particle size and distribution of iron and titanium powders are given. It was determined that the average size of iron powder was 60 µm, and the average size of titanium powder was 50 µm.



(a)

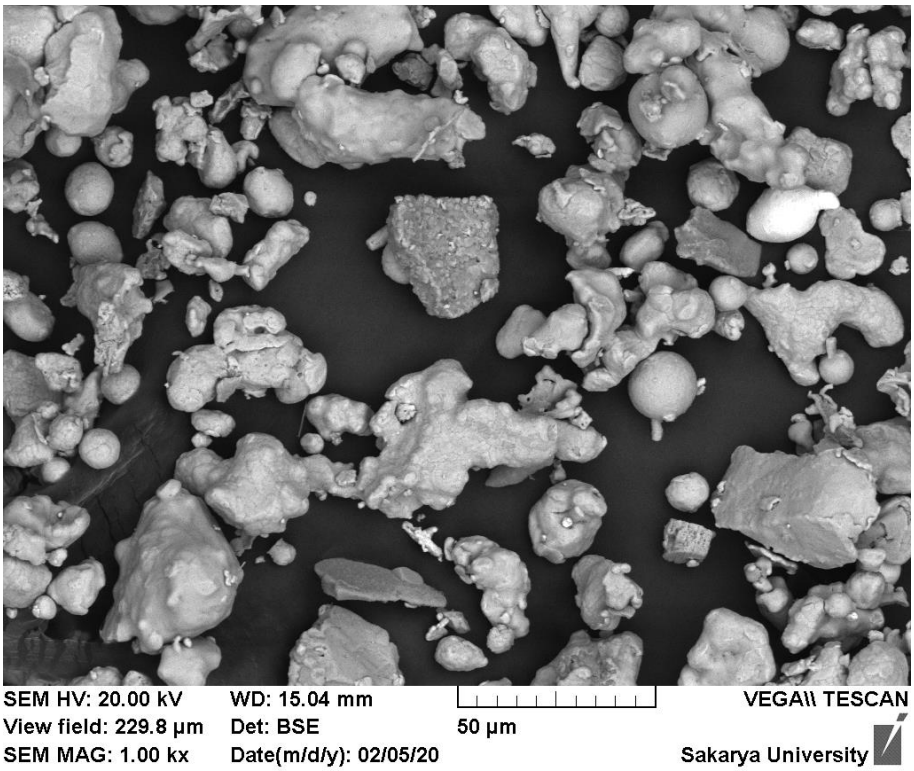


(b)

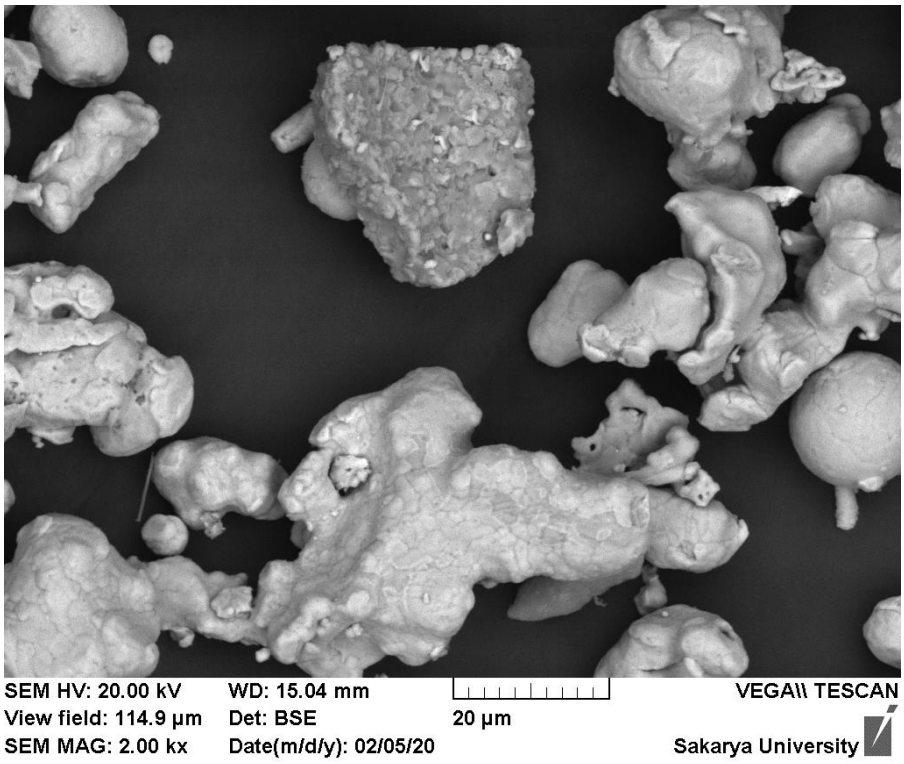
Figure 3.1. The average particle size distribution of metallic powders, a) Fe and b) Ti.

SEM micrographs of reactant powders were examined in detail. As a result of examining the geometric forms of the powder particles with this method, it is seen in

the micrographs that the Fe powder consists of almost spherical powders, in Fig. 3.2. The dimensions of the displayed iron powders correspond to the values obtained by the average grain size and distribution analysis. According to the EDS analysis result taken from a few particles, iron powder consists almost entirely of iron metal, given in Fig. 3.3. However, in the analysis of some particles, superficial oxidization has been observed. These results are consistent with the results of XRD analysis.

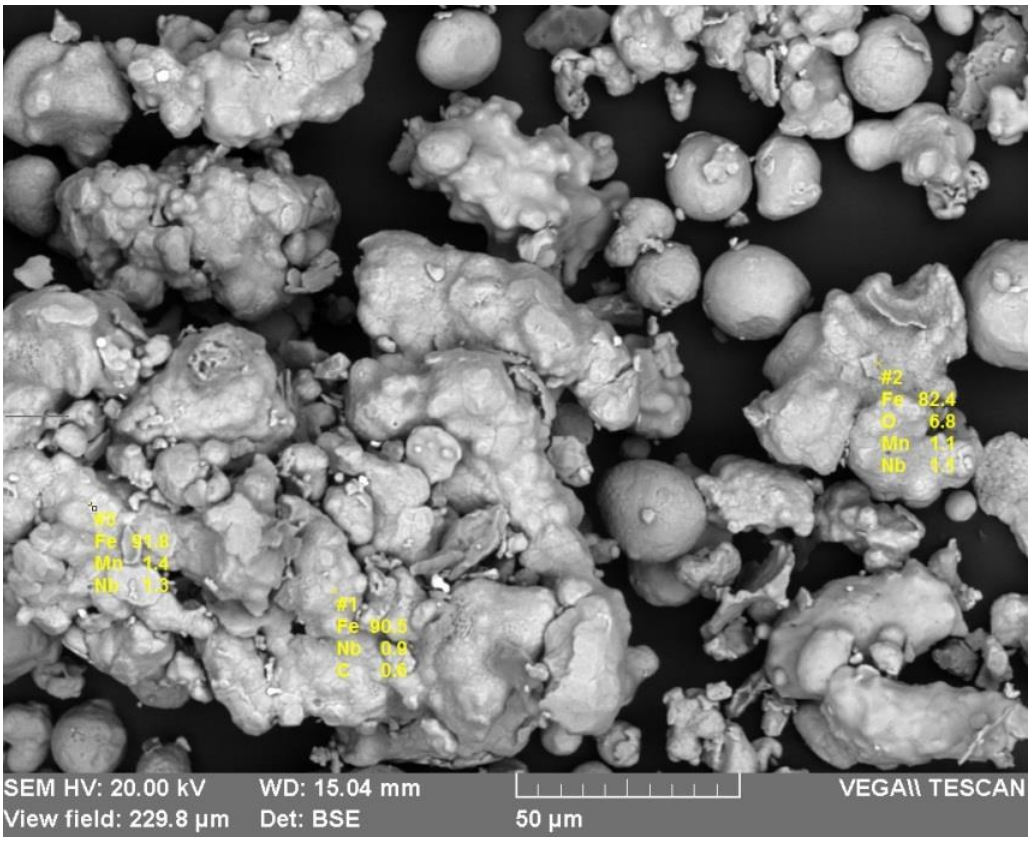


(a)



(b)

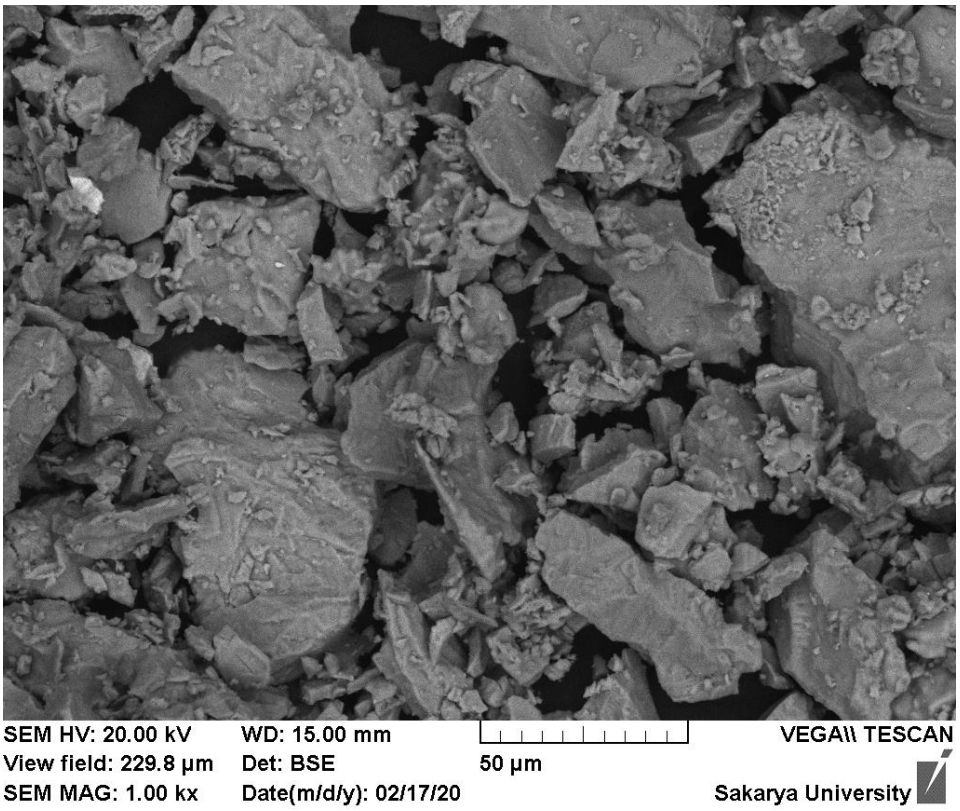
Figure 3.2. SEM micrographs of Fe powder, a) 1000X, b) 2000X.



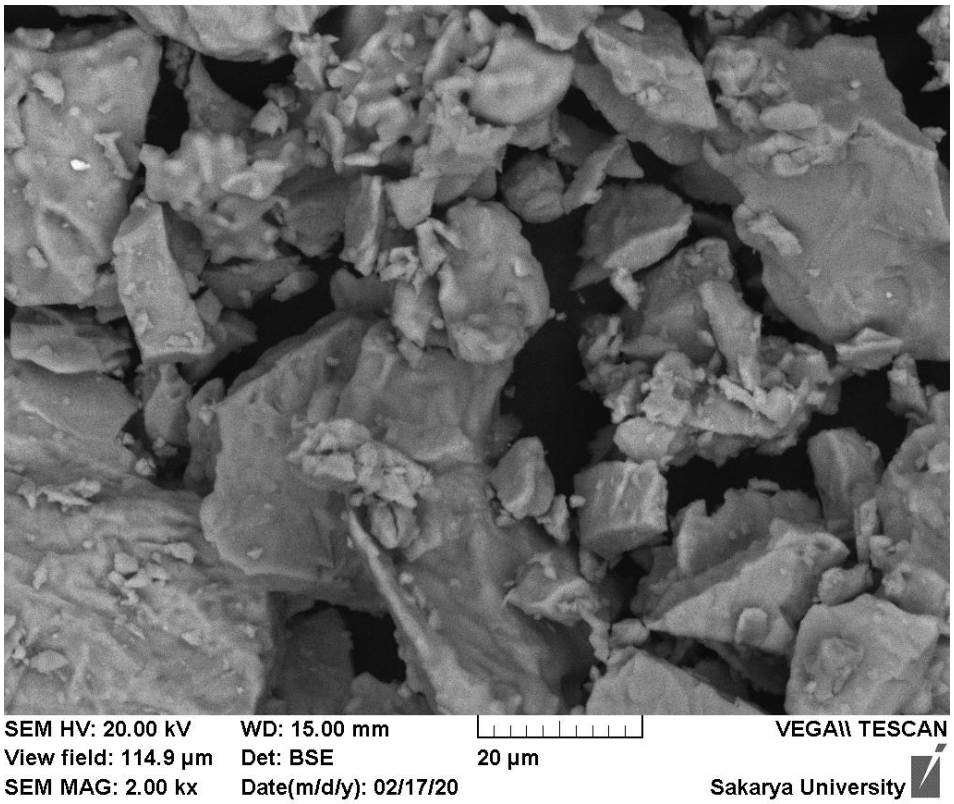
Point	Fe %	Mn %	Nb %	C %	O %
#1	90.5	-	0.9	0.6	-
#2	82.4	1.1	1.1	-	6.8
#3	91.8	1.4	1.3	-	-

Figure 3.3. SEM-EDS results of Fe powder.

It is seen in the micrographs that the Ti powder consists of almost angular powders, in Fig. 3.4. Although it is angular, the powder dimensions of titanium correspond to the measurements calculated by the particle size and distribution measuring device. It was observed that all of the particles, which were measured by EDS analysis in Fig. 3.5., were of titanium element.

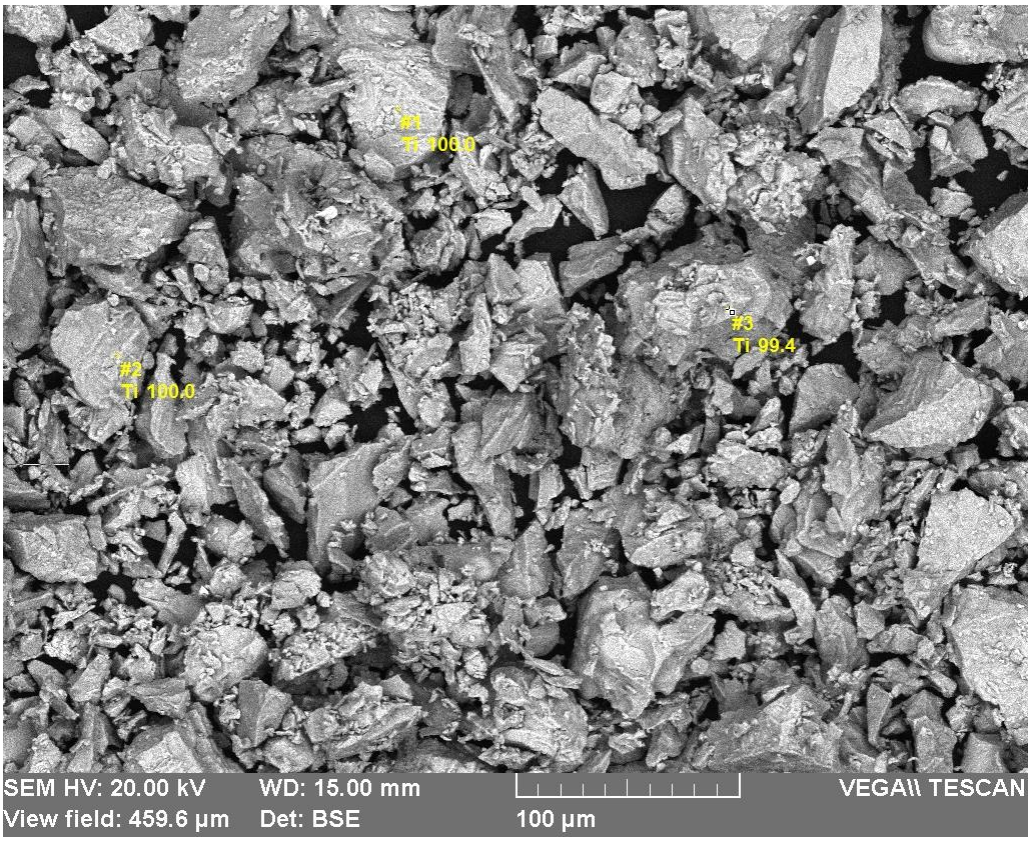


(a)



(b)

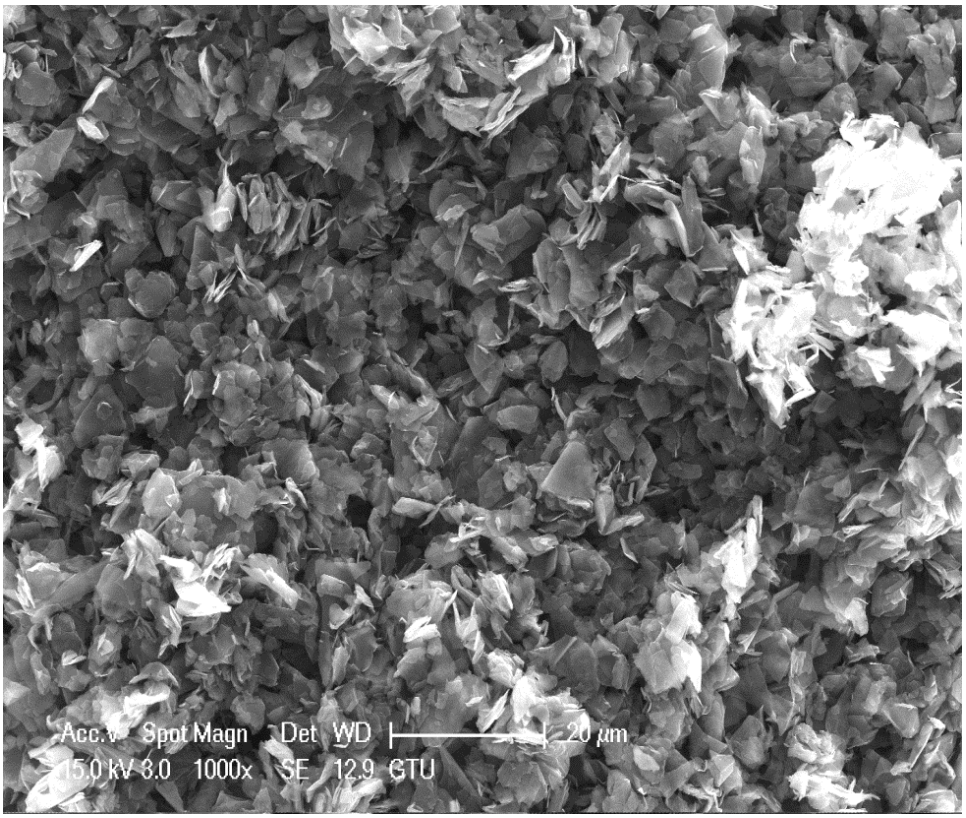
Figure 3.4. SEM micrographs of Ti powder, a) 1000X, b) 2000X.



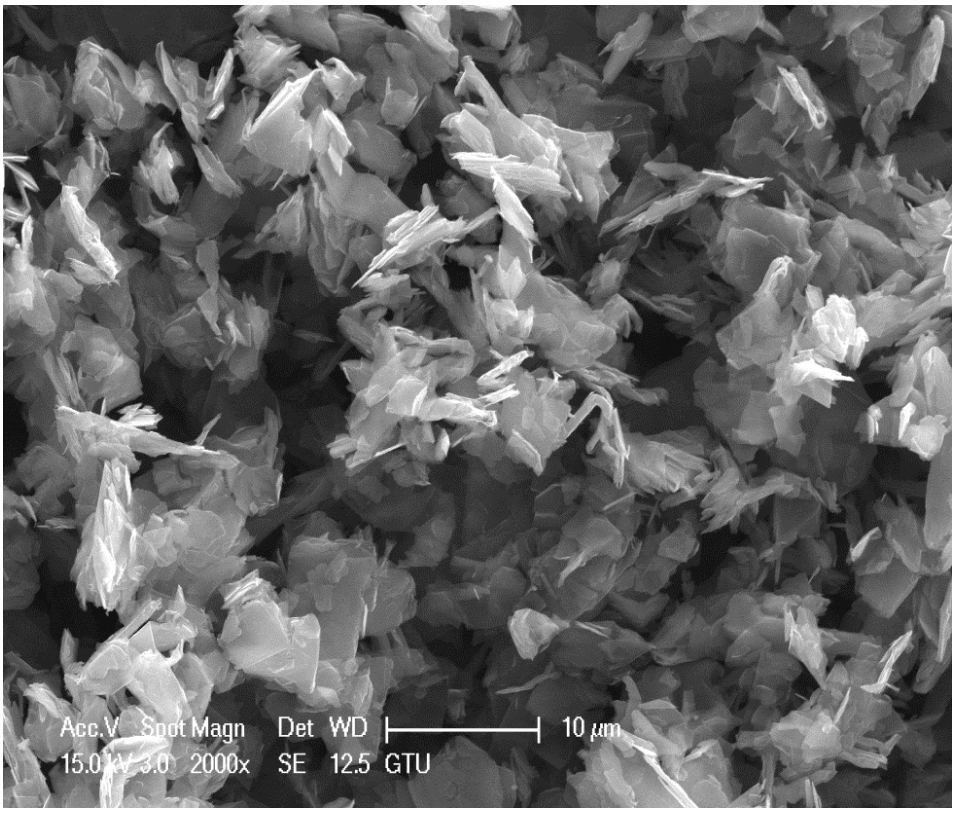
Point	Ti %	Nb %
#1	100	-
#2	100	-
#3	99.4	0.6

Figure 3.5. SEM-EDS results of Ti powder.

Fig. 3.6 shows the micrographs of graphite powder used as a carbon source. Based on the detailed examination of the imaged micrographs, it was observed that the average particle size of the graphite powders was around 1 µm.



(a)



(b)

Figure 3.6. SEM micrographs of graphite powder, a) 1000X, b) 2000X.

At the analysis of the XRD patterns of used powders were not encountered different phases than Fe, Ti and C in Fig. 3.7.

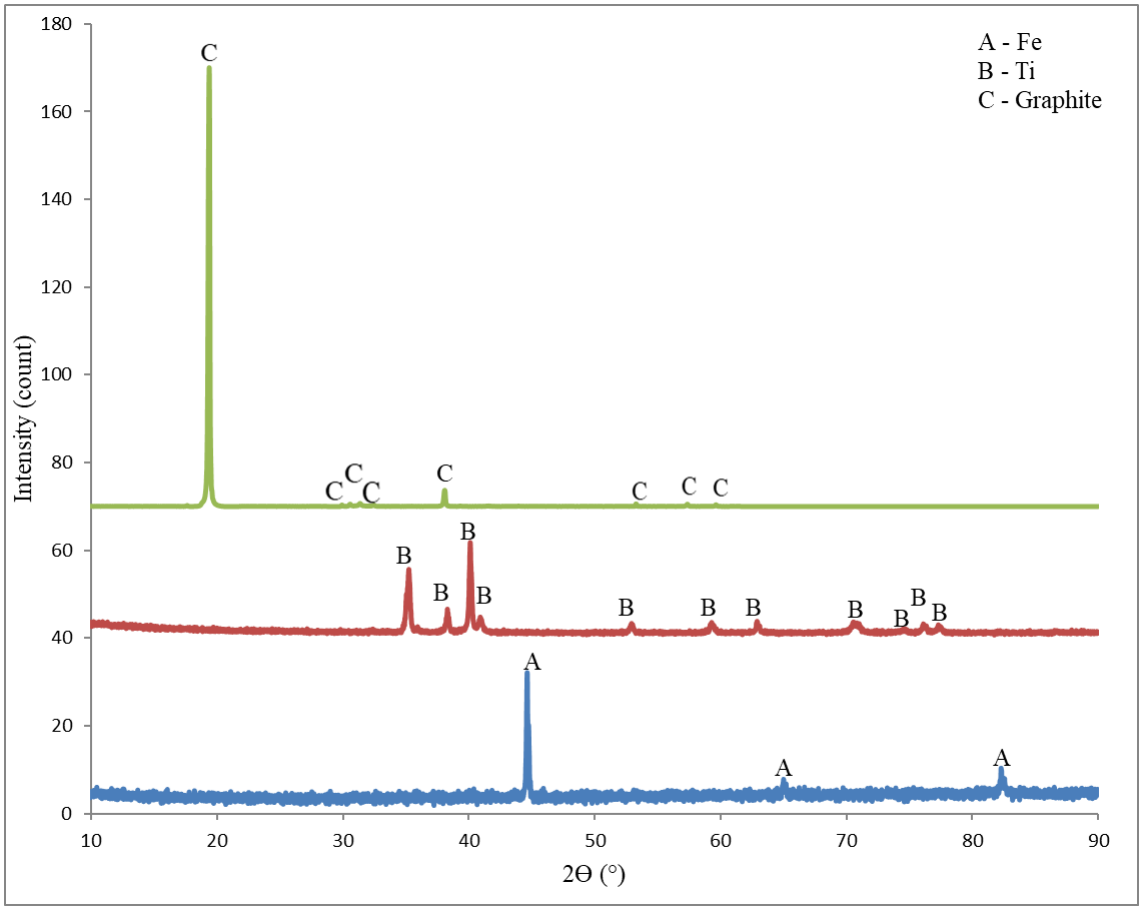
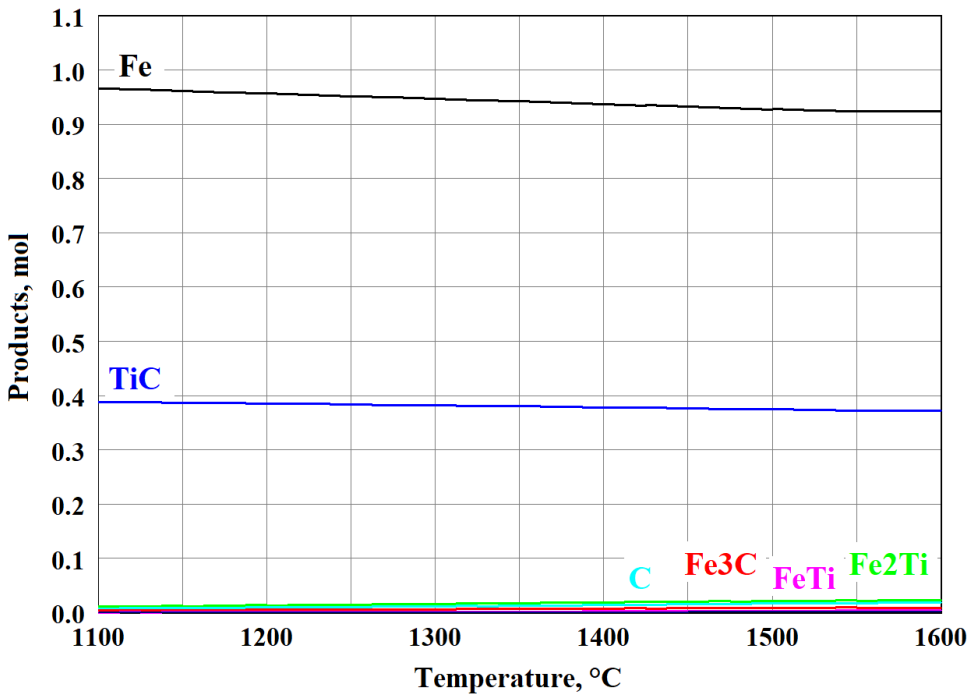


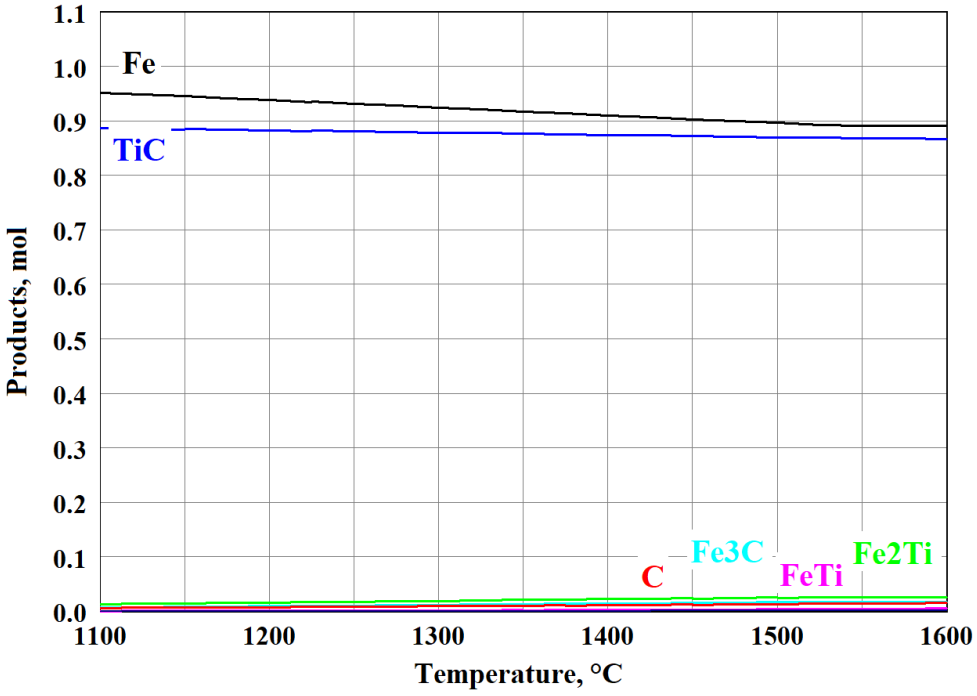
Figure 3.7. XRD patterns of reactant powders.

3.2. Thermochemical Modelling of the Cermets

As shown in Fig. 3.8., it is seen that TiC and Fe phases are formed by the targeted ratios (30%, 50%, and 70% TiC) in the sintering temperature range of 1100-1600 ºC. However, it was determined that C, Fe3C, FeTi, and Fe2Ti phases could also be formed in modeling graphics together with TiC and iron phases as a result of the reaction. Besides, it is seen that the amounts of these phases that will occur as a result of the reaction can be negligible. The sintering time is also known as another effective parameter on the phase structure of the cermet samples together with sintering temperature, so it can change the diffusion balances and further decrease the number of undesired phases to be formed in the final product.

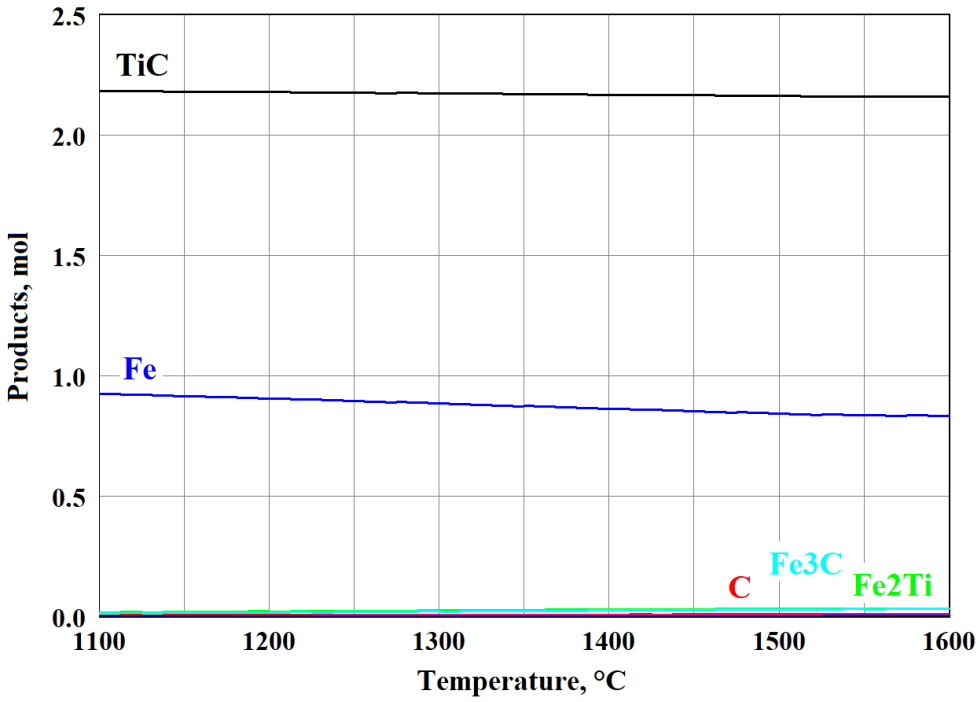


(a)



(b)

Figure 3.8. Results of thermochemical modeling for the different variations of TiC in the iron matrix, a) 30%, b) 50% and c) 70% TiC.



(c)

Figure 3.8. Results of thermochemical modeling for the different variation of TiC in the iron matrix, a) 30%, b) 50% and c) 70% TiC (continuum).

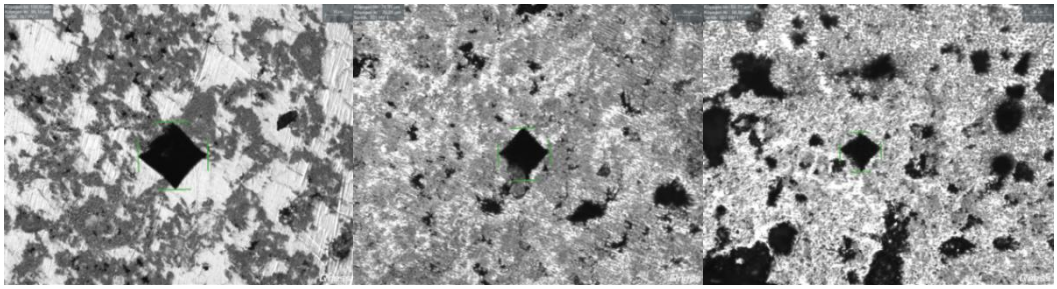
3.3. Hardness of the Cermets

As for all three chemical composites, the hardness of the sintered cermet samples increased at almost all temperatures, so this conclusion is based on the values given in Table 3.1. It was observed that the hardness of the samples with 30 % Ti + C content continuously increased depending on the temperature, and this increase accelerated between 1275 - 1425 ºC. The minimum hardness value of cermet samples with this composition was measured as 247.14 HV1 with (S.D. 86.44) at 1200 ºC, and the highest hardness value was measured as 463.50 HV1 (S.D. 65.12) at 1500 ºC. As shown in Fig. 3.4., in the examination of cermet samples with 50 % Ti + C composition, it was concluded that the inclination of the hardness values in the sintering temperature range of 1200-1350 ºC was close to the horizontal, and this slope increased in the range of 1350-1500 ºC. The lowest hardness value measured from cermet samples in this composition is 335.17 HV1 (S.D. 78.36) at 1275 ºC, and the highest hardness value is 538 HV1 (S.D. 68.16) at 1500 ºC. Except for the results obtained at 1350 ºC, a continuous increase was observed in the measurement of the

hardness of cermet samples, of which 70% of the content is Ti and C. Starting from 307.33 HV 1 (S.D. 59.24) at 1200 ^{o}C, this slope climbed up to 590 HV1 (S.D. 98.31) at 1500 ^{o}C.

Table 3.1. The average measured hardness and standard deviation values of the cermets.

Hardness (HV)			
Sample Code	-3	-5	-7
KB 1200	247 ± 86	355 ± 14	307 ± 59
KB 1275	273 ± 28	335 ± 78	376 ± 72
KB 1350	362 ± 81	379 ± 76	342 ± 57
KB 1425	456 ± 39	495 ± 37	433 ± 58
KB 1500	463 ± 65	538 ± 68	590 ± 98



(a) (b) (c)

Figure 3.9. Examples for hardness indents, a) KB 1200-3, b) KB 1350-5, c) KB 1500-7.

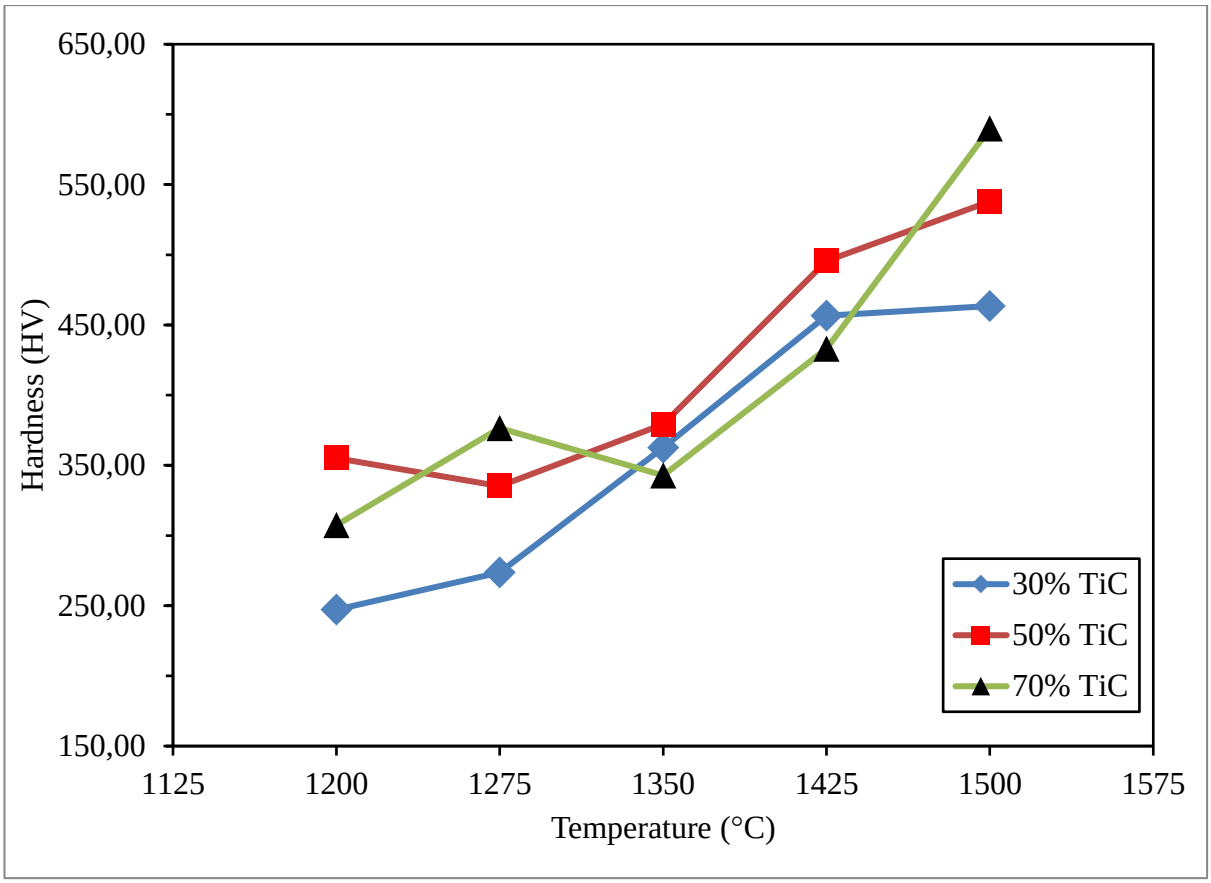


Figure 3.10. Hardness change of the cermets depending on sintering temperature.

3.4. Density of the Cermets

According to the density values shown in Table 3.2., and plotted in Fig. 3.11., in examining the measured density values of sintered cermets, it was observed that the density values decreased and then increased depending on the temperature increase, regardless of the chemical composition. After sintering of cermets containing 30% Ti + C, the average of the measured density values started at 4.99 g/cm^3 at 1200 ºC and decreased to 4.89 g/cm^3 at 1350 ºC, respectively, with increasing temperature, then the observed increase in density values was 5.09 g/cm^{-3} at 1500 ºC. The sample with the highest density of cermet samples containing 30% Ti + C was the sample with code KB-1500-3 and reached 72.75% of the calculated theoretical density. When the densities of cermet samples made of 50% Ti + C were compared with the increasing sintering temperature, it was observed that the average density value starting from 3.97 g/cm^3 at 1200 ºC decreased to 3.87 g/cm^3 at 1275 ºC and then increased to 4.62 g/cm^3 at 1500 ºC maximum value and at the same time the relative density value of this

maximum density value was calculated to be 72.14% (sample code: KB-1500-5). In the cermet sample series containing 70% Ti + C, the density increase starting from 3.18 g/cm^3 at 1200 ^{o}C increased to 3.28 g/cm^3 at 1275 ^{o}C, then the density of 3.23 g/cm^3, the lowest value was measured at 1350 ^{o}C. The increase continued up to 1500 ^{o}C and the measured 3.48 g/cm^3 density value of the KB-1500-7 sample was reached a relative density of 59.90% as the densest of the series.

Table 3.2. The average measured bulk and relative density values of the samples.

Density (g/cm3)				Relative Density (%)			
	-3	-5	-7		-3	-5	-7
KB 1200	4.99	3.97	3.18	KB 1200	71	62	55
KB 1275	4.94	3.87	3.28	KB 1275	71	61	56
KB 1350	4.89	3.92	3.23	KB 1350	70	61	56
KB 1425	5.03	4.29	3.33	KB 1425	72	67	57
KB 1500	5.09	4.62	3.48	KB 1500	73	72	60

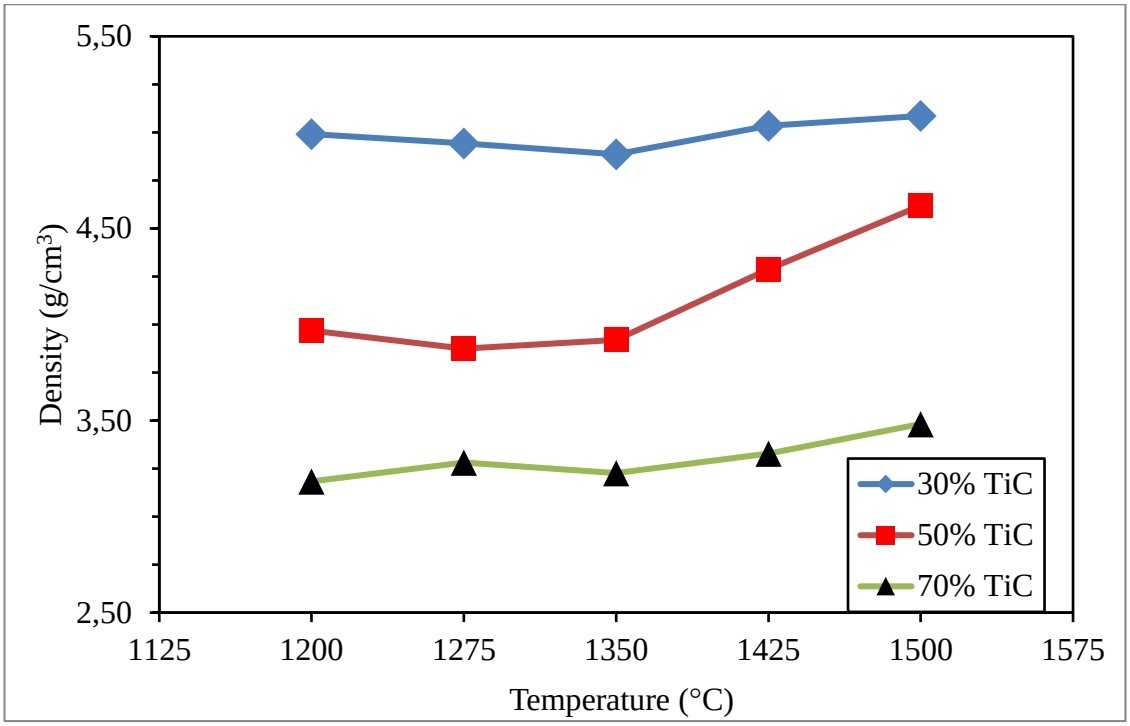


Figure 3.11. Density change of the cermets depending on sintering temperature.

3.5. XRD Analysis of Cermets

XRD patterns of cermet samples according to chemical composition are given in Fig. 3.12., Fig. 3.13. and Fig. 3.14., respectively. The XRD patterns of the cermet samples grouped according to the sintering temperature are given in Fig. 3.15., Fig. 3.16., Fig. 3.17., Fig. 3.18., and Fig. 3.19., respectively. Peaks of titanium carbide and iron phases were seen in XRD patterns of all 15 samples. It was proved that the SHS reaction between Ti and C at all temperatures and compositions started, progressed, and completed without any problems. Graphite peaks were determined only in the pattern of the KB 1200-7 coded sample with low sintering temperature and 70 % Ti + C composition. When analyzing the XRD patterns, it was observed that there is proportionality between the peak intensities of TiC and Fe phases. As it is seen in the XRD pattern graphs plotted according to the chemical composition, this proportionality changes only according to the increasing amount of Ti and C. As is also clearly shown by the XRD pattern graphs plotted based on the sintering temperatures, the temperature change is not effective on proportionality. Another meaning of this proportionality was that all reaction results met the expectations.

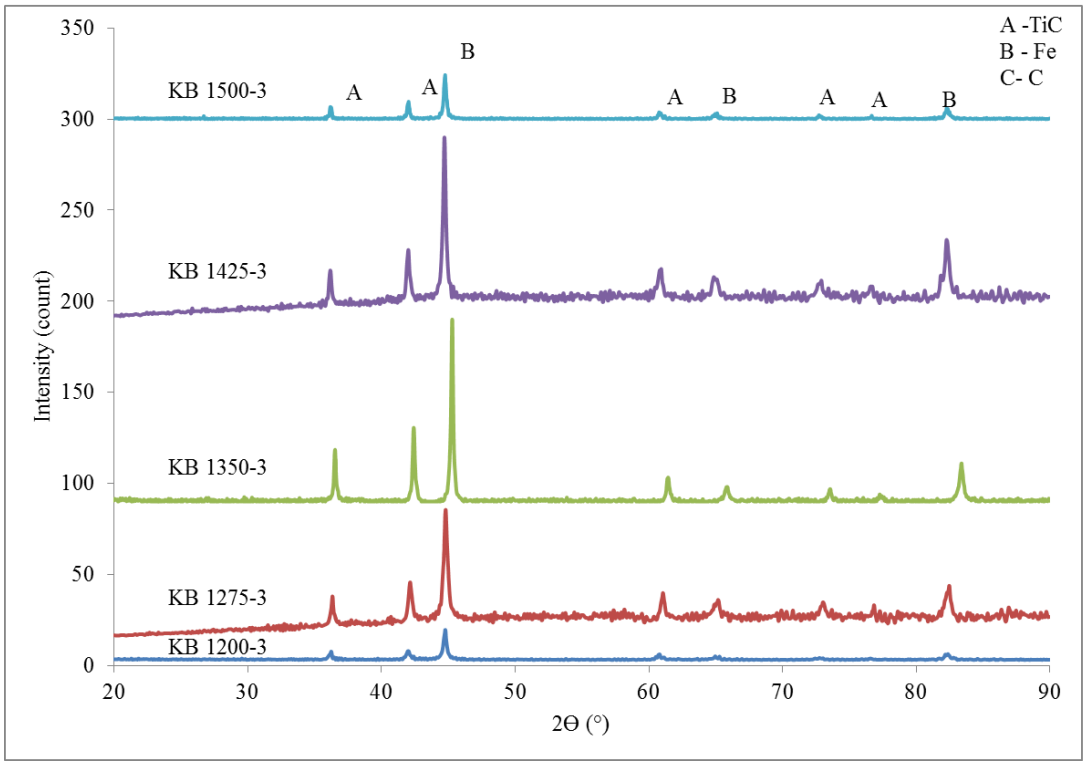


Figure 3.12. XRD patterns of the cermets containing 30 wt.% TiC.

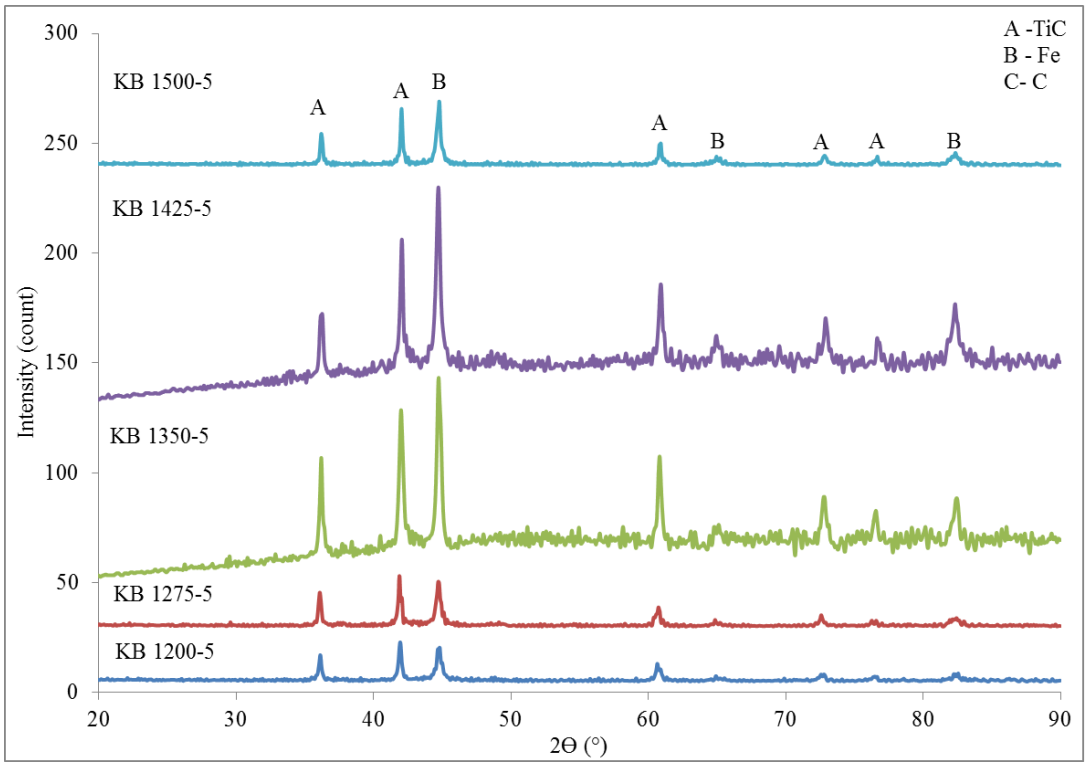


Figure 3.13. XRD patterns of the cermets containing 50 wt.% TiC.

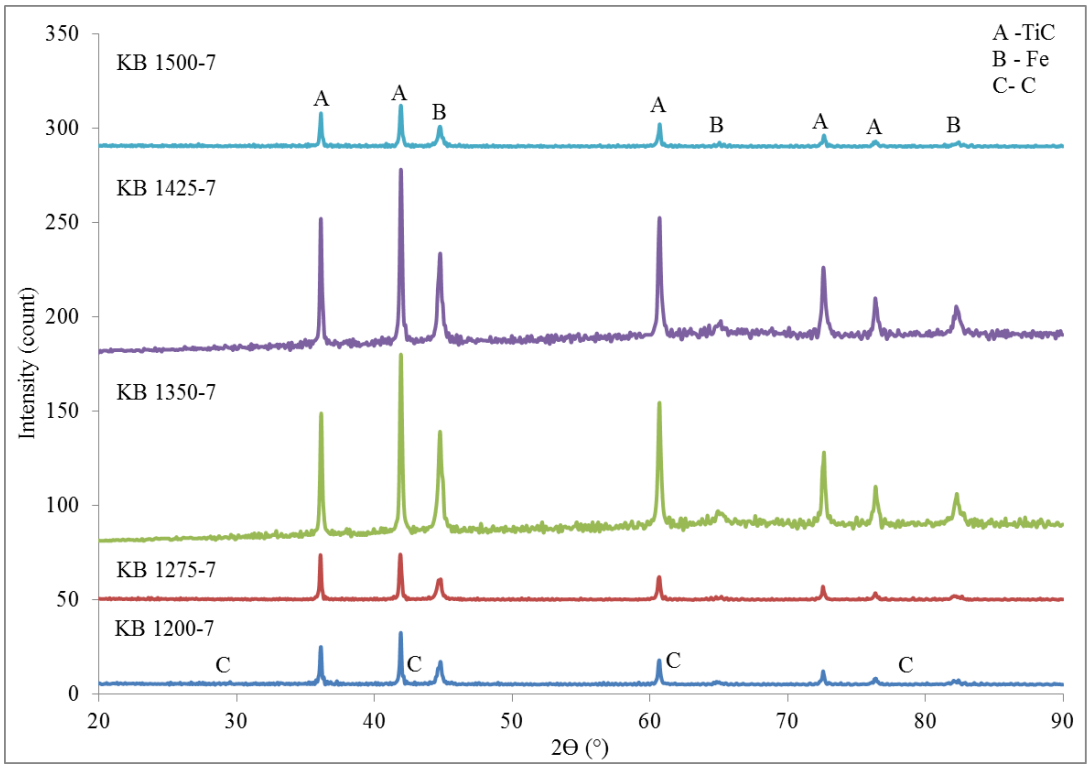


Figure 3.14. XRD patterns of the cermets containing 70 wt.% TiC.

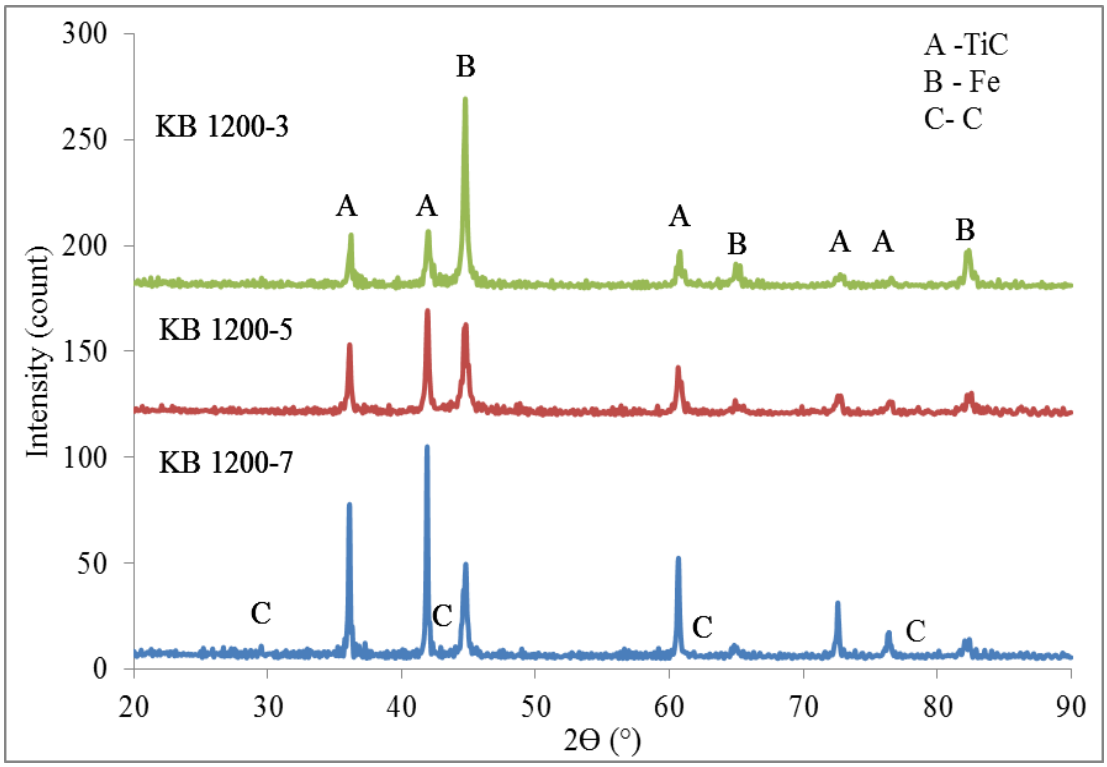


Figure 3.15. XRD patterns of cermets sintered at 1200 ºC.

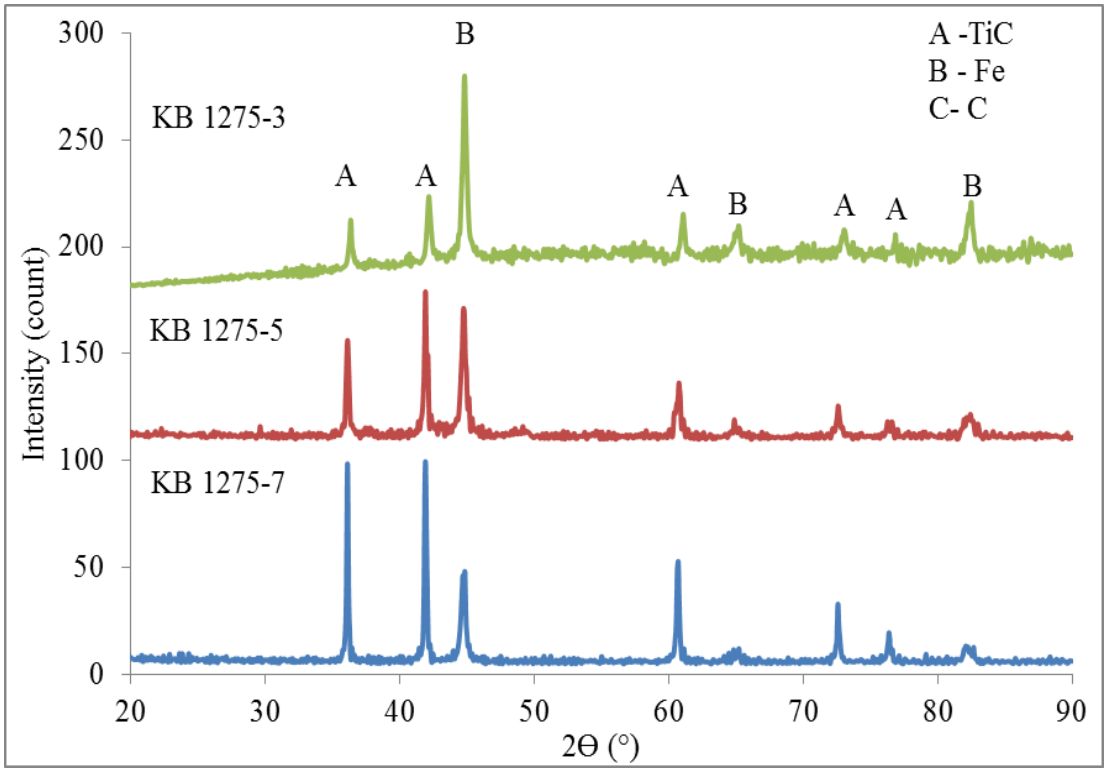


Figure 3.16. XRD patterns of the cermets sintered at 1275 ºC.

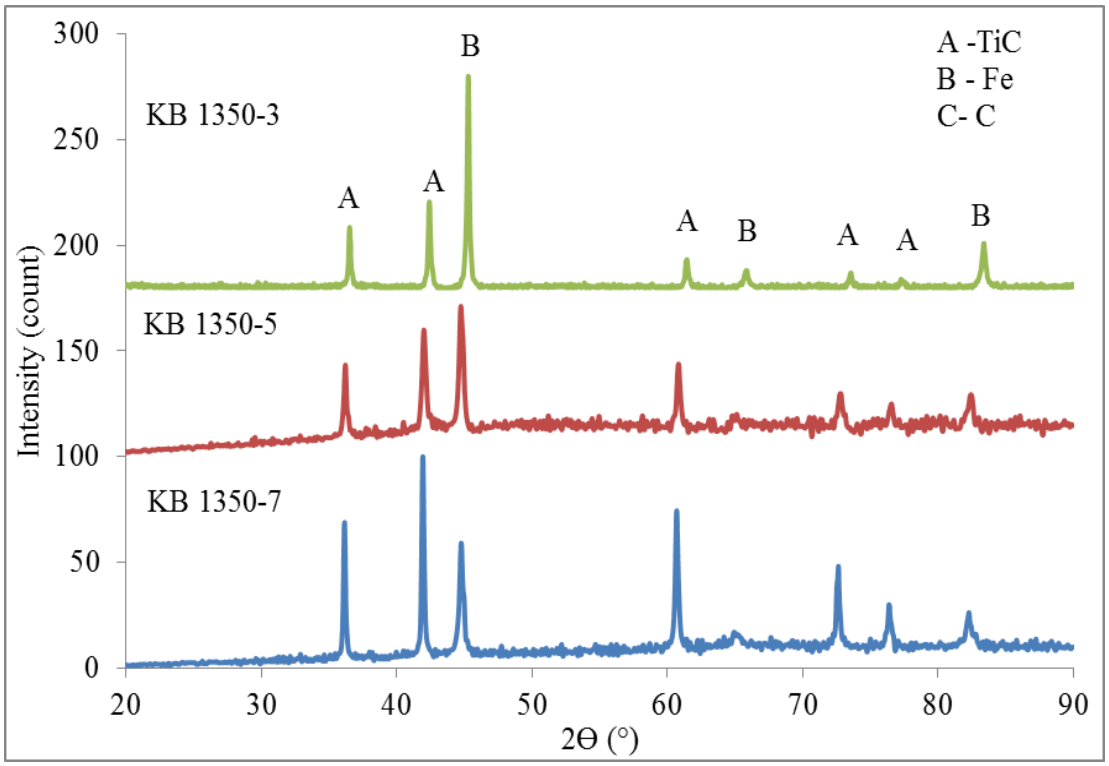


Figure 3.17. XRD patterns of the cermets sintered at 1350 ºC.

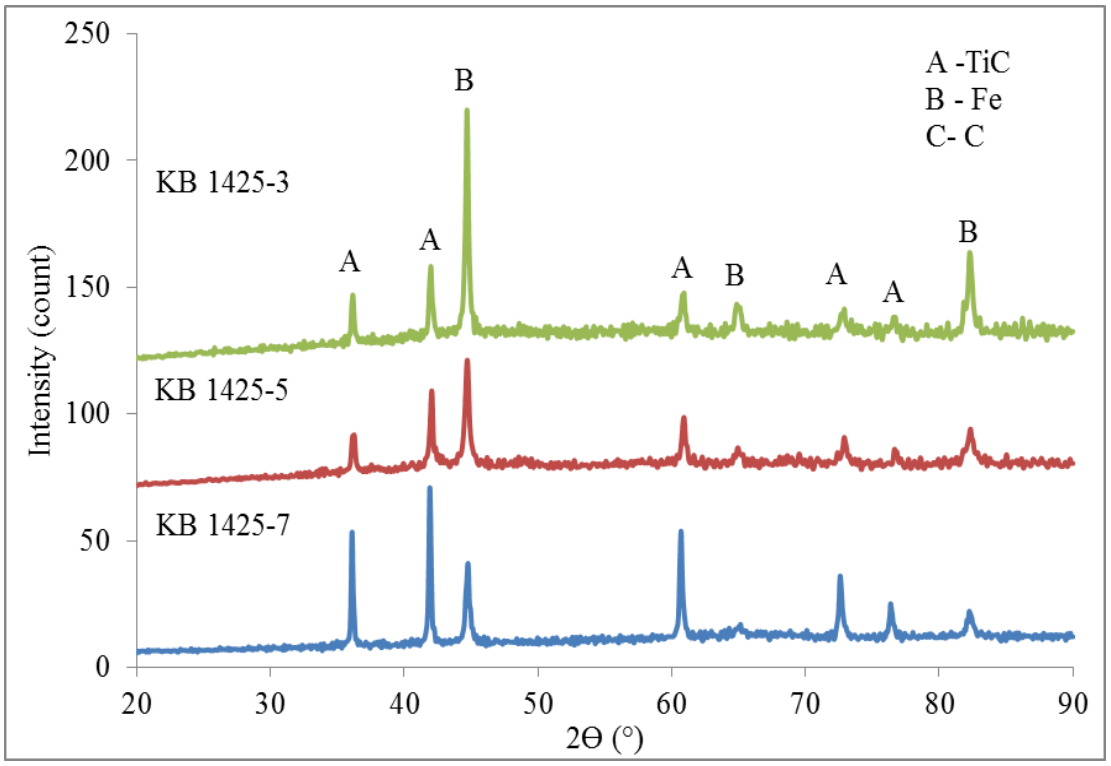


Figure 3.18. XRD patterns of the cermets sintered at 1425 ºC.

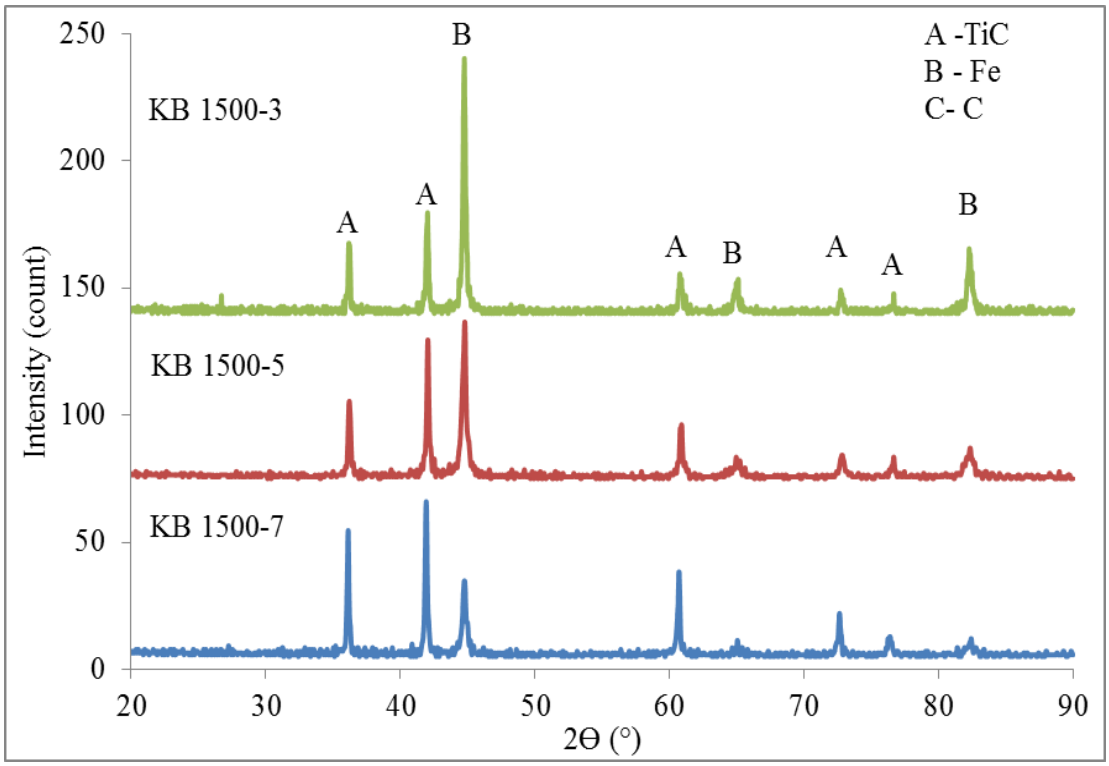


Figure 3.19. XRD patterns of the cermets sintered at 1500 ºC.

3.6. OM and SEM Analysis of Cermets

The following visual differences were detected on the surfaces and shapes of cermets after sintering. By considering the temperature rise parameter according to three (% 30, 50, 70 Ti+C) different chemical compositions, as shown in Fig 2.5.

- Cermets containing 30% TiC did not exhibit serious geometric changes due to the increasing sintering temperature. But from KB 1350-3, the color of the cermets became more metallic graying, and occurred collapses get deepen by increasing sintering temperature in the middle of the cermets were observed.

- When cermets containing 50% TiC were examined depending on the increasing sintering temperature, it was found that the color of the cermets after sintering started to become more metallic gray as from KB 1425-5. A little geometric distortion was observed only in the KB 1500-5 sample after sintering.

- When cermets containing 70% TiC are examined depending on the increasing sintering temperature, it is seen that increasing splits and cleavage occur in the cermets as from the lowest temperature and the temperature increase supports their growth.

These effects formed the dominant drop shape pattern on all cermet samples for this series. KB 1500-7 sample has a more metallic gray color than the others.

The images of the optical microscope and the micrographs of the scanning electron microscope obtained from sintered cermet samples are given in Fig. 3.20.-3.34. As a result of macro-dimensional examination even at 50X magnification, it was observed that there are three different coloreds (black-gray-white) areas in the cermet surfaces. These regions consisted of porosity and similar discontinuities due to the light not reflected from the black areas. The areas in gray shades, respectively, were specified as areas with dense TiC, while the relatively lighter area was determined as the areas rich in iron-based matrix metal. At the same time, the average particle size of the TiCs formed on the images obtained by SEM was calculated and average particle size values are shared in Table 3.3. Same color differences of phase structures were also observed in SEM micrographs obtained at magnifications between 500X and 5000X. In addition to the chemically different phase regions, as the magnification rates increased, findings supporting the following assumptions were found in the micrographs. SEM images of cermet samples were interpreted considering the effect of increasing temperature under 3 groups according to the chemical composition.

Formation of the matrix phase as islet and positioned the TiC phase like a granulated shell outside of the matrix islets were detected at the sample of the KB 1200-3 and the porosity ratio was observed high at TiC regions. Along with the temperature increase (KB 1275-3, KB 1350-3), the islet-shell structure was disrupted, and therefore the formation of TiC grains of different sizes with almost round were formed and these grains were surrounded homogeneously with the matrix phase. The homogeneous surrounding of the reinforcement particles with matrix was enable porosity to be reduced. At 1425 ^{o}C (KB 1425-3), the phase distribution of TiC and Fe was appeared to be completely homogeneous, and also with the effect of increasing temperature, the TiC particles tend to grow and coalesce. In the SEM images of the sample (KB 1500-3) with the highest sintering temperature of the series, it was observed that some TiC grains were coarsened and merged, matrix islands were formed. Conversely, the porous regions were come out in the matrix between TiC grains and even in the combined TiC clusters.

In the examination of the SEM micrographs of samples (KB-1200-5, KB 1275-5), it was obtained microstructure as formed TiC grains with the non-surrounded by Fe-based matrix on different sizes and forms. The presence of large porous areas and

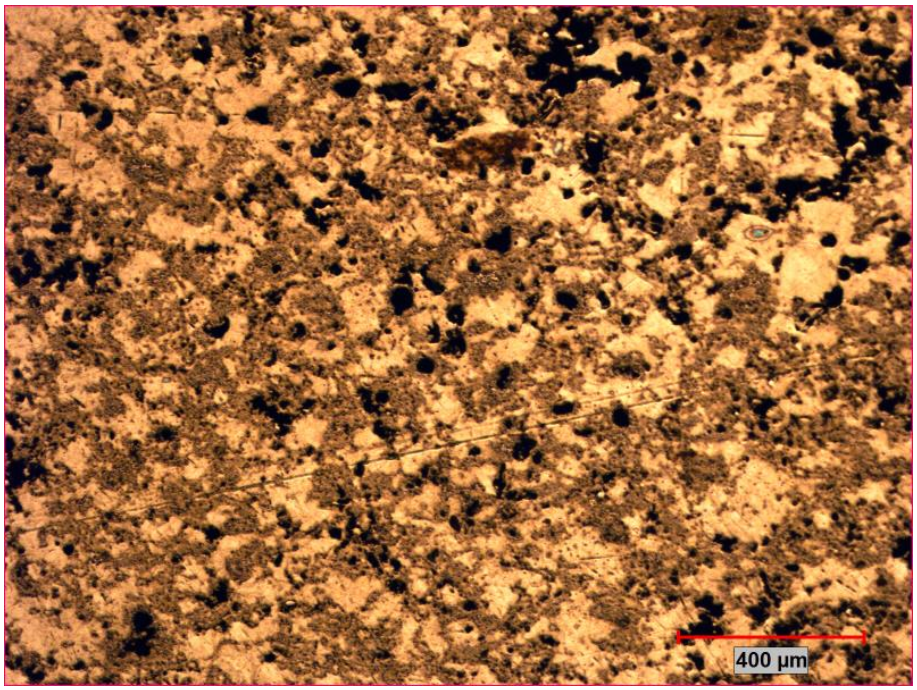
more, these findings are predicted to be due to insufficient sintering. In cermet samples of KB-1350-5, TiC grains were rounded and formed in more homogeneous dimensions, better encapsulation of these reinforcing phases by the matrix phase and a serious decrease in the porous areas were observed. It was determined at cermets sintered in the high temperatures (KB 1425-5 and KB 1500-5), matrix-poor regions were formed between homogeneously distributed TiC grains in some parts of the microstructure and these regions were in the porous structure.

In the SEM micrographs of KB 1200-7 cermets, numerous porosity areas, TiC particles formed in different sizes and forms, and insufficient Fe matrix network were observed. In this series, due to the increasing temperature, the relatively homogenized TiC grains at KB 1275-7 are better surrounded by the matrix, the porosity in the boundary of the reinforcement and the matrix has decreased, and but the gaps in the structure have grown even. In the SEM micrographs of KB 1350-7 and KB 1425-7 samples, the decrease in the number and size of gap areas started and continued with the effect of temperature increase, and at the same time, a tendency to coalesce was observed in grains of TiC. As the sintering temperature continued to increase (KB 1425-7 and KB 1500-7), sharp decreases in large gaps-porous areas were seen, as well as the coarsening and coalescing on TiC grains were caused to the formation of TiC clusters. The aggregation tendency resulted in the formation of small porous regions between TiC grains. Which are thought to be due to the matrix phase surrounding the TiC grains inadequate in the face of coarsening and coalescence.

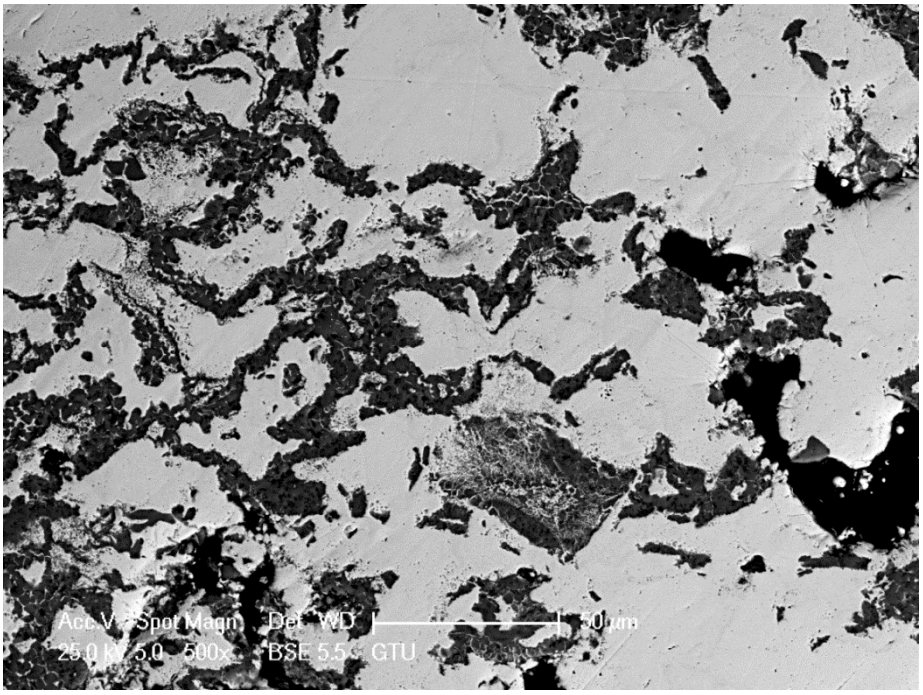
As shown in the study by Li et al., In the Ti-C-Fe system, the two types of TiC grains (coarse/angular and fine/round) are formed according to the sintering temperature and the ratio of (Ti+C)/Fe. Li's study indicated that the course/angular TiC grains (~2 μ) by the nucleation-growth mechanism and the smaller/rounder grains by the solution and precipitation mechanism are formed. It showed that increasing sintering temperature and the ratio of T+C [exp., (28TiFe)-C, (48TiFe)-C, and (68TiFe)-C] can cause ten times enlargement in small grains [3]. Indeed, the coarse and angular TiC grains observed in all KB 1200-3-5-7 samples were formed due to the low sintering temperature. The average TiC particle size in samples with 30 wt% Ti + C composition was observed coarsening only depending on the sintering temperature. Due to the increasing sintering temperature and the increasing ratio of Ti+C/Fe of cermets containing 50 wt% and 70 wt% Ti+C, it was observed that the average TiC particle sizes increased. It is also seen in the SEM micrographs that the grain size is

always in the direction of increase, and these values are also shared in Table 3.3. Based on these factors, doing more precise measurement methods and calculations on more TiC particles are required to optimize the average TiC size and also the rate of increase.

Especially in SEM micrographs of all KB 1425 and KB 1500 samples, increasing temperature cause the formation of matrix-poor regions amoung TiCs trying to coarsen and merge. Lee et al. reported in their study that micro-porosities formed and increased in the composite structure in direct proportion to the increasing temperature and Ti+C/Fe ratio for (28TiFe)-C, (48TiFe)-C, and (68TiFe)-C systems. Additionally, it was emphasized that micro-porosities do not harm mechanical properties in their study [3]. This situation is thought to be related to the surface kinetic reactions exhibited between the high temperature TiC and the Fe matrix.

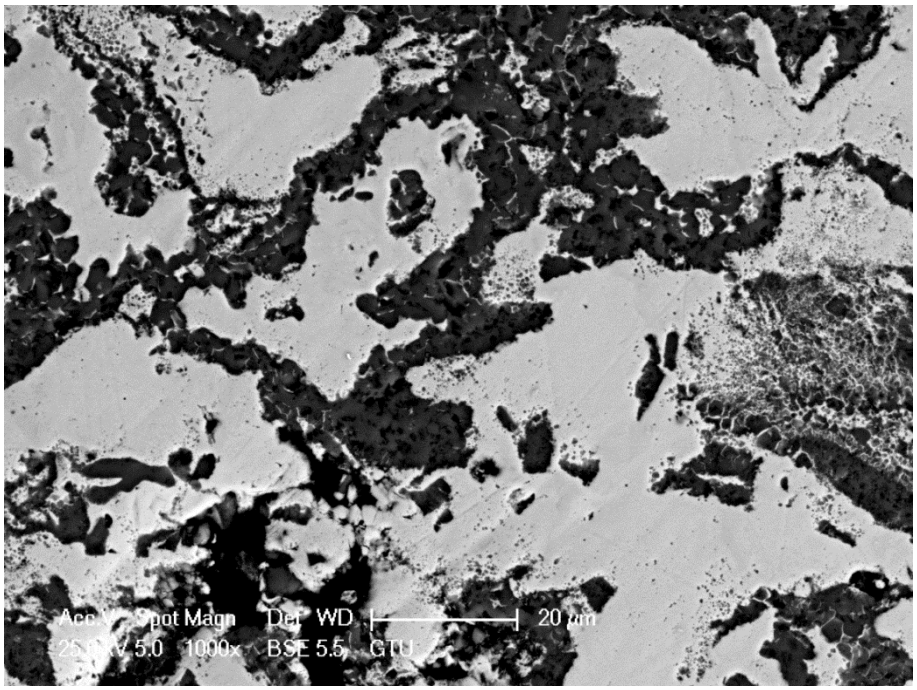


(a)

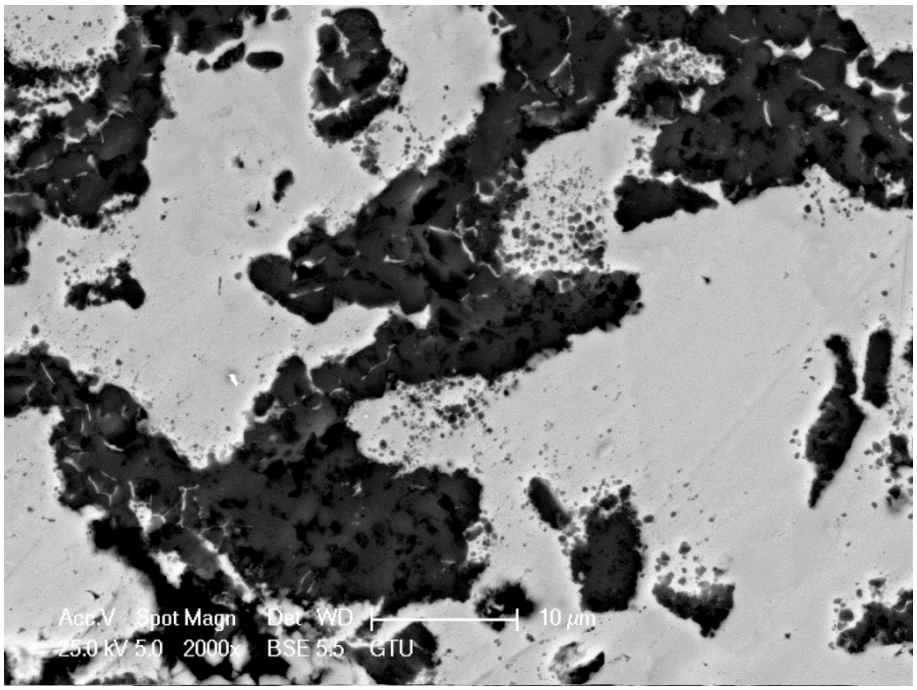


(b)

Figure 3.20. Micrographs of KB 1200-3 at a) 50X b) 500X c) 1000X d) 2000X e) 5000X and f) tipical particle sizes of TiCs at 5000X.

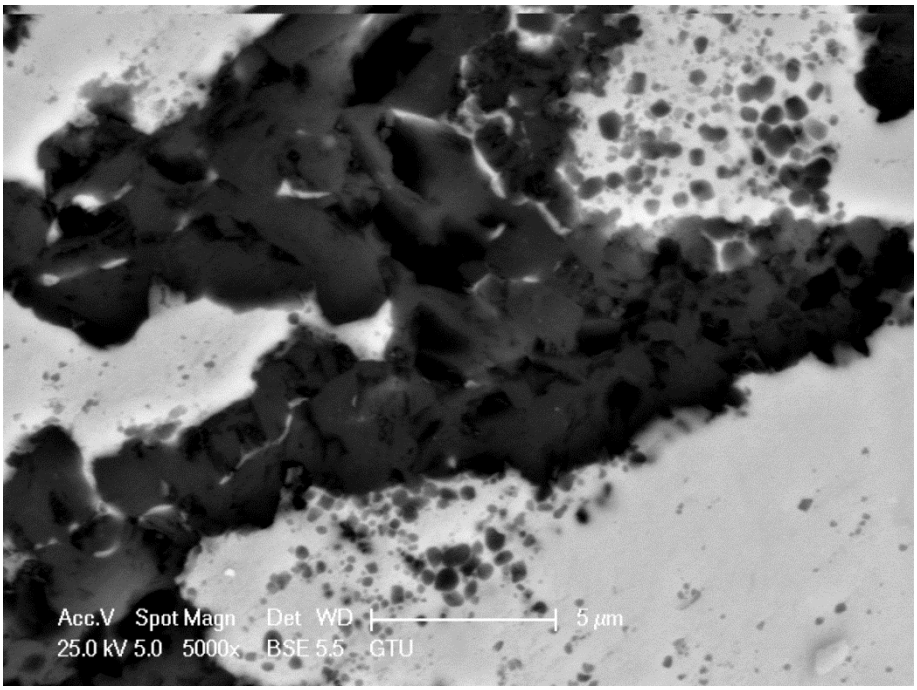


(c)

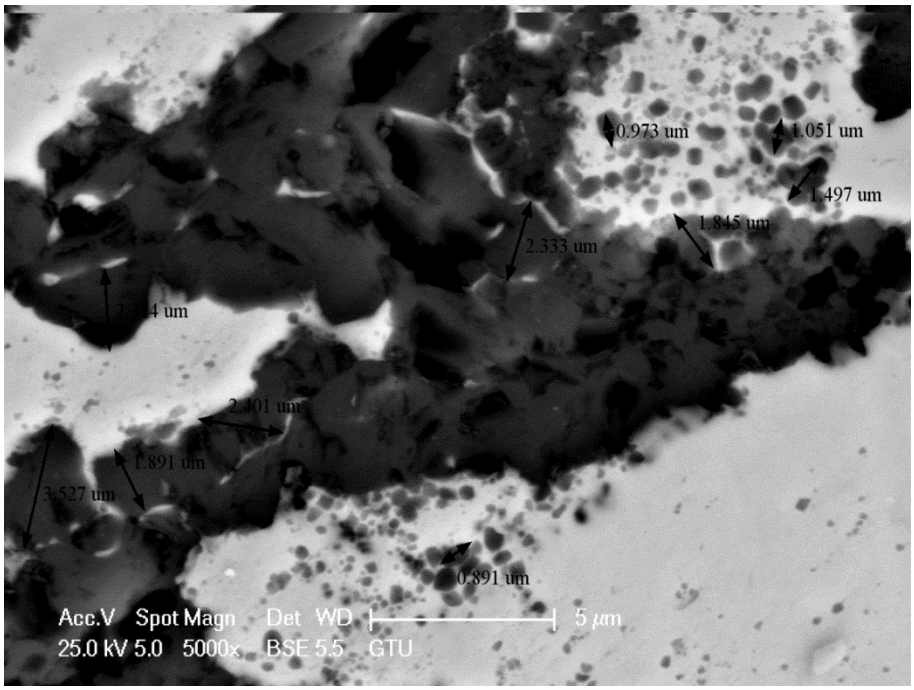


(d)

Figure 3.20. Micrographs of KB 1200-3 at a) 50X b) 500X c) 1000X d) 2000X e) 5000X and f) tipical particle sizes of TiCs at 5000X (continuum).

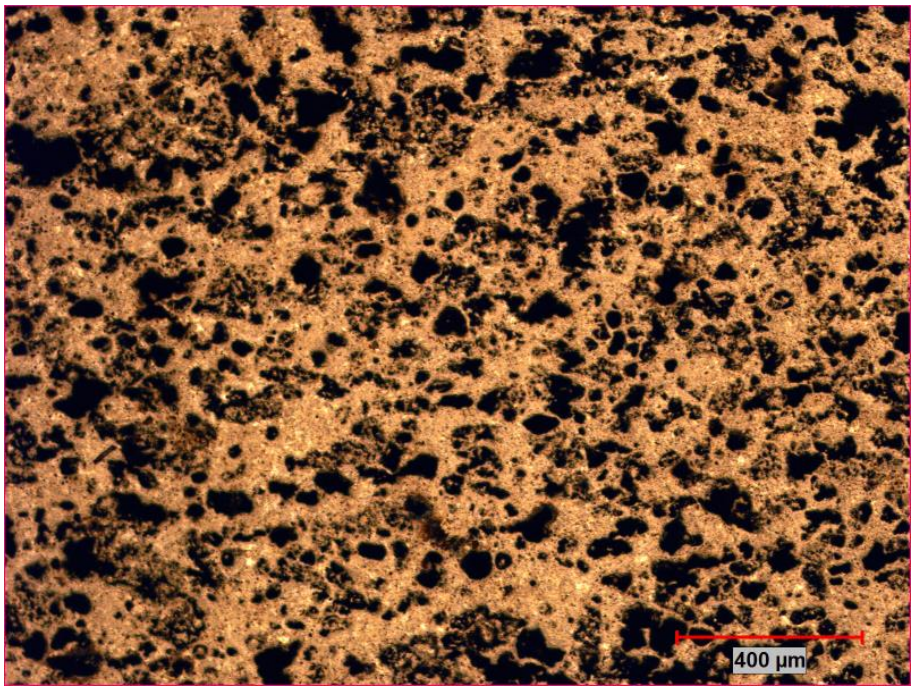


(e)

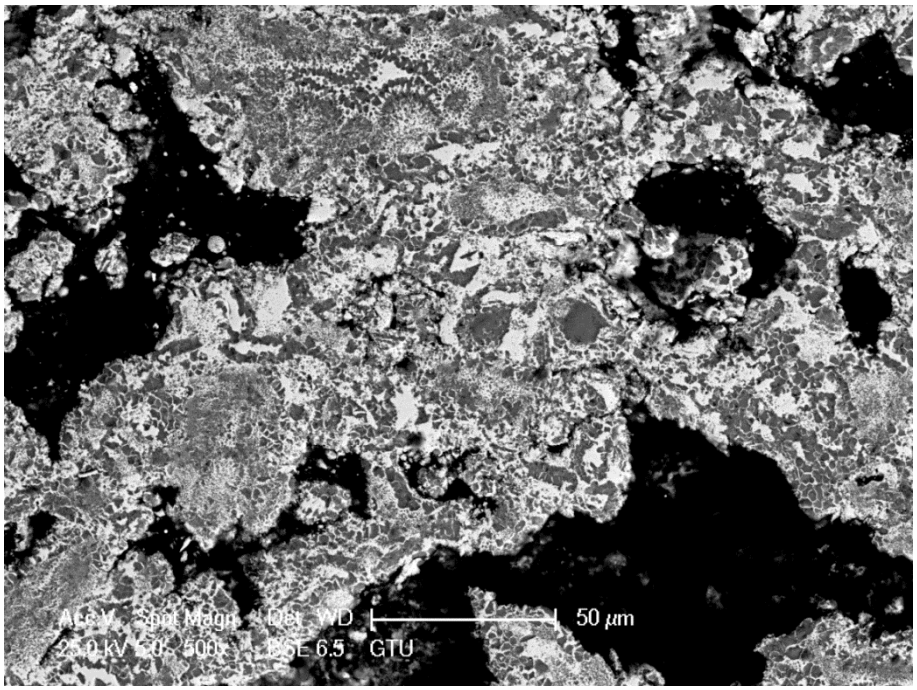


(f)

Figure 3.20. Micrographs of KB 1200-3 at a) 50X b) 500X c) 1000X d) 2000X e) 5000X and f) tipical particle sizes of TiCs at 5000X (continuum).

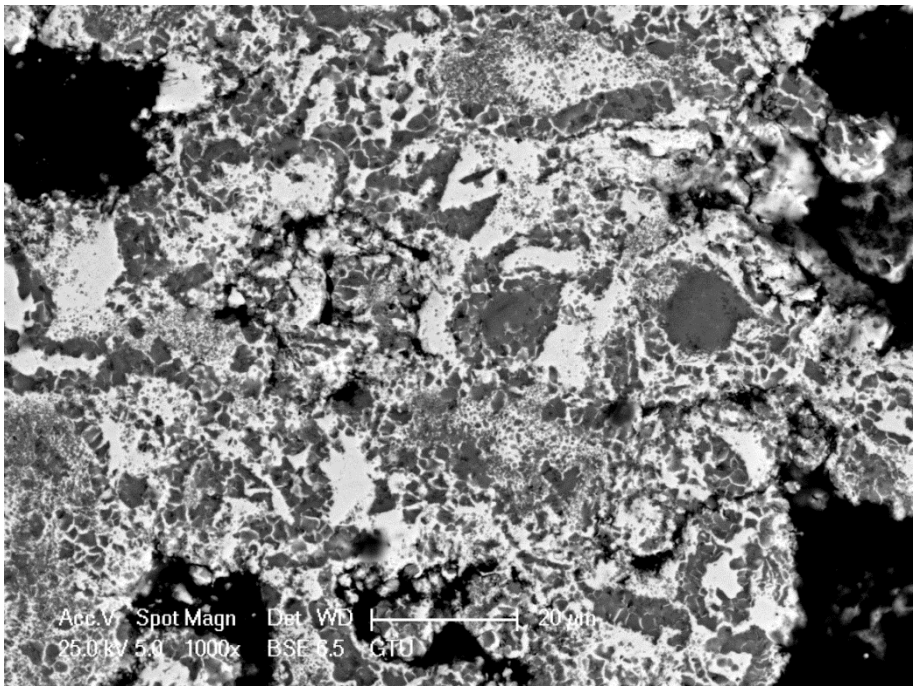


(a)

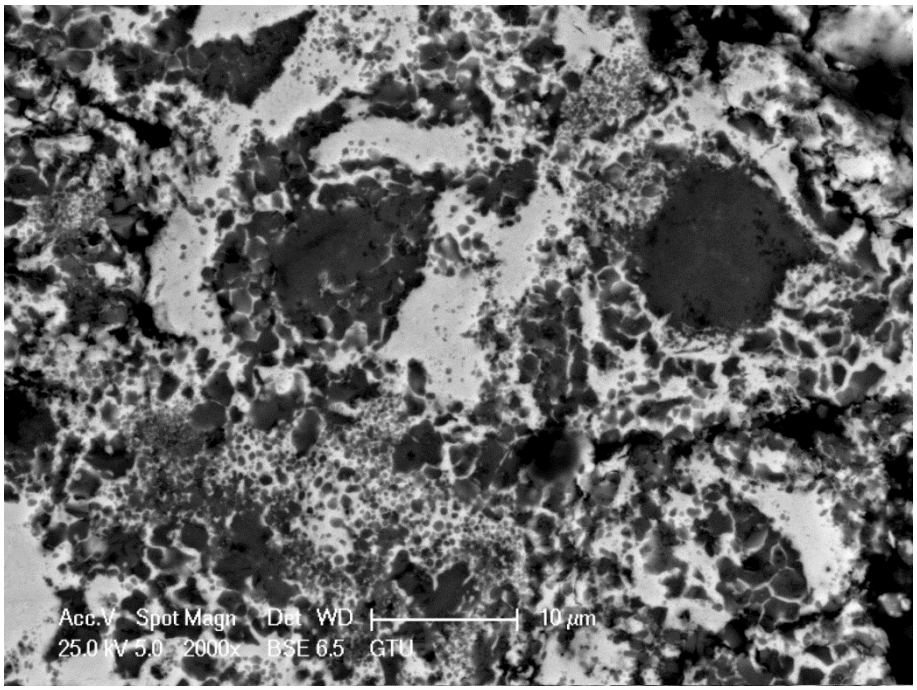


(b)

Figure 3.21. Micrographs of KB 1200-5 at a) 50X b) 500X c) 1000X d) 2000X e) 5000X and f) tipical particle sizes of TiCs at 5000X.

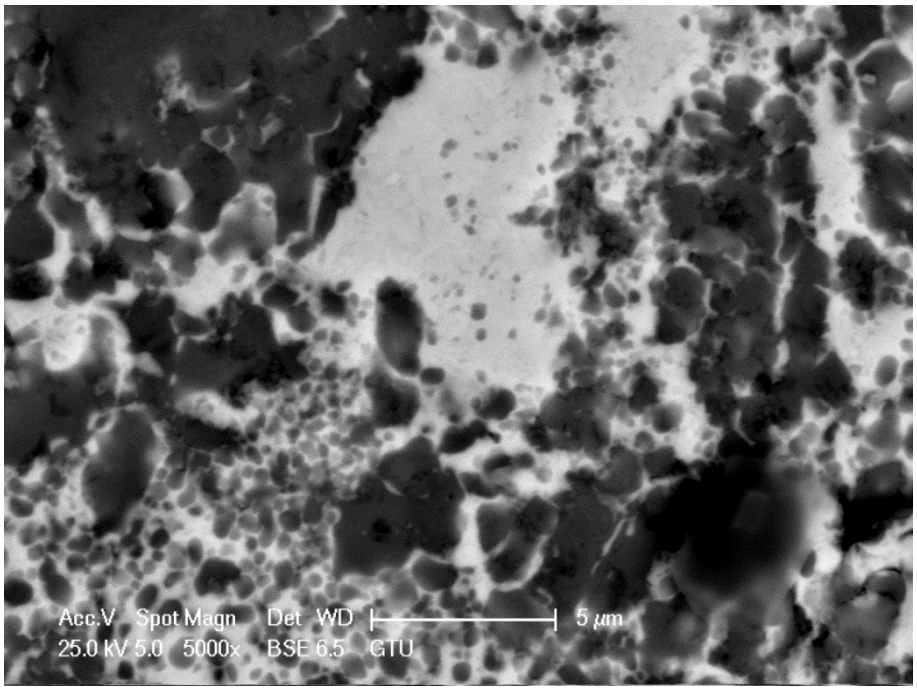


(c)

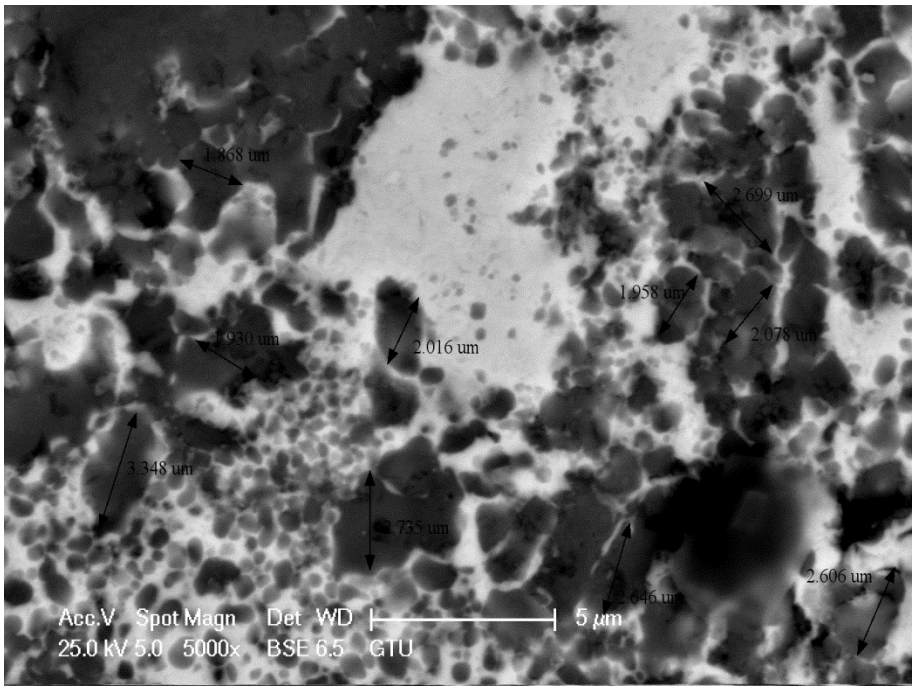


(d)

Figure 3.21. Micrographs of KB 1200-5 at a) 50X b) 500X c) 1000X d) 2000X e) 5000X and f) tipical particle sizes of TiCs at 5000X (continuum).

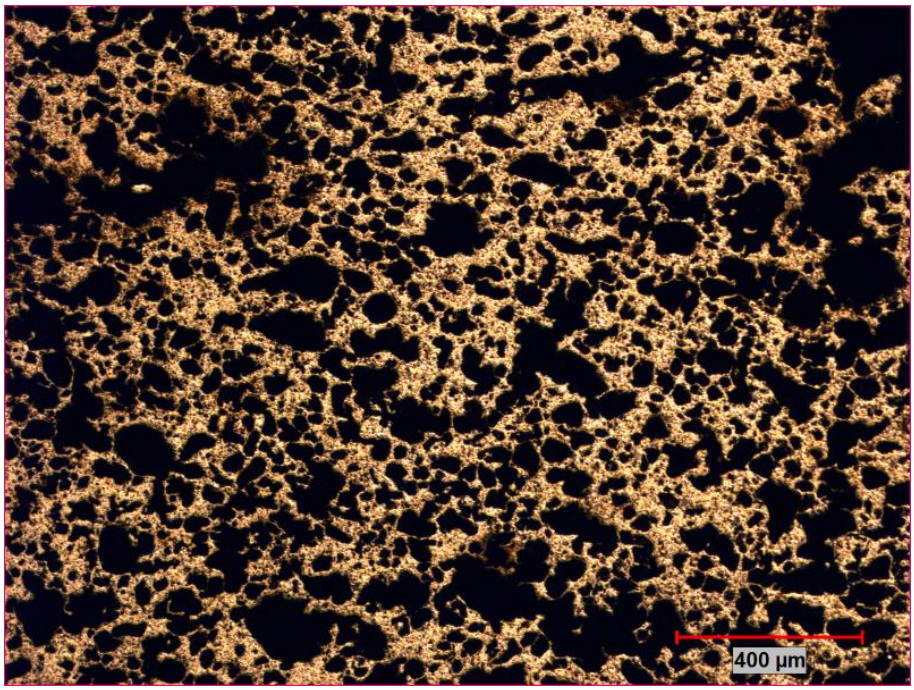


(e)

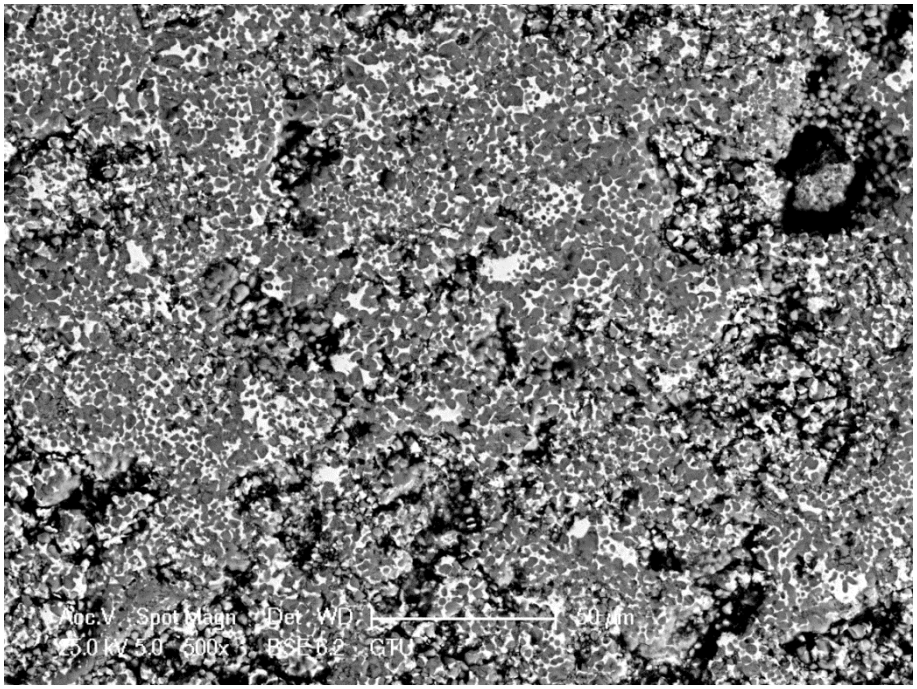


(f)

Figure 3.21. Micrographs of KB 1200-5 at a) 50X b) 500X c) 1000X d) 2000X e) 5000X and f) tipical particle sizes of TiCs at 5000X (continuum).

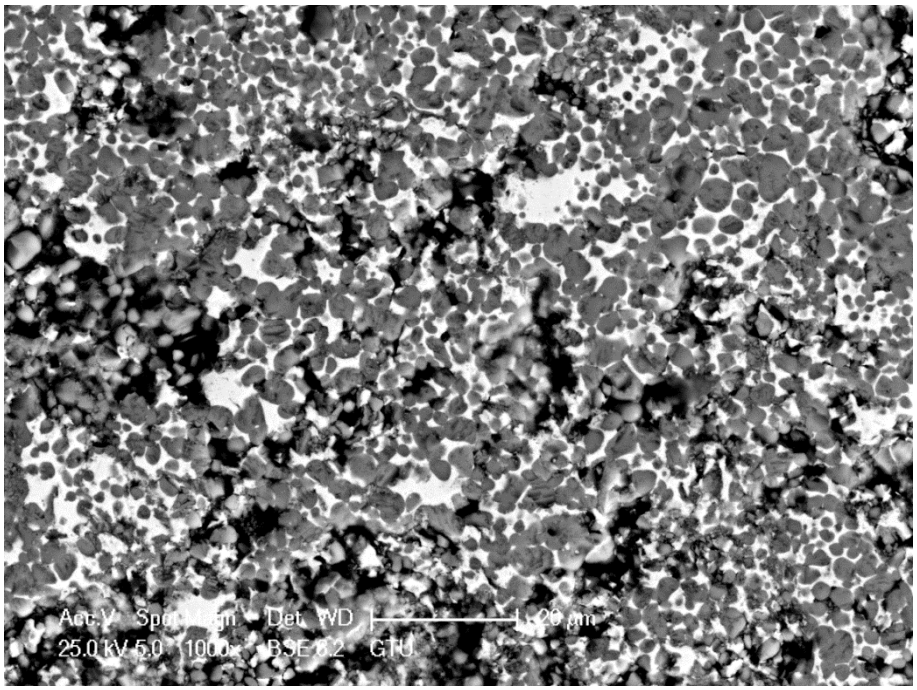


(a)

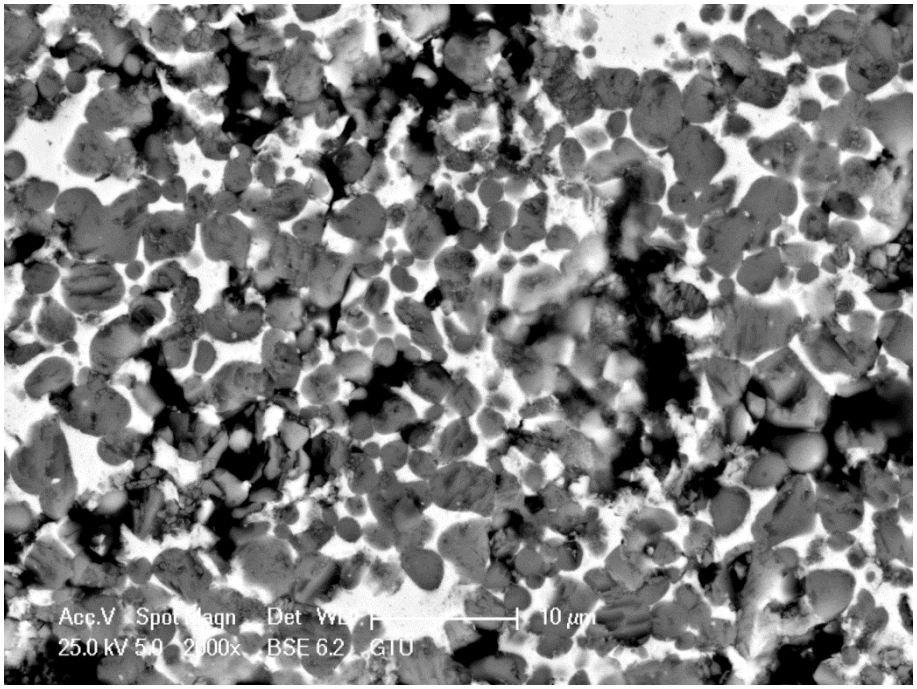


(b)

Figure 3.22. Micrographs of KB 1200-7 at a) 50X b) 500X c) 1000X d) 2000X e) 5000X and f) tipical particle sizes of TiCs at 5000X.

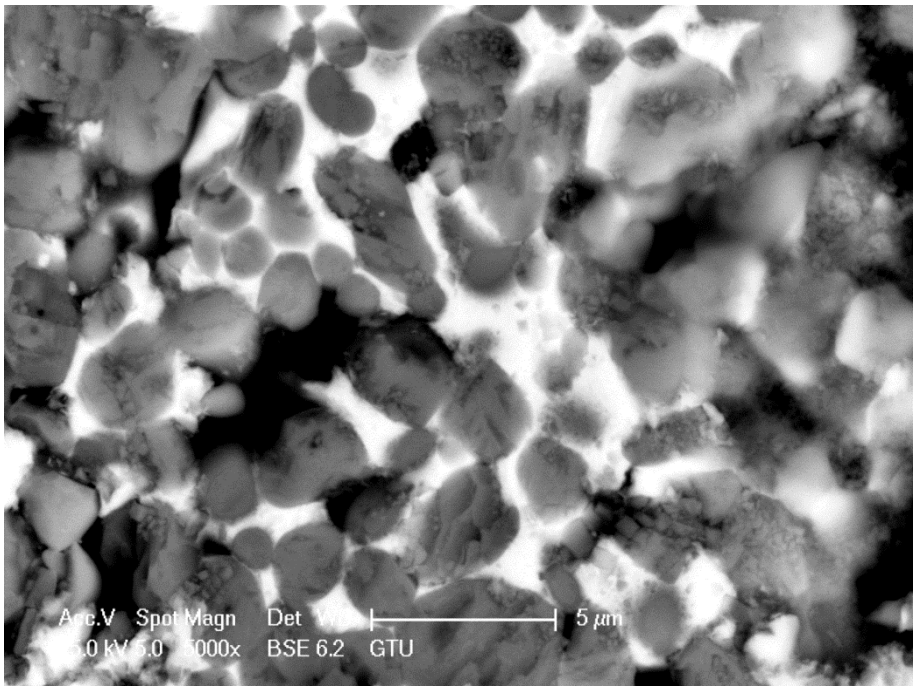


(c)

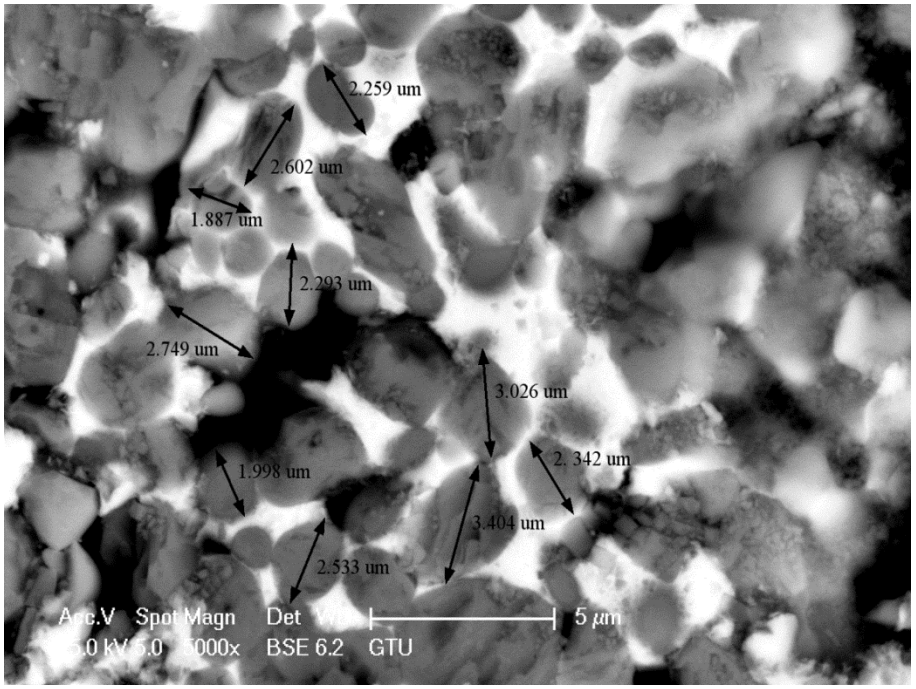


(d)

Figure 3.22. Micrographs of KB 1200-7 at a) 50X b) 500X c) 1000X d) 2000X e) 5000X and f) tipical particle sizes of TiCs at 5000X (continuum).

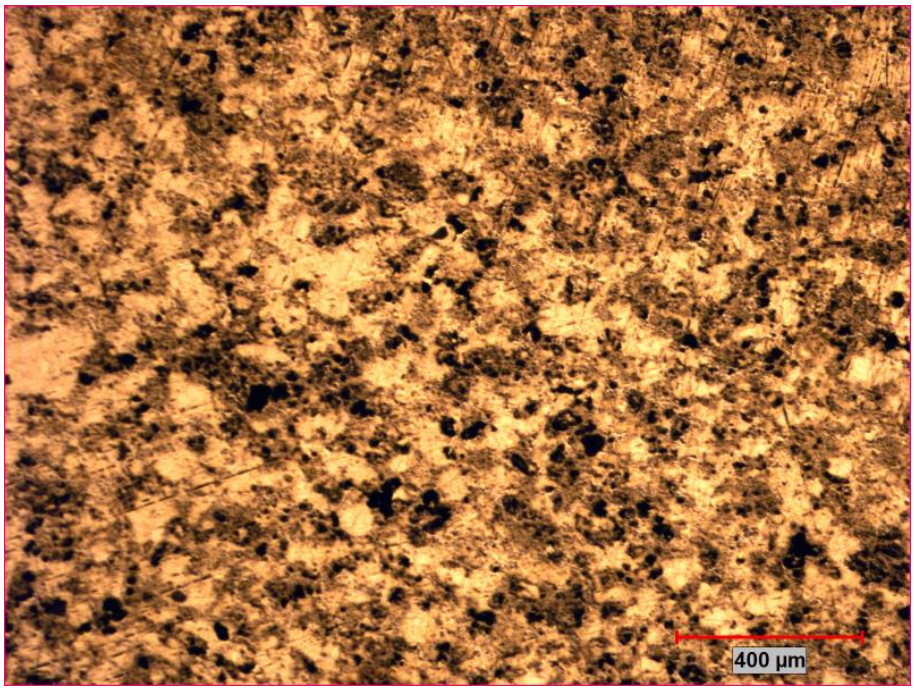


(e)

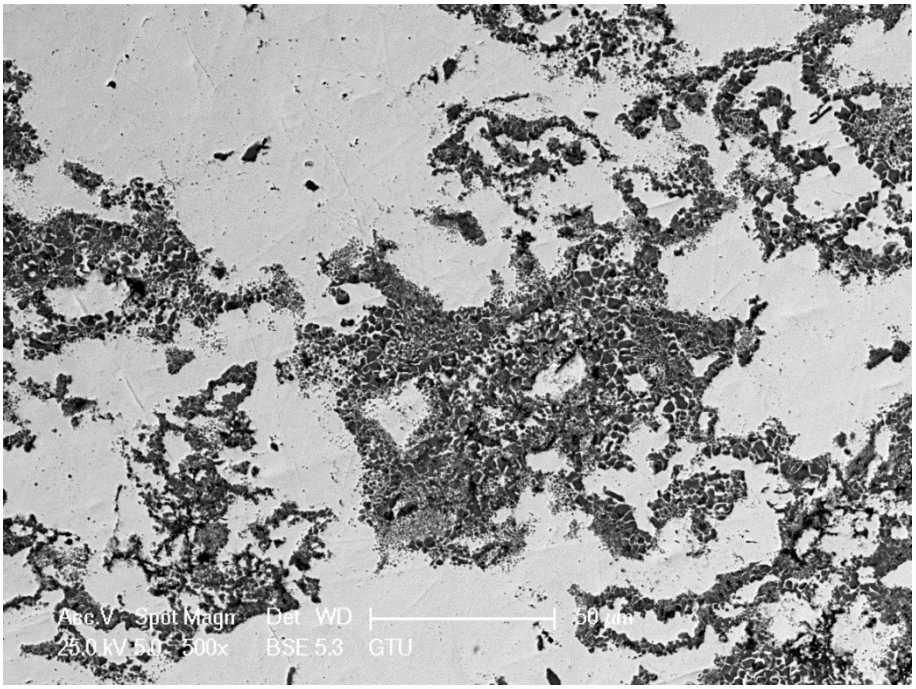


(f)

Figure 3.22. Micrographs of KB 1200-7 at a) 50X b) 500X c) 1000X d) 2000X e) 5000X and f) tipical particle sizes of TiCs at 5000X (continuum).

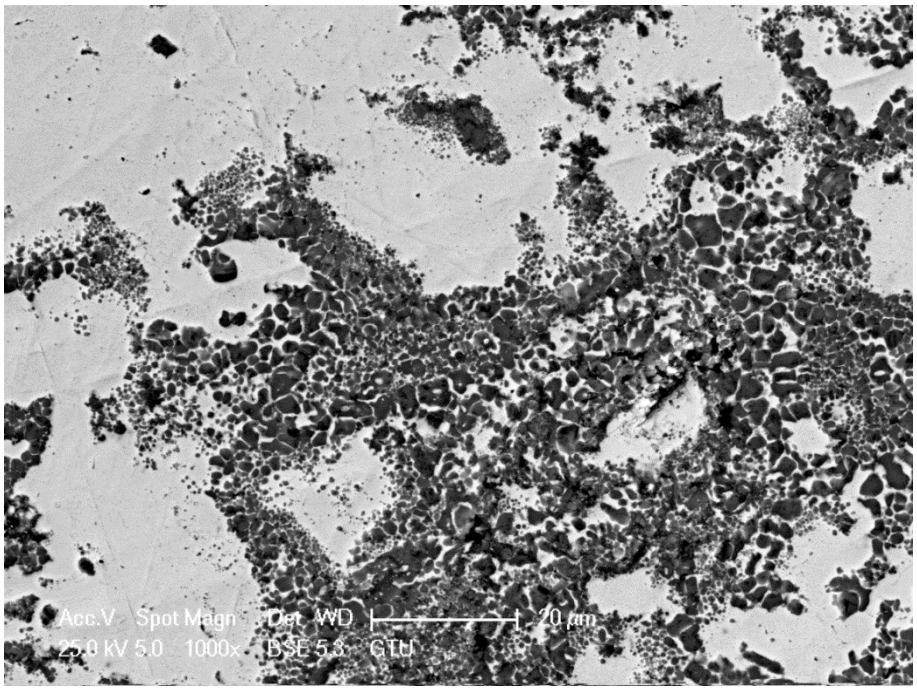


(a)

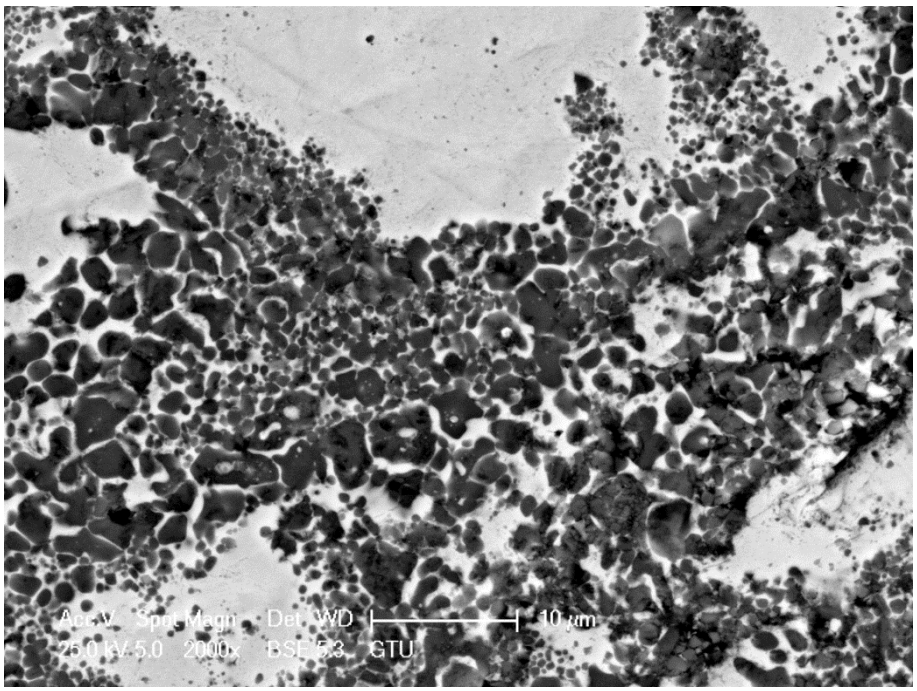


(b)

Figure 3.23. Micrographs of KB 1275-3 at a) 50X b) 500X c) 1000X d) 2000X e) 5000X and f) tipical particle sizes of TiCs at 5000X.

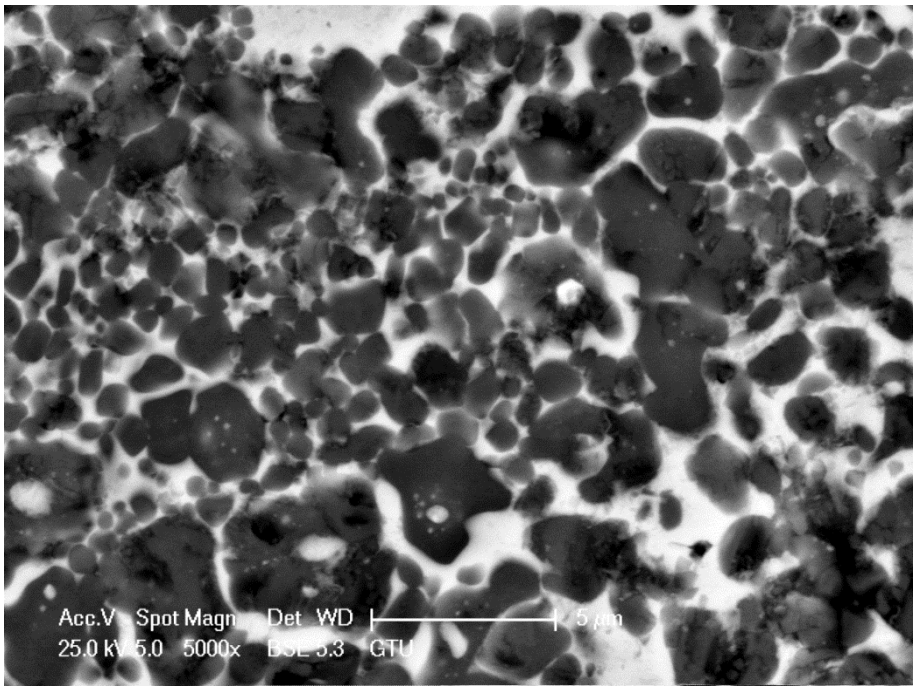


(c)

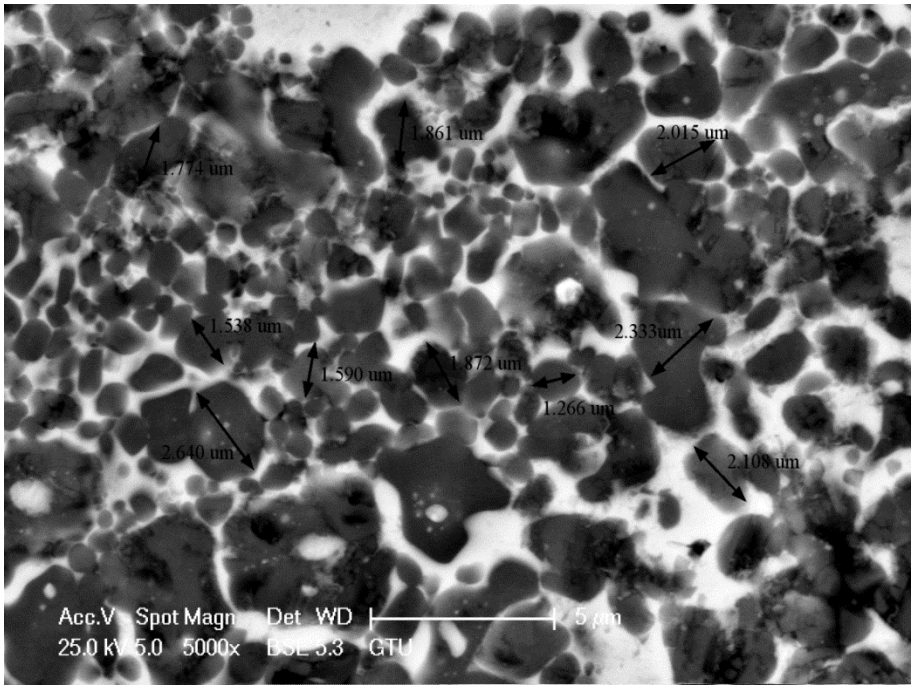


(d)

Figure 3.23. Micrographs of KB 1275-3 at a) 50X b) 500X c) 1000X d) 2000X e) 5000X and f) tipical particle sizes of TiCs at 5000X ((continuum).

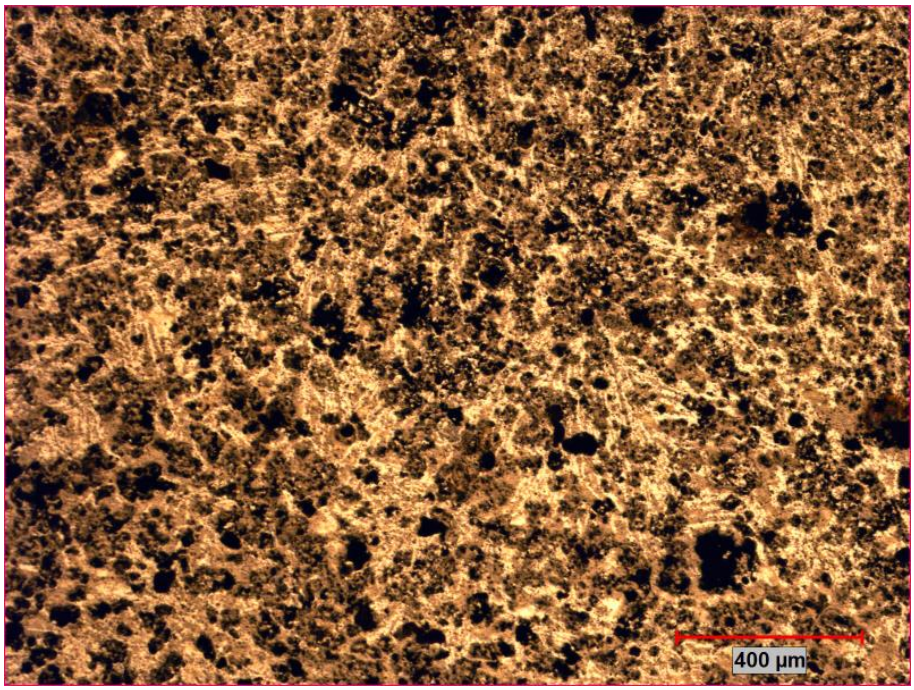


(e)

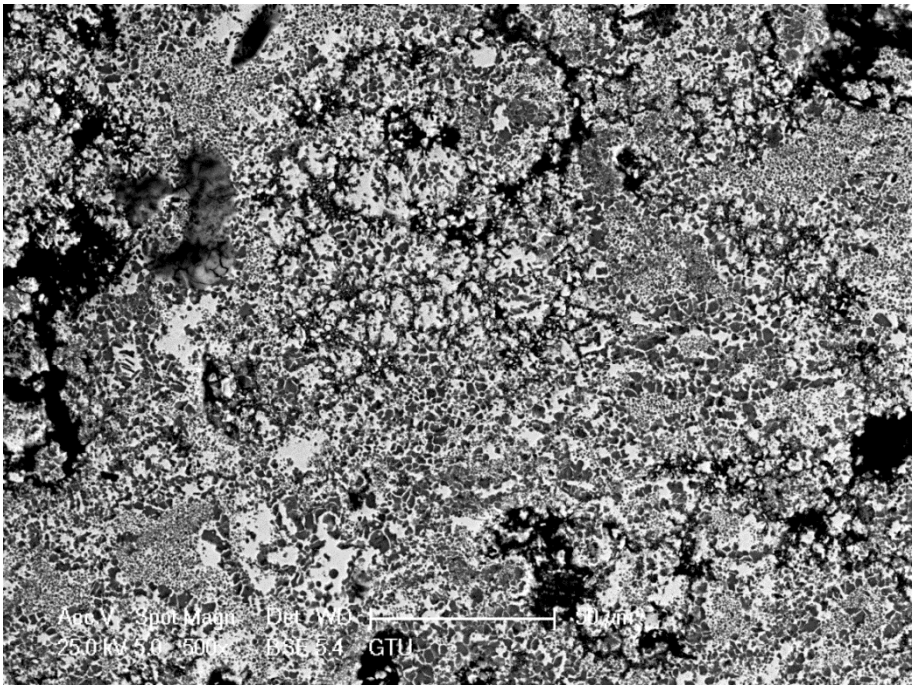


(f)

Figure 3.23. Micrographs of KB 1275-3 at a) 50X b) 500X c) 1000X d) 2000X e) 5000X and f) tipical particle sizes of TiCs at 5000X ((continuum).

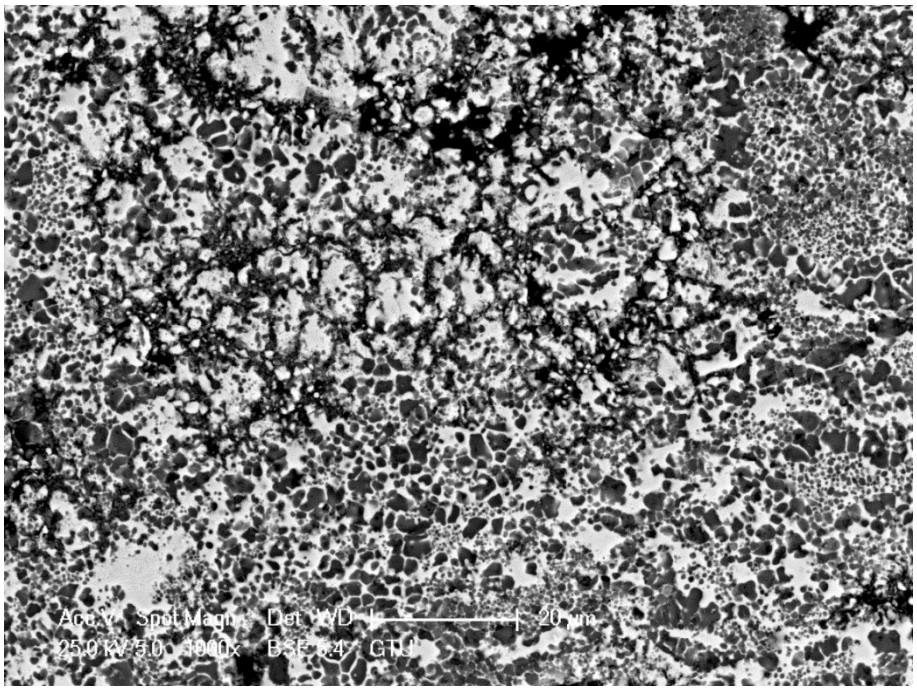


(a)

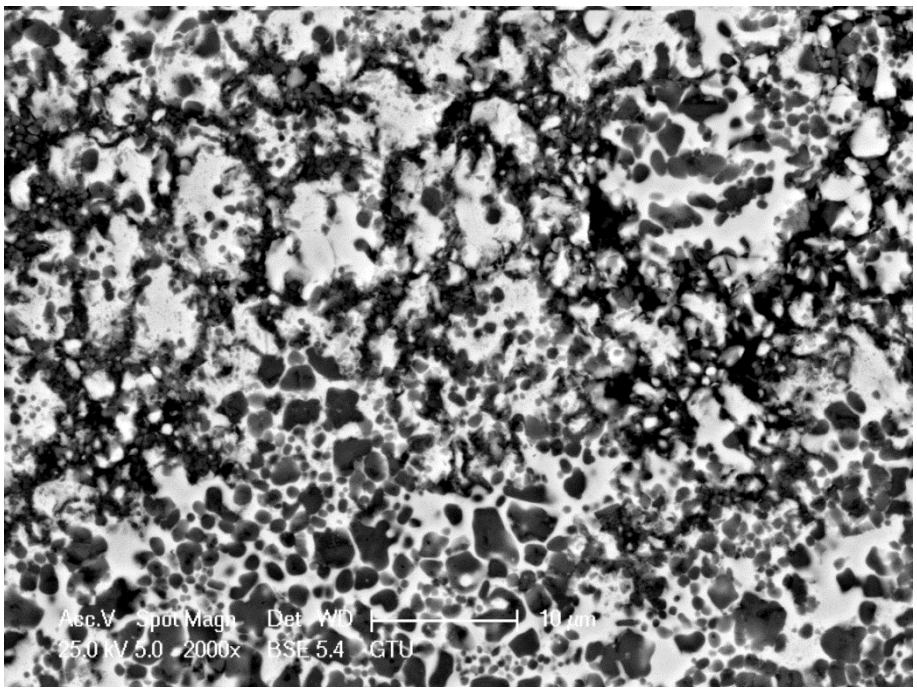


(b)

Figure 3.24. Micrographs of KB 1275-5 at a) 50X b) 500X c) 1000X d) 2000X e) 5000X and f) tipical particle sizes of TiCs at 5000X.

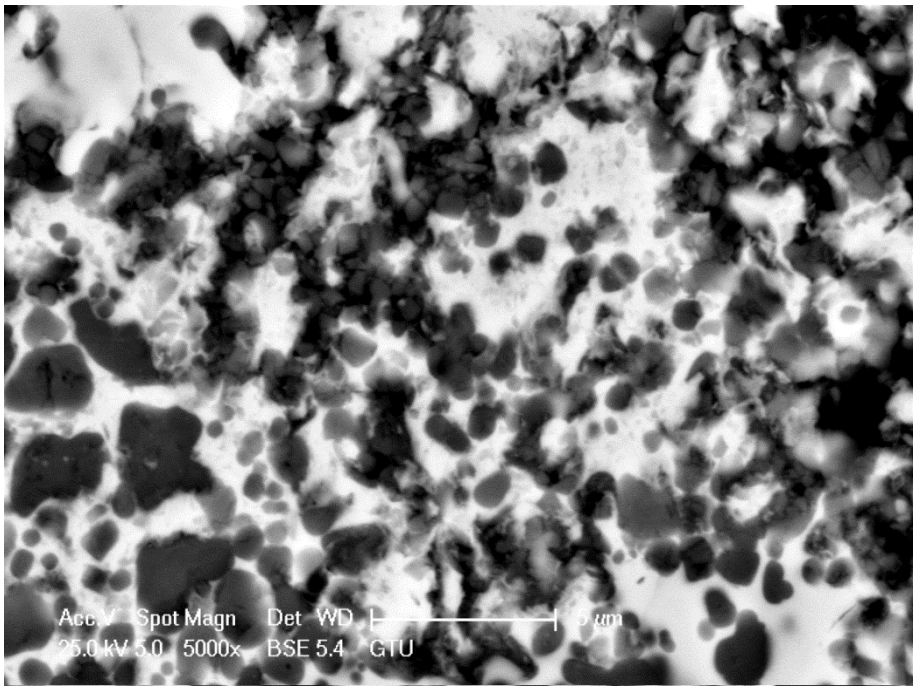


(c)

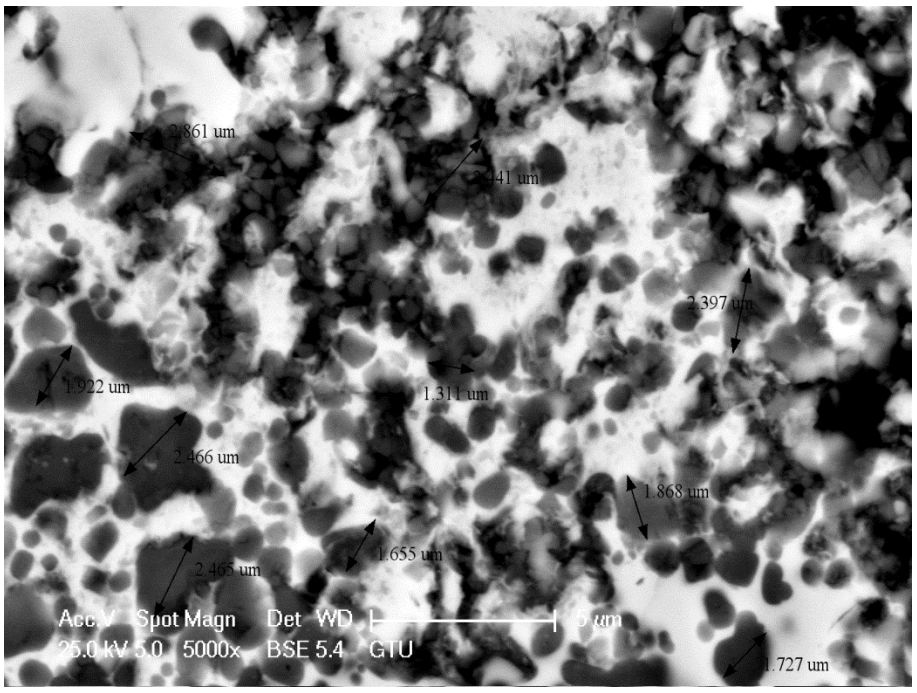


(d)

Figure 3.24. Micrographs of KB 1275-5 at a) 50X b) 500X c) 1000X d) 2000X e) 5000X and f) tipical particle sizes of TiCs at 5000X ((continuum).

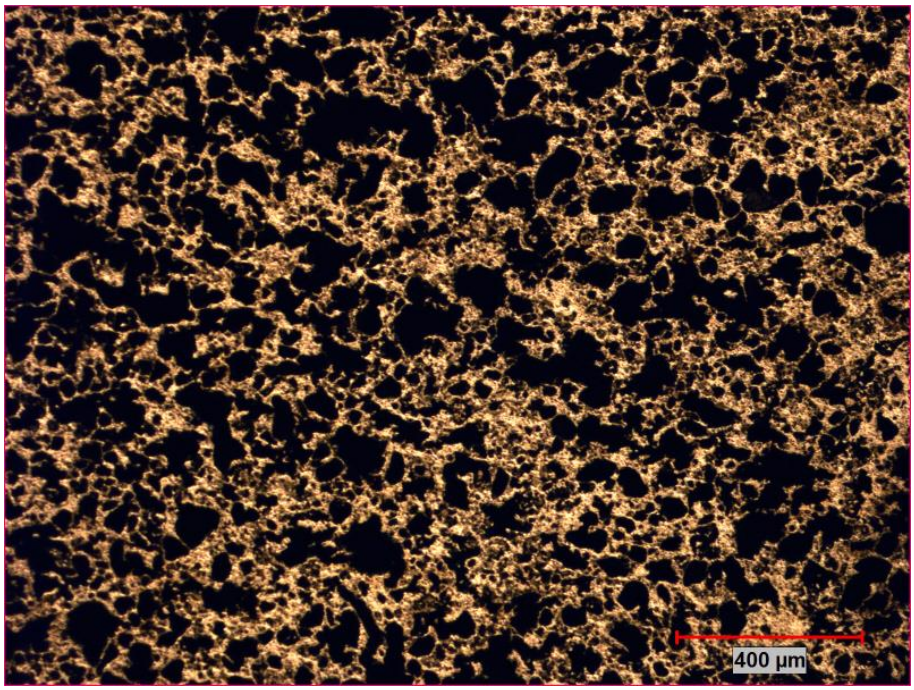


(e)

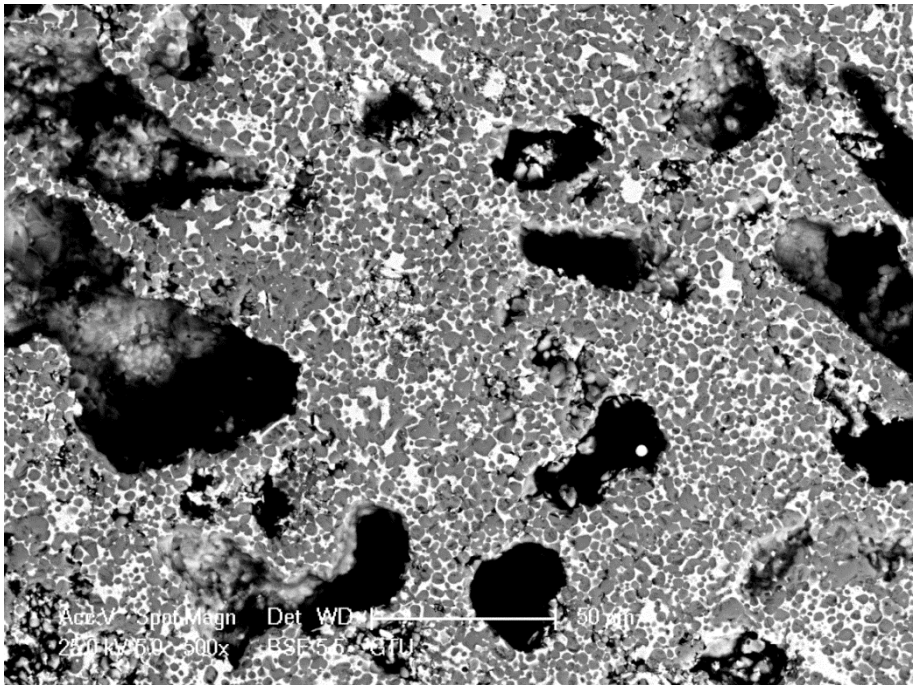


(f)

Figure 3.24. Micrographs of KB 1275-5 at a) 50X b) 500X c) 1000X d) 2000X e) 5000X and f) tipical particle sizes of TiCs at 5000X ((continuum).

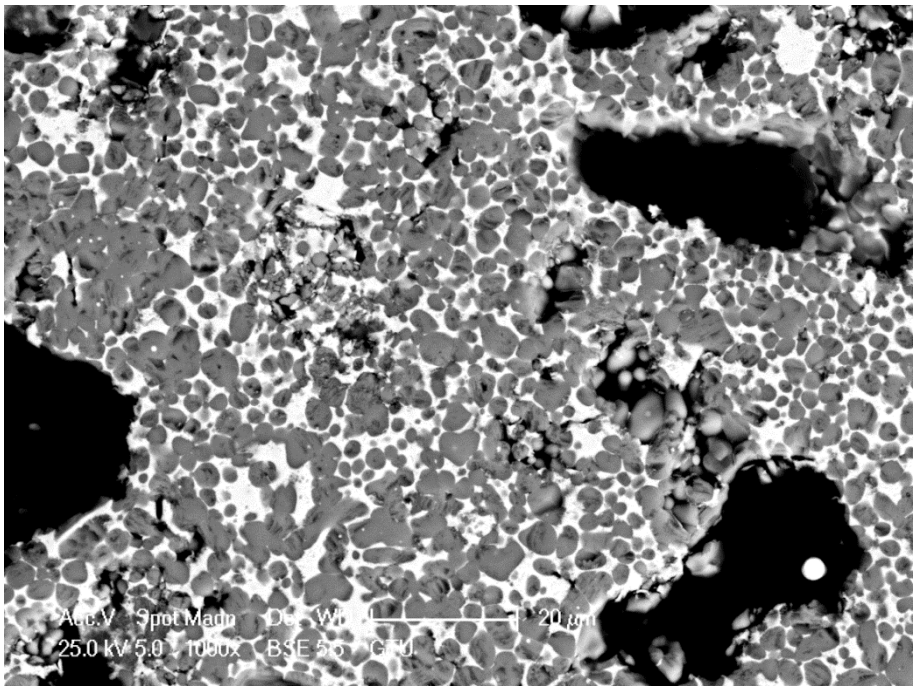


(a)

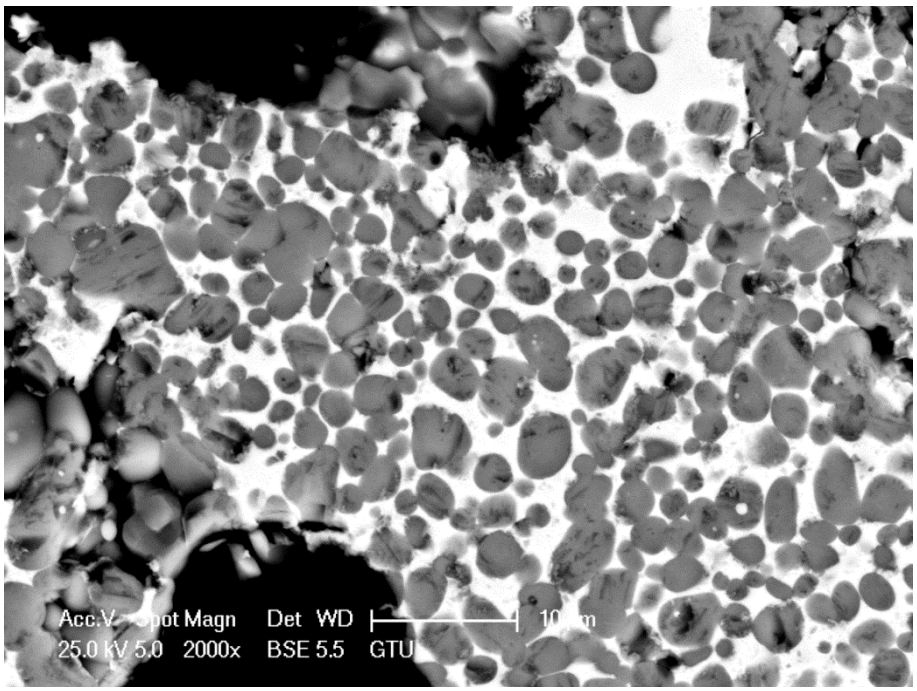


(b)

Figure 3.25. Micrographs of KB 1275-7 at a) 50X b)500X c) 1000X d) 2000X e) 5000X and f) tipical particle sizes of TiCs at 5000X.

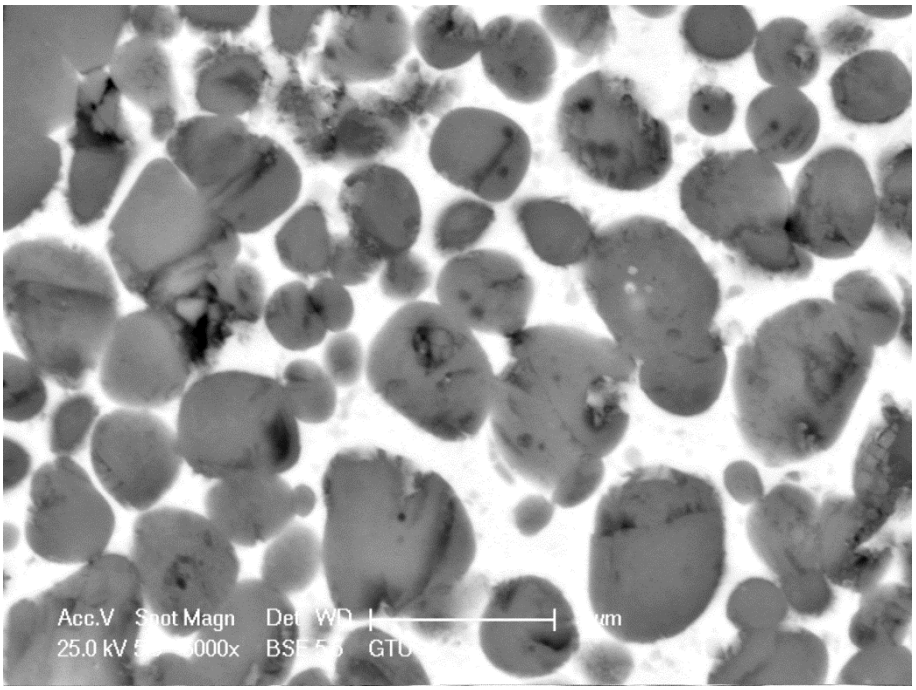


(c)

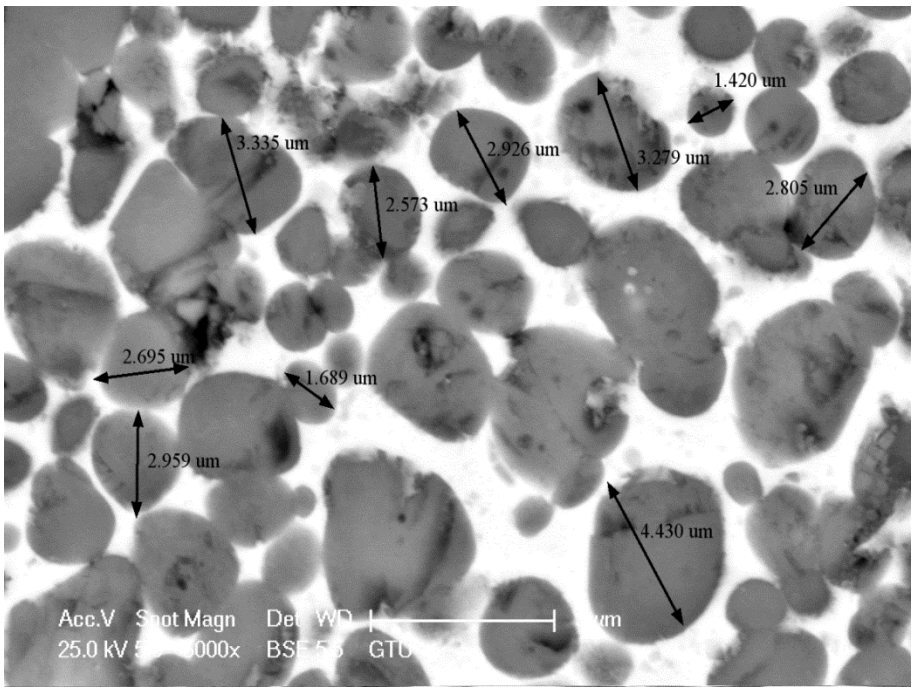


(d)

Figure 3.25. Micrographs of KB 1275-7 at a) 50X b)500X c) 1000X d) 2000X e) 5000X and f) tipical particle sizes of TiCs at 5000X ((continuum).

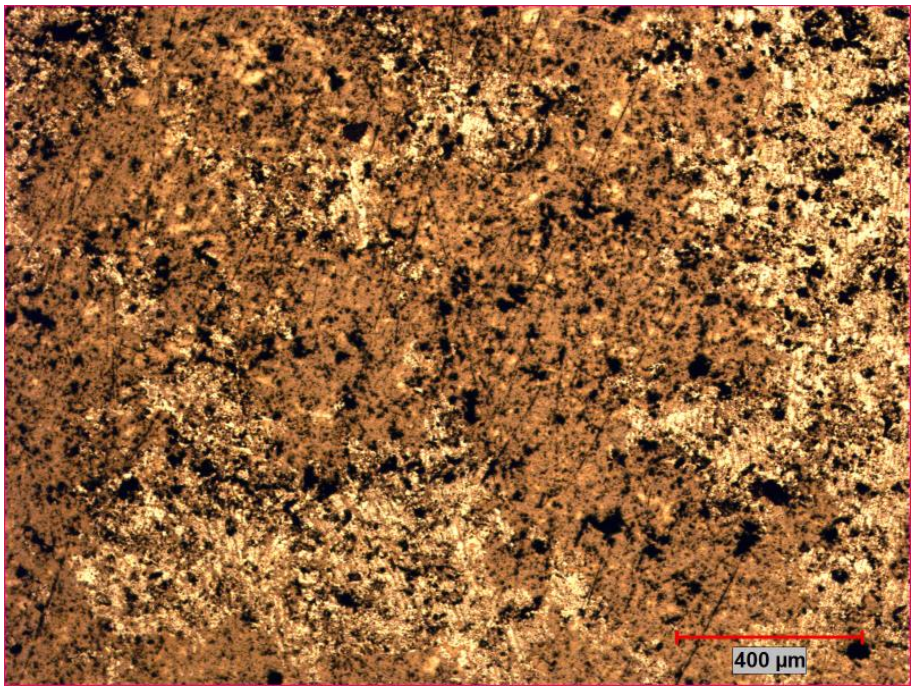


(e)

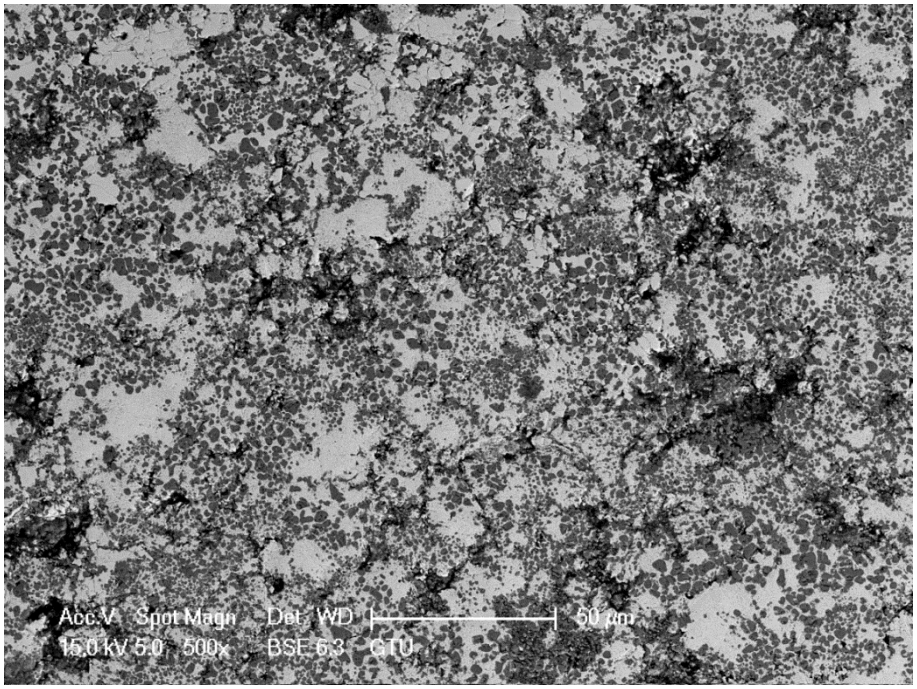


(f)

Figure 3.25. Micrographs of KB 1275-7 at a) 50X b)500X c) 1000X d) 2000X e) 5000X and f) tipical particle sizes of TiCs at 5000X ((continuum).

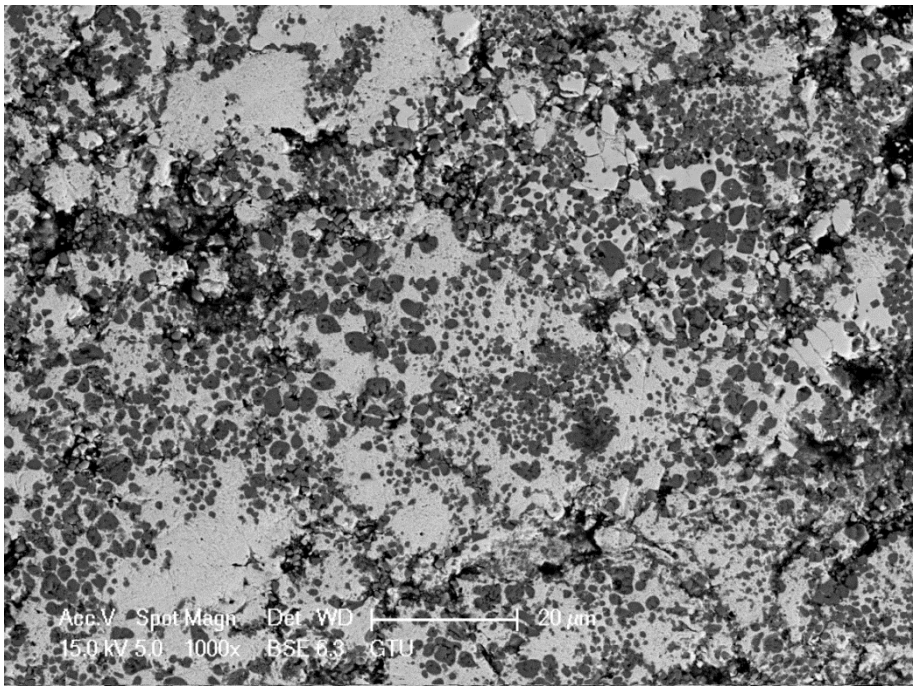


(a)

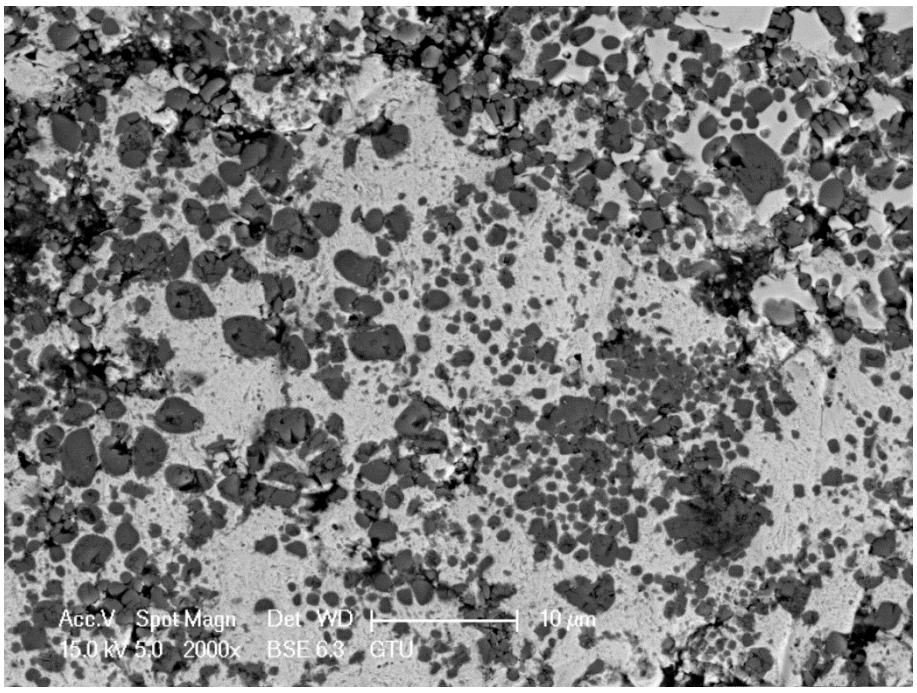


(b)

Figure 3.26. Micrographs of KB 1350-3 at a) 50X b) 500X c) 1000X d) 2000X e) 5000X and f) tipical particle sizes of TiCs at 5000X.

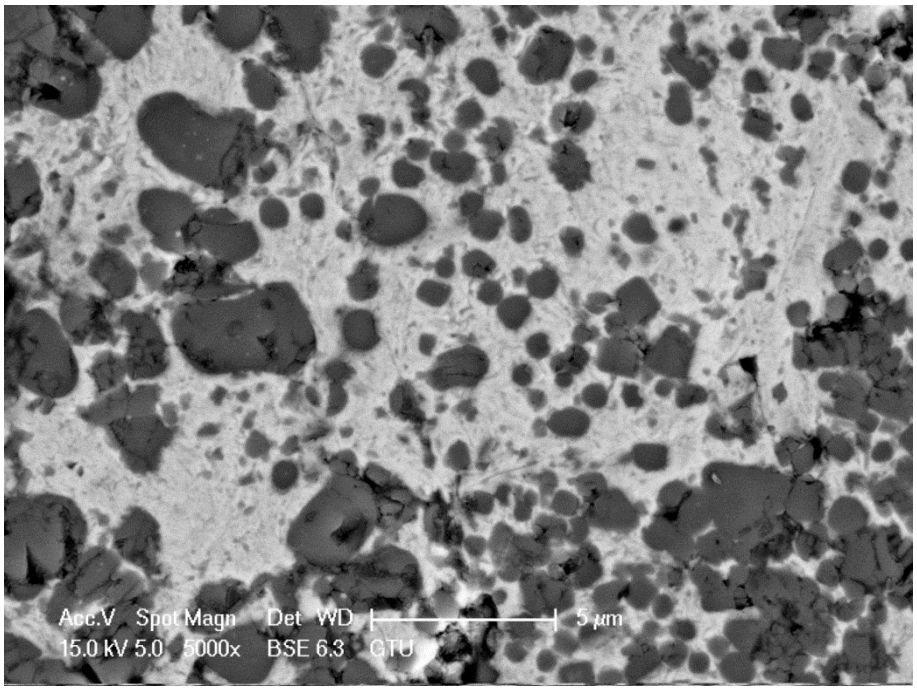


(c)

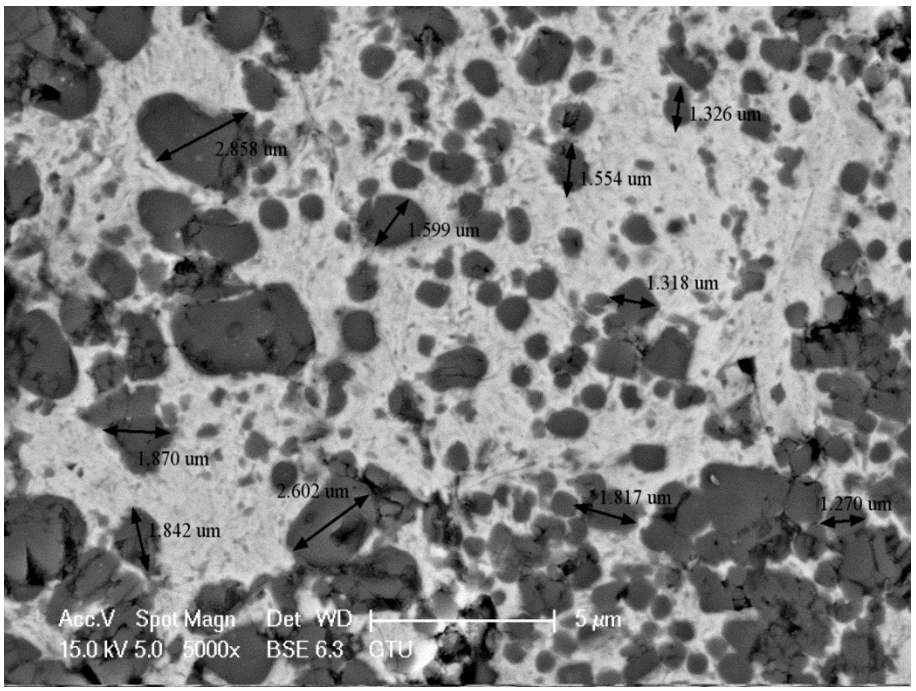


(d)

Figure 3.26. Micrographs of KB 1350-3 at a) 50X b) 500X c) 1000X d) 2000X e) 5000X and f) tipical particle sizes of TiCs at 5000X ((continuum).

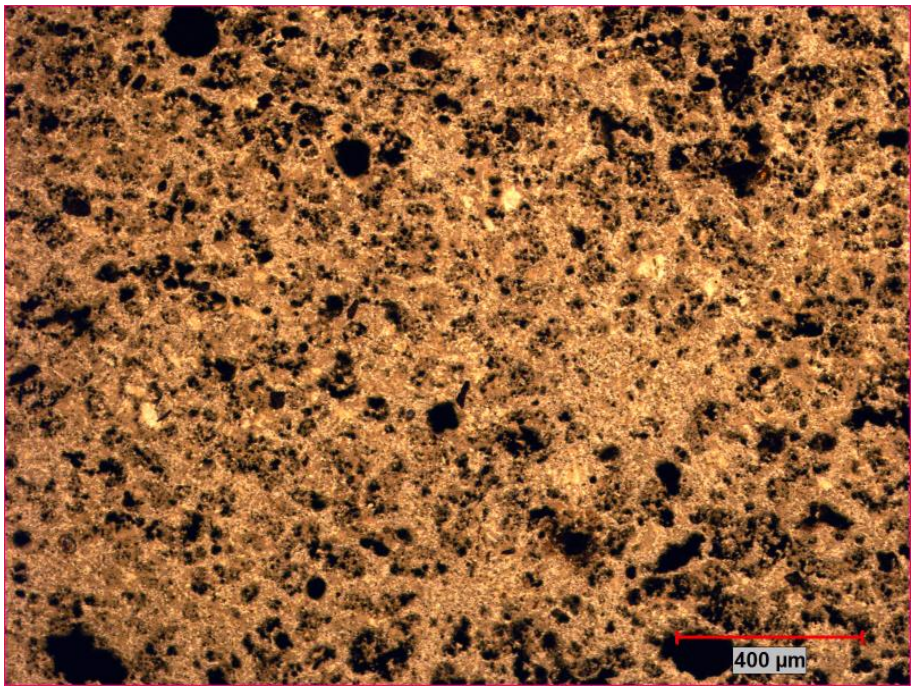


(e)

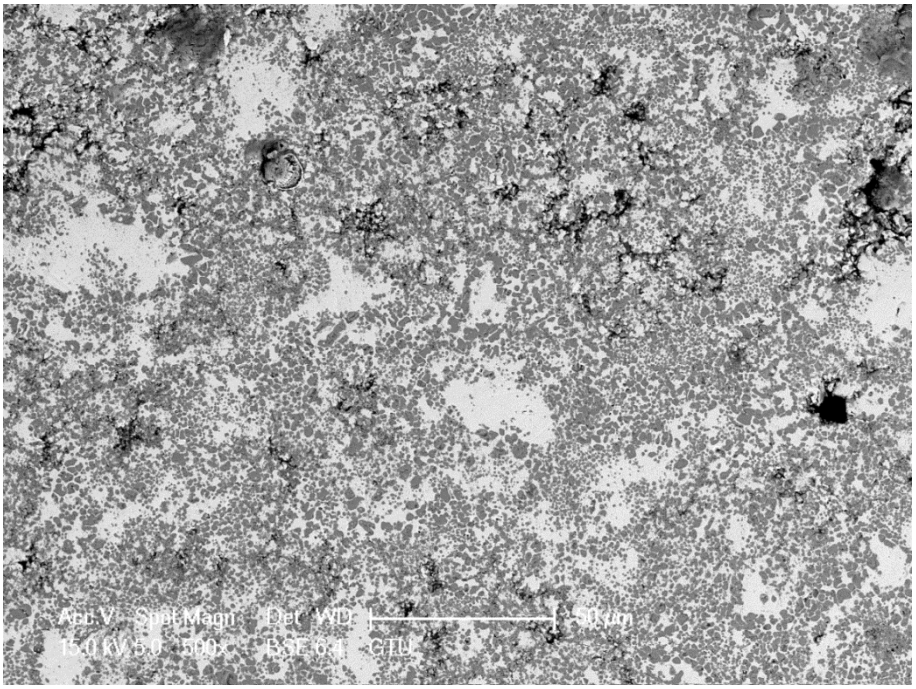


(f)

Figure 3.26. Micrographs of KB 1350-3 at a) 50X b) 500X c) 1000X d) 2000X e) 5000X and f) tipical particle sizes of TiCs at 5000X ((continuum).

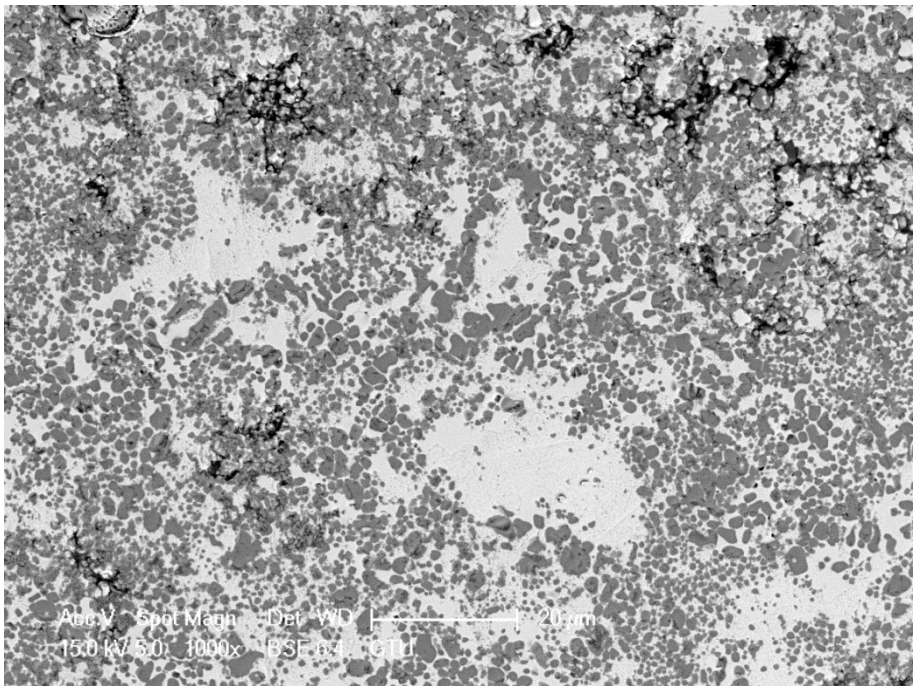


(a)

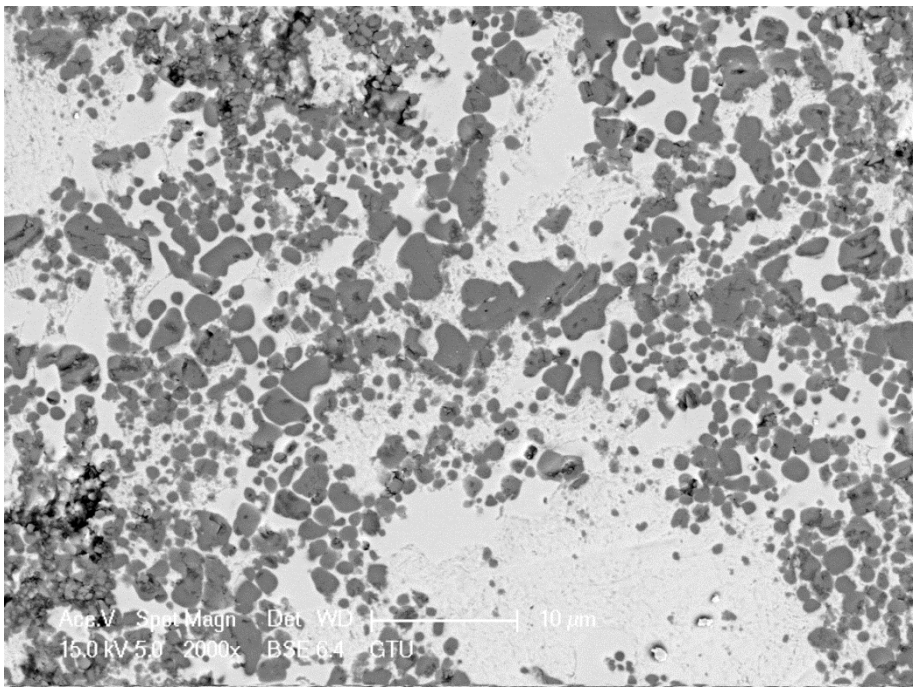


(b)

Figure 3.27. Micrographs of KB 1350-5 at a) 50X b) 500X c) 1000X d) 2000X e) 5000X and f) tipical particle sizes of TiCs at 5000X.

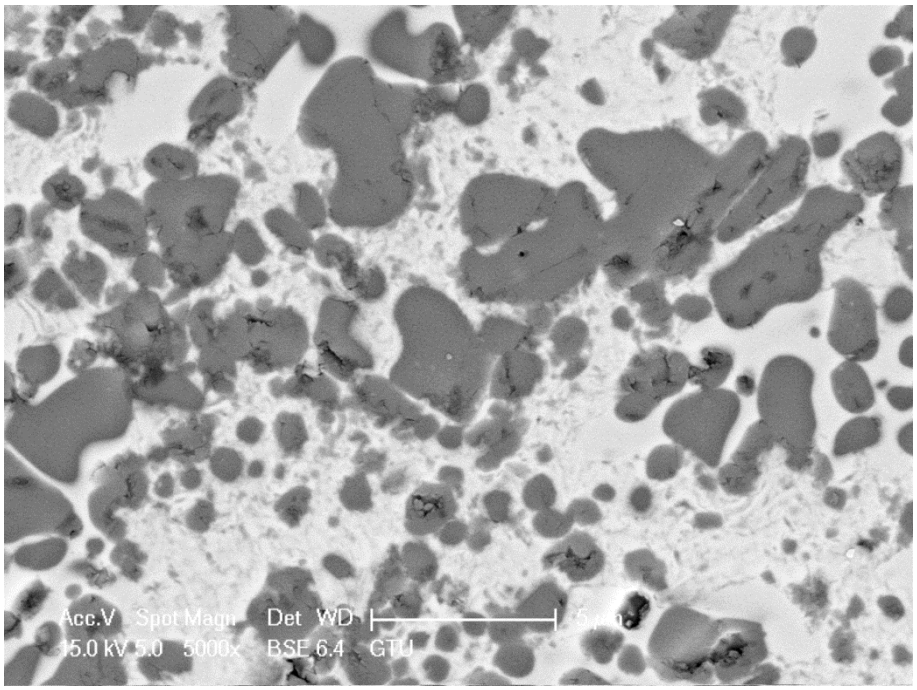


(c)

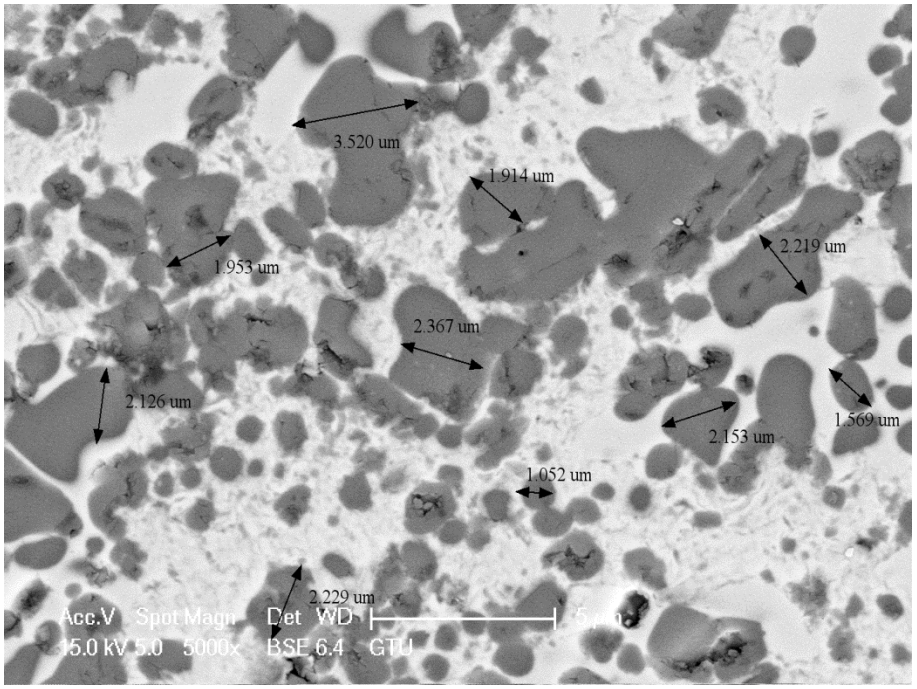


(d)

Figure 3.27. Micrographs of KB 1350-5 at a) 50X b) 500X c) 1000X d) 2000X e) 5000X and f) tipical particle sizes of TiCs at 5000X (continuum).

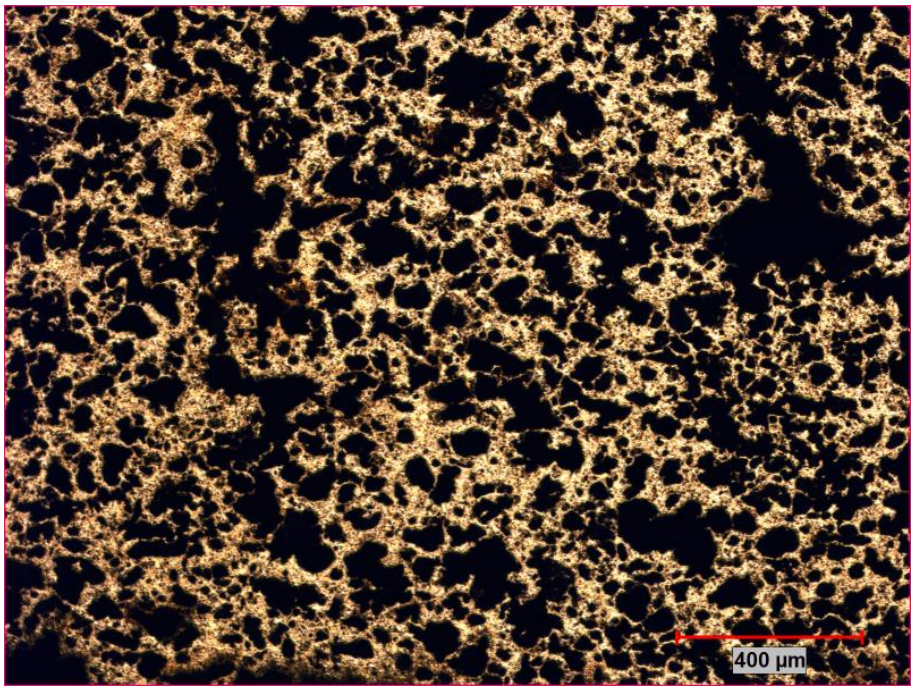


(e)

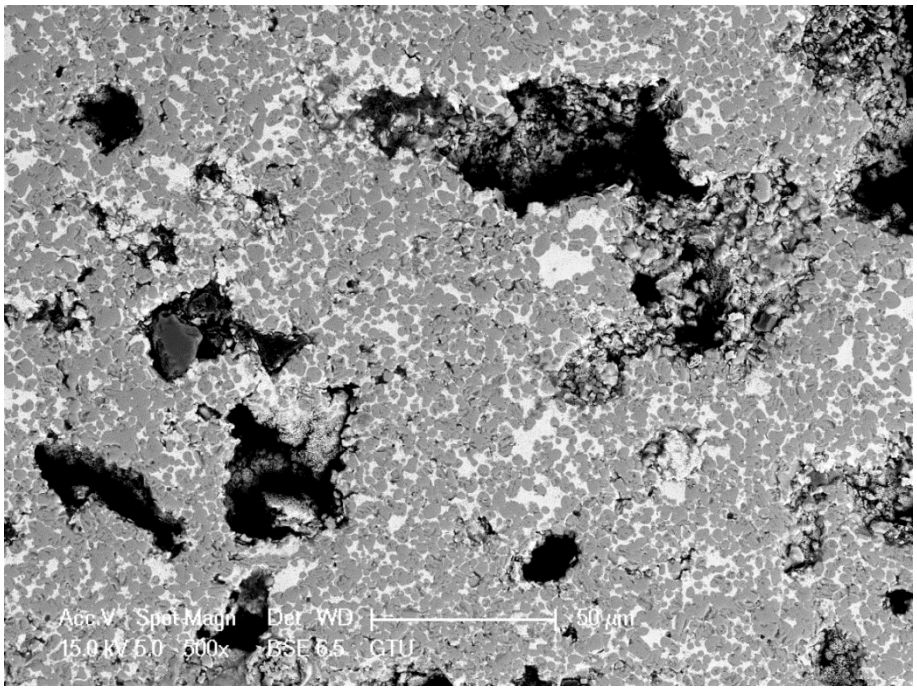


(f)

Figure 3.27. Micrographs of KB 1350-5 at a) 50X b) 500X c) 1000X d) 2000X e) 5000X and f) tipical particle sizes of TiCs at 5000X (continuum).

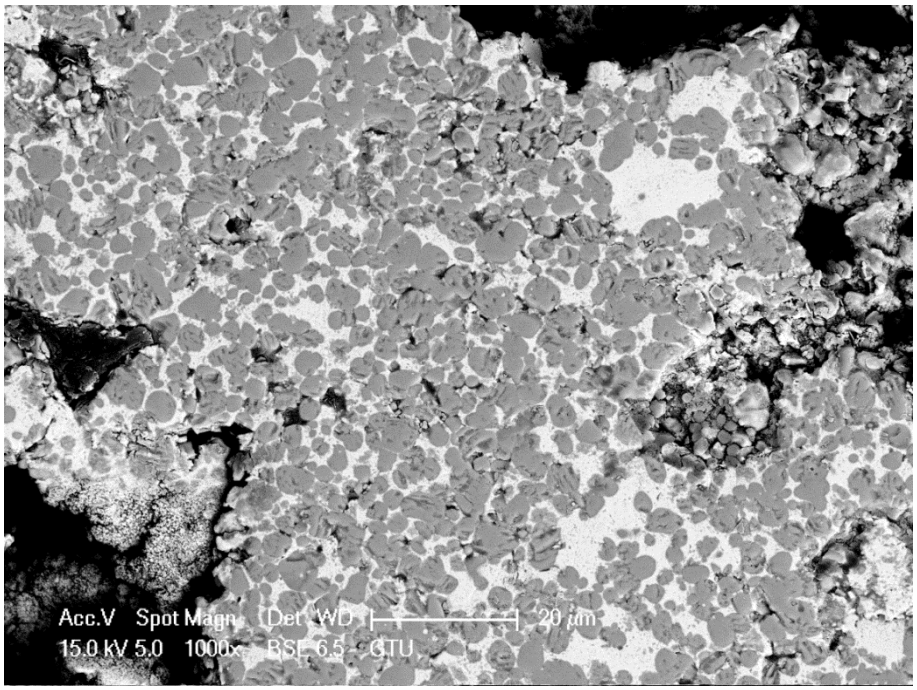


(a)

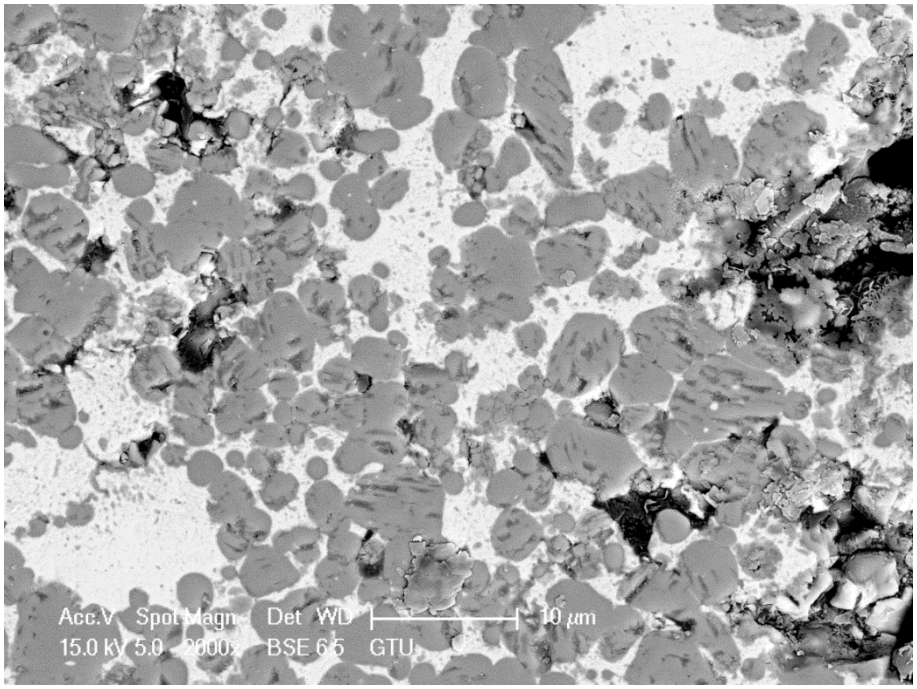


(b)

Figure 3.28. Micrographs of KB 1350-7 at a) 50X b) 500X c) 1000X d) 2000X e) 5000X and f) tipical particle sizes of TiCs at 5000X.

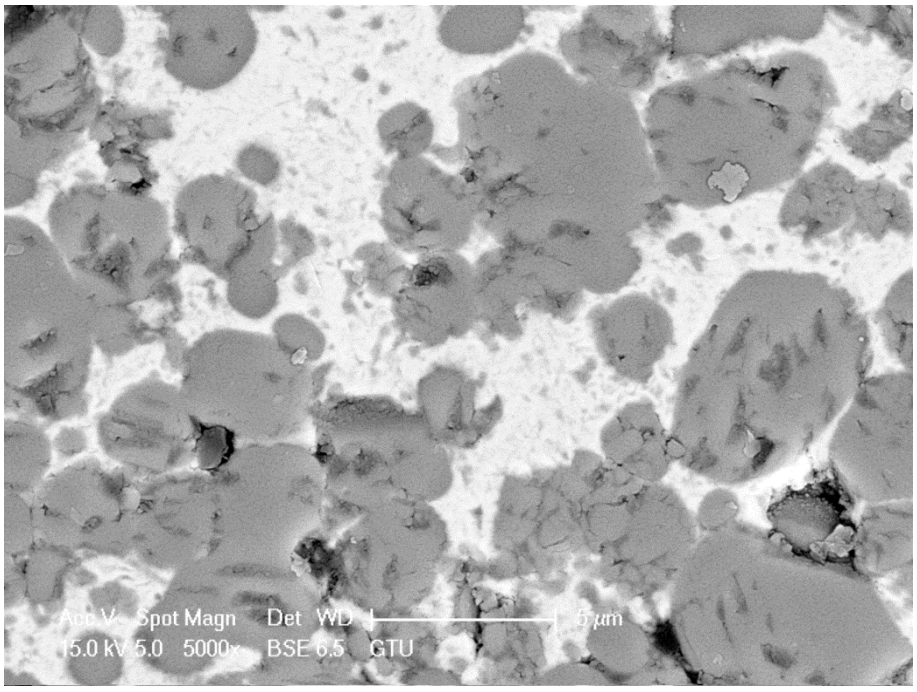


(c)

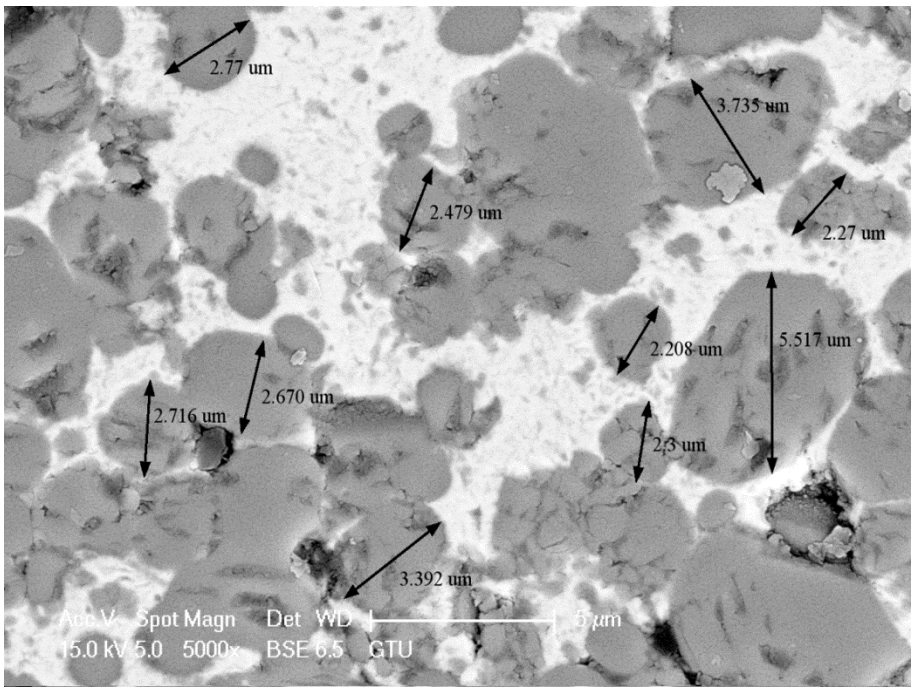


(d)

Figure 3.28. Micrographs of KB 1350-7 at a) 50X b) 500X c) 1000X d) 2000X e) 5000X and f) tipical particle sizes of TiCs at 5000X (continuum).

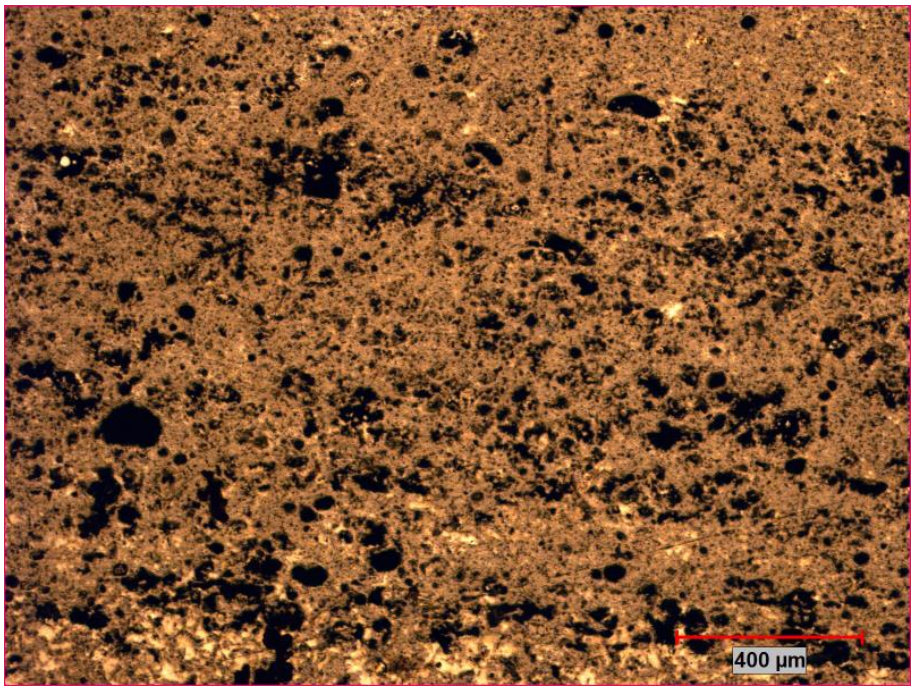


(e)

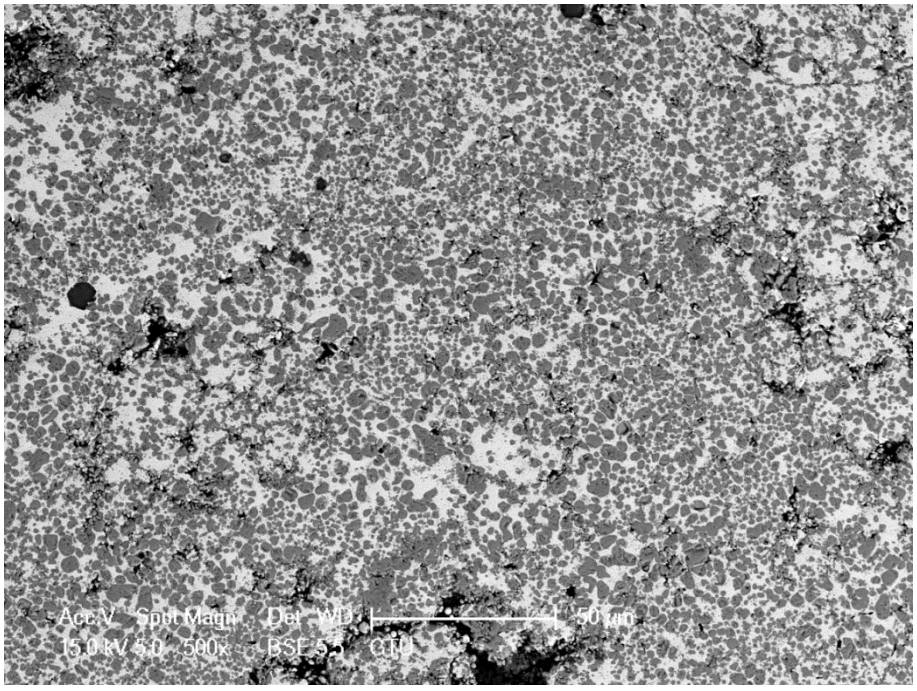


(f)

Figure 3.28. Micrographs of KB 1350-7 at a) 50X b) 500X c) 1000X d) 2000X e) 5000X and f) tipical particle sizes of TiCs at 5000X (continuum).

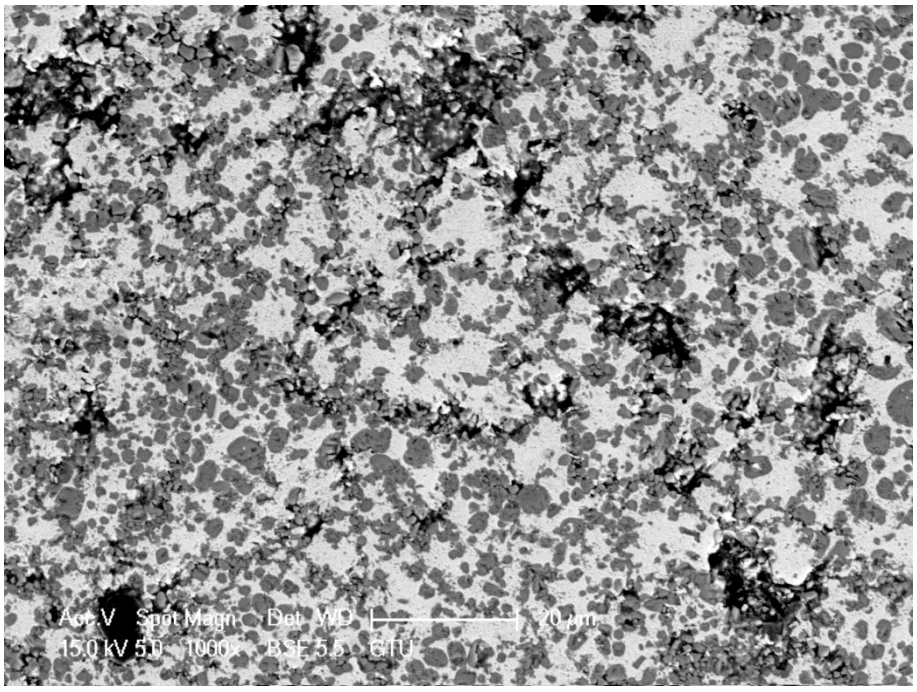


(a)

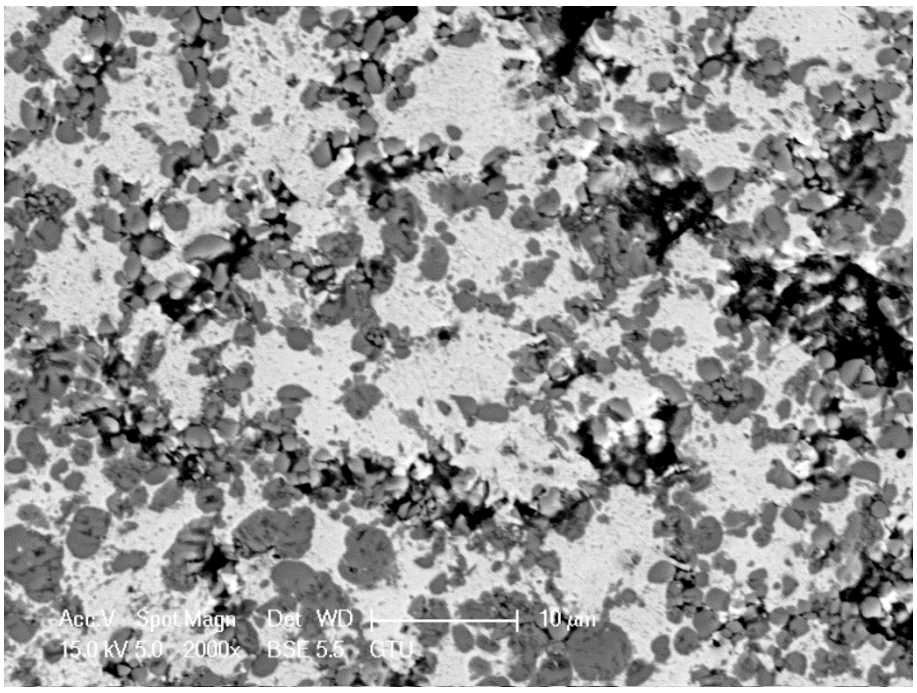


(b)

Figure 3.29. Micrographs of KB 1425-3 at a) 50X b) 500X c) 1000X d) 2000X e) 5000X and f) tipical particle sizes of TiCs at 5000X.

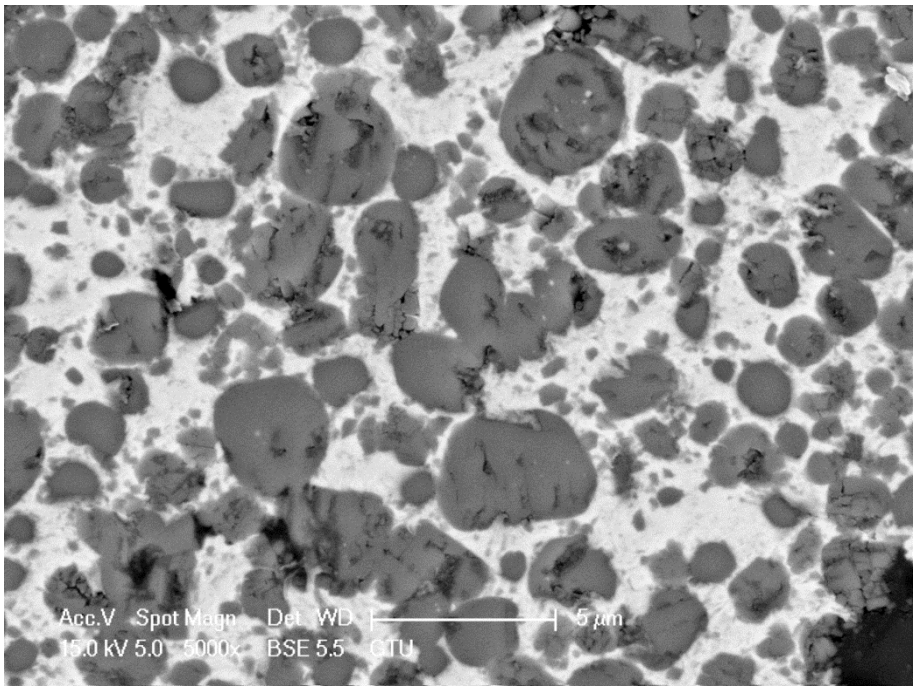


(c)

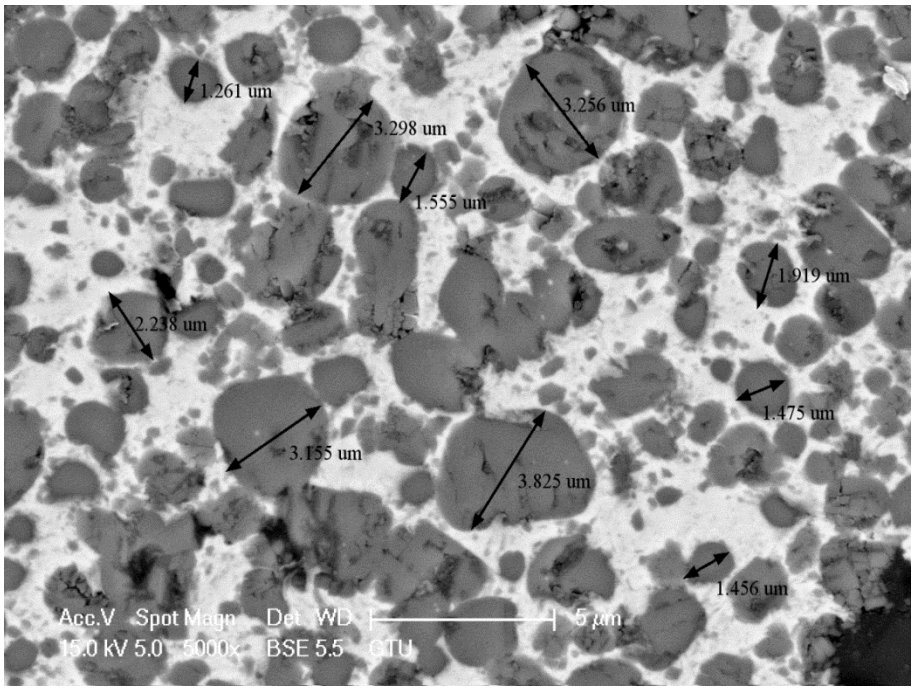


(d)

Figure 3.29. Micrographs of KB 1425-3 at a) 50X b) 500X c) 1000X d) 2000X e) 5000X and f) tipical particle sizes of TiCs at 5000X ((continuum).

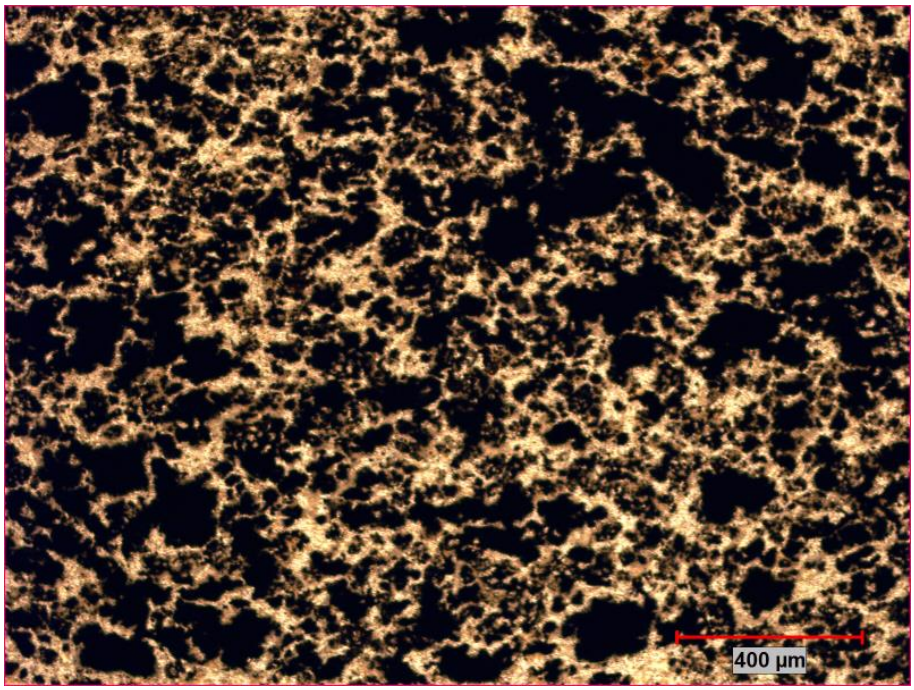


(e)

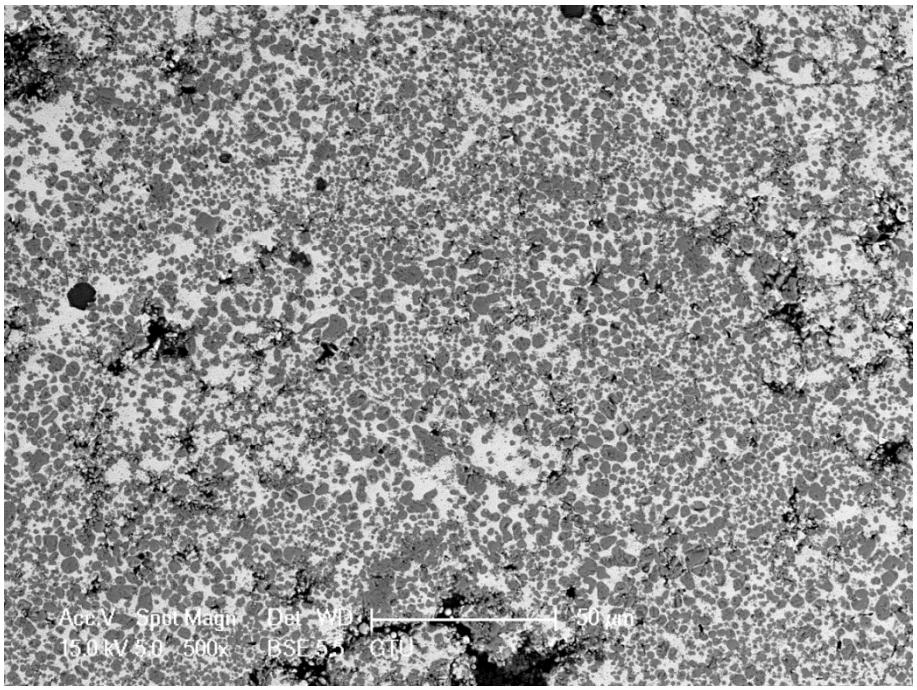


(f)

Figure 3.29. Micrographs of KB 1425-3 at a) 50X b) 500X c) 1000X d) 2000X e) 5000X and f) tipical particle sizes of TiCs at 5000X ((continuum).

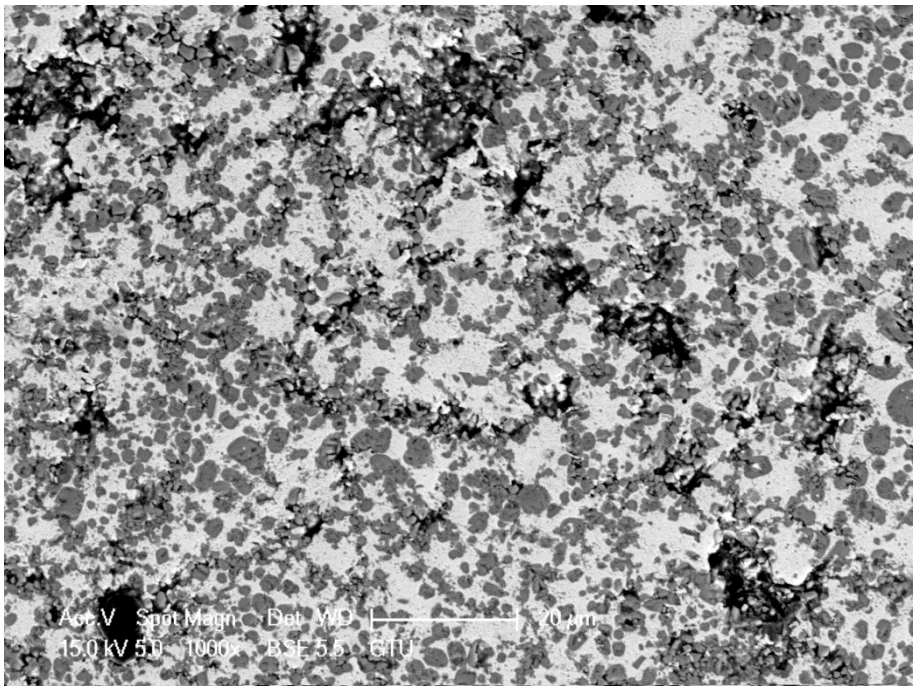


(a)

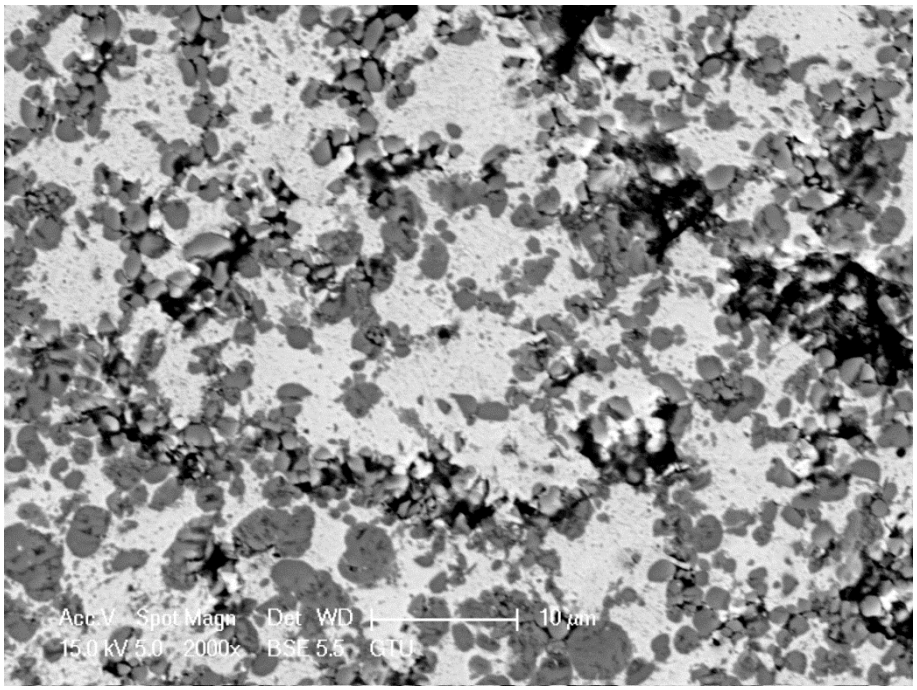


(b)

Figure 3.30. Micrographs of KB 1425-5 at a) 50X b) 500X c) 1000X d) 2000X e) 5000X and f) tipical particle sizes of TiCs at 5000X.

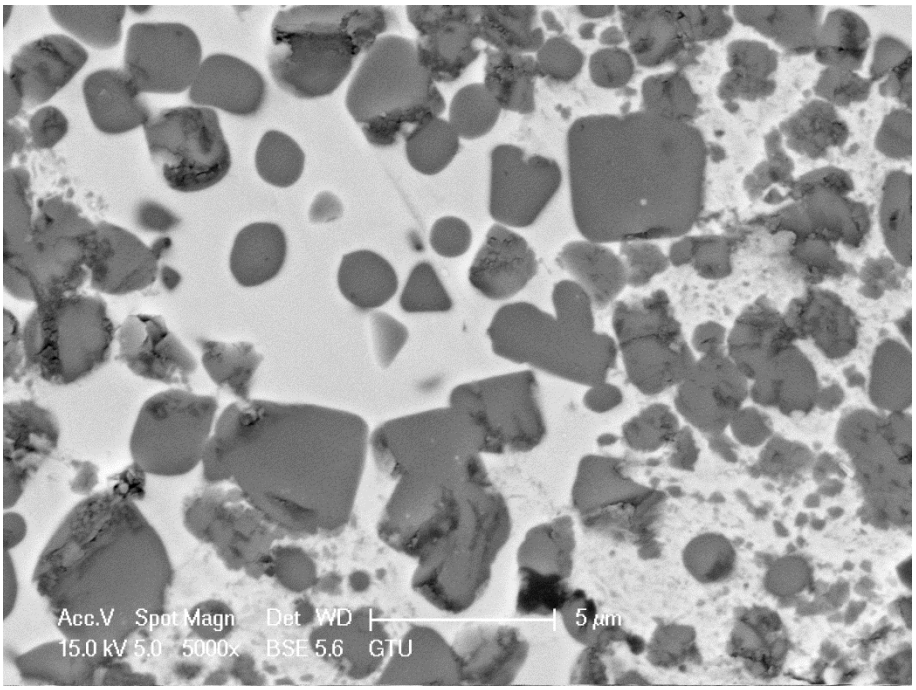


(c)

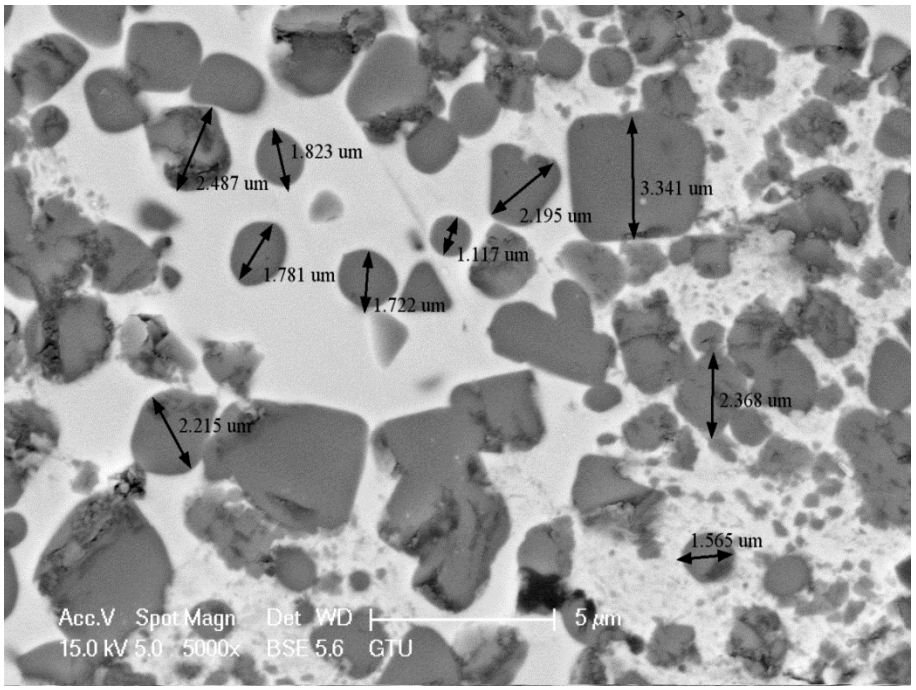


(d)

Figure 3.30. Micrographs of KB 1425-5 at a) 50X b) 500X c) 1000X d) 2000X e) 5000X and f) tipical particle sizes of TiCs at 5000X ((continuum).

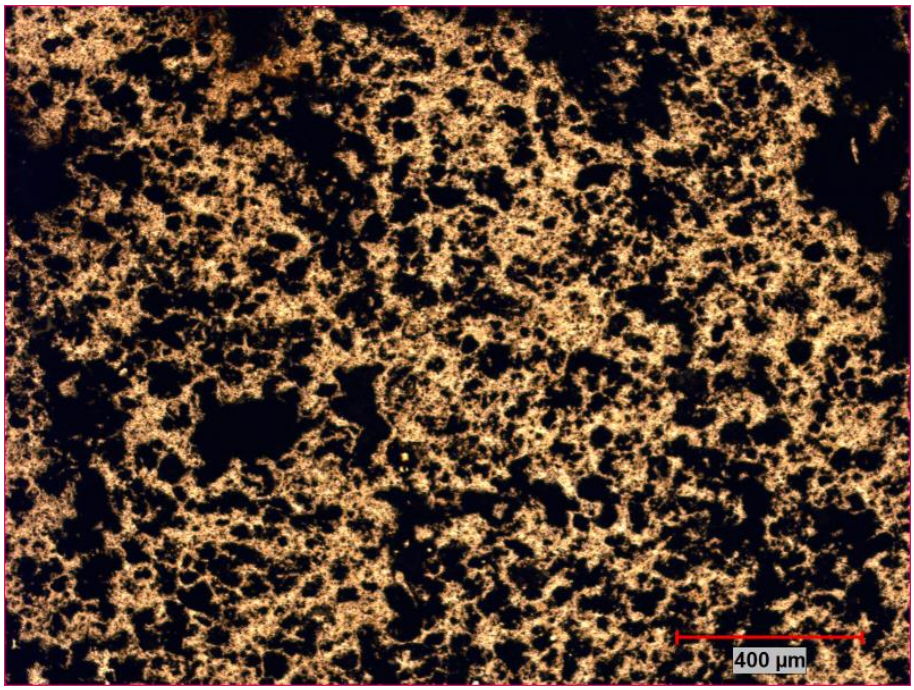


(e)

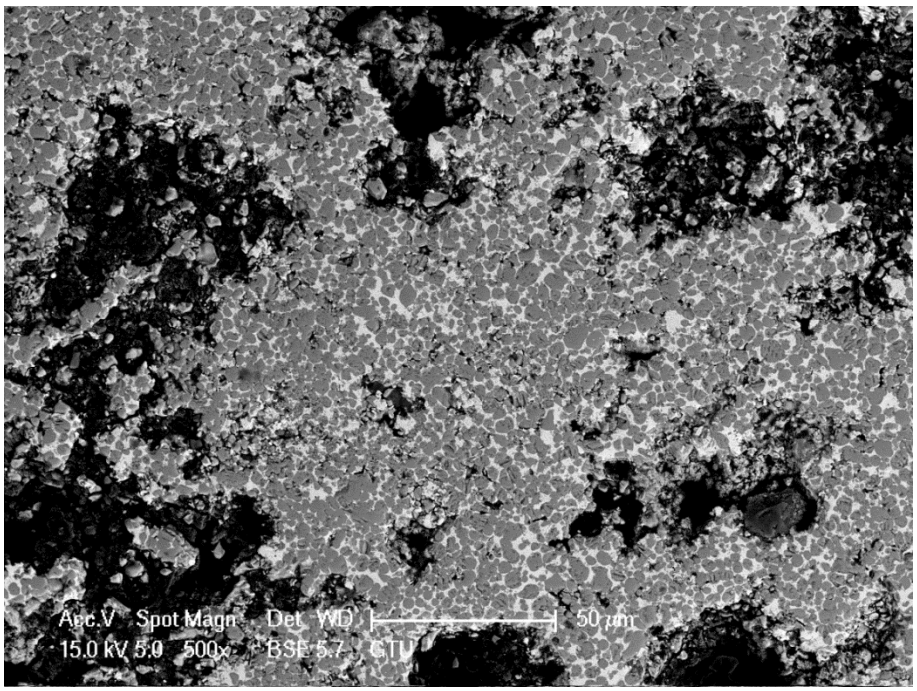


(f)

Figure 3.30. Micrographs of KB 1425-5 at a) 50X b) 500X c) 1000X d) 2000X e) 5000X and f) tipical particle sizes of TiCs at 5000X ((continuum).

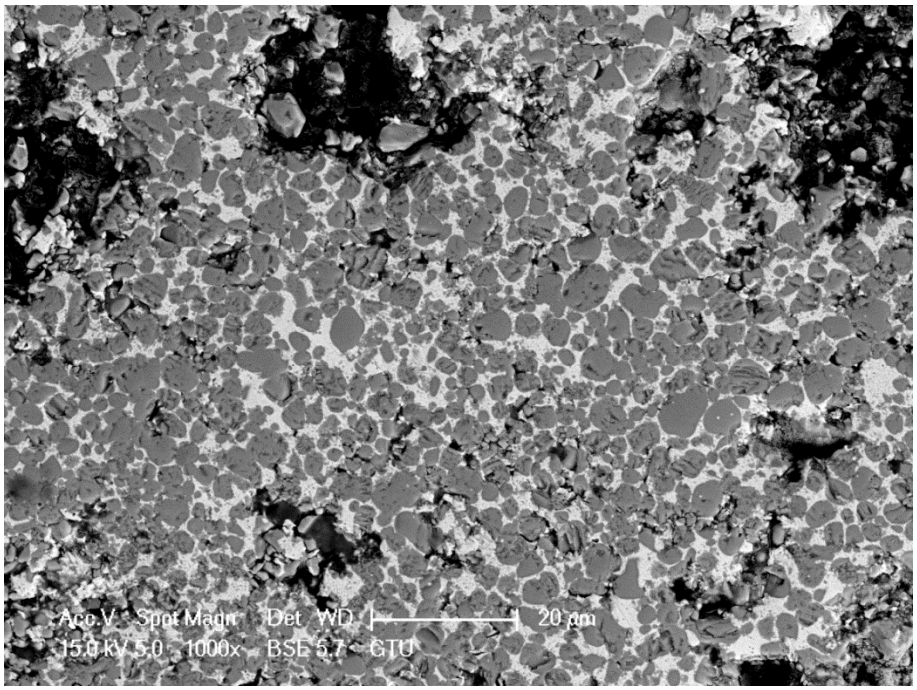


(a)

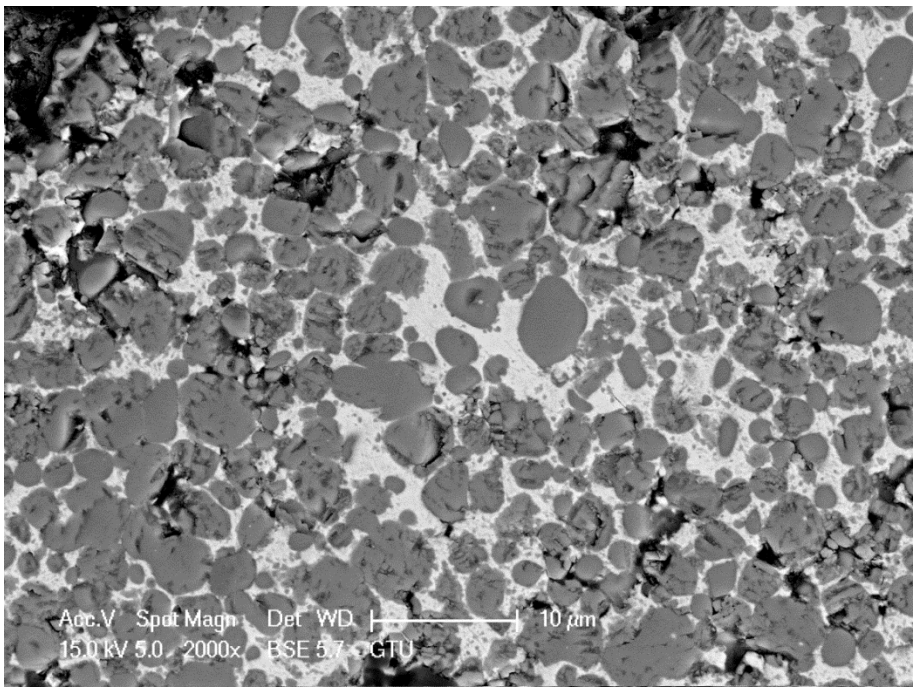


(b)

Figure 3.31. Micrographs of KB 1425-7 at a) 50X b) 500X c) 1000X d) 2000X e) 5000X and f) tipical particle sizes of TiCs at 5000X.

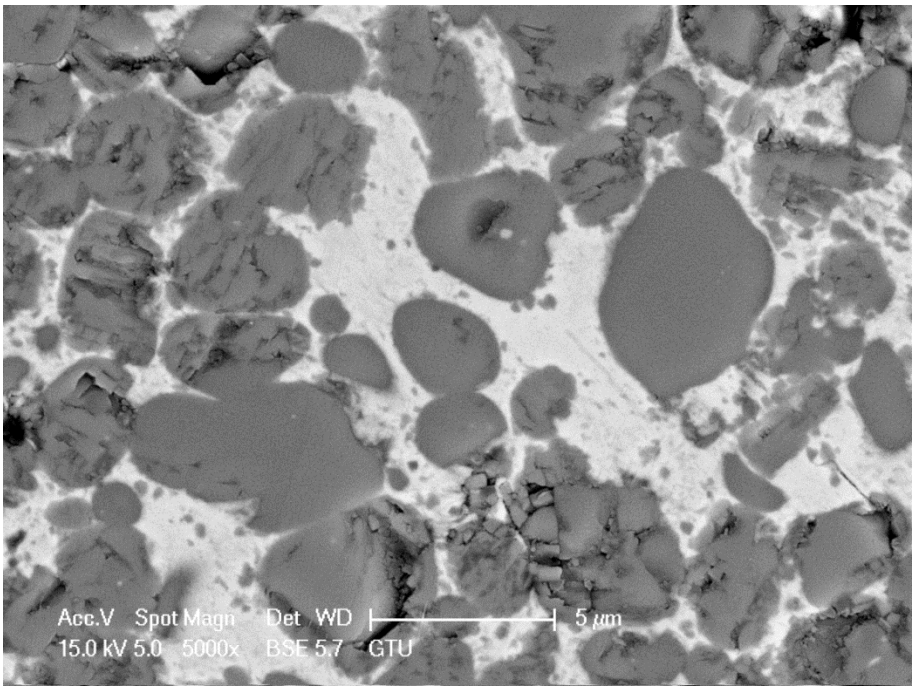


(c)

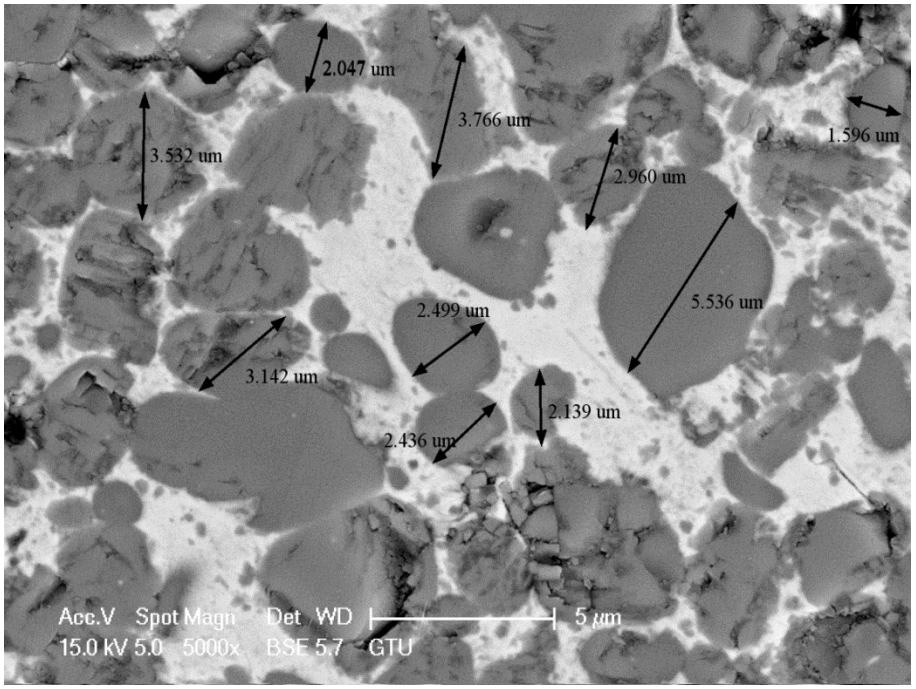


(d)

Figure 3.31. Micrographs of KB 1425-7 at a) 50X b) 500X c) 1000X d) 2000X e) 5000X and f) tipical particle sizes of TiCs at 5000X (continuum).

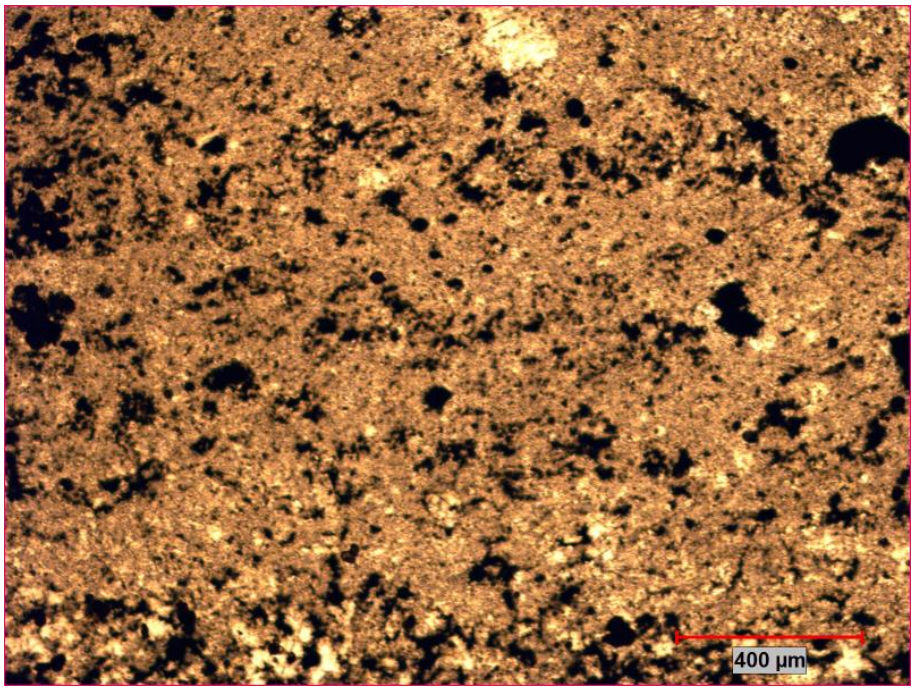


(e)

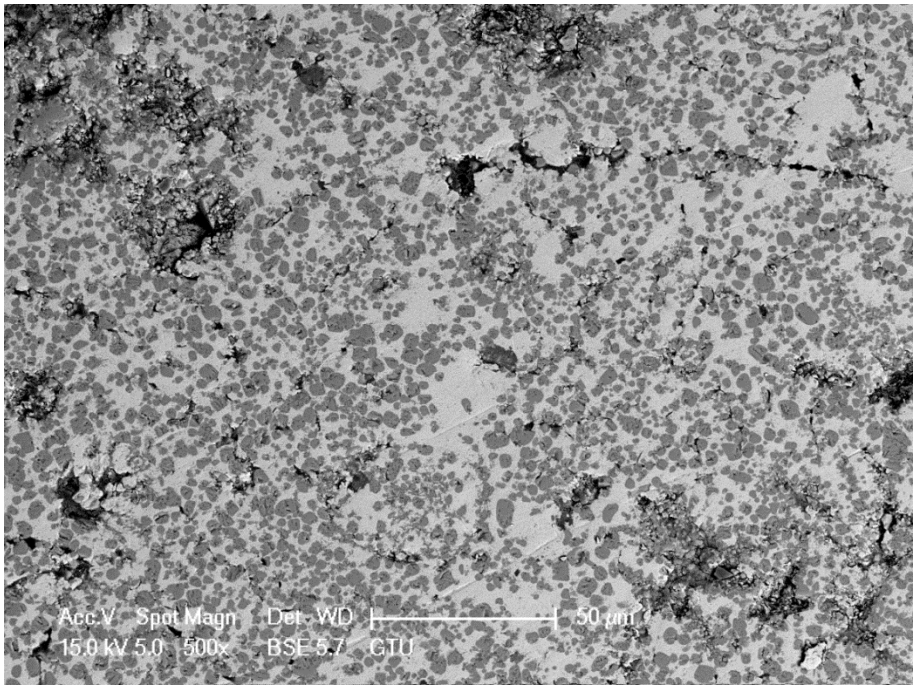


(f)

Figure 3.31. Micrographs of KB 1425-7 at a) 50X b) 500X c) 1000X d) 2000X e) 5000X and f) tipical particle sizes of TiCs at 5000X ((continuum).

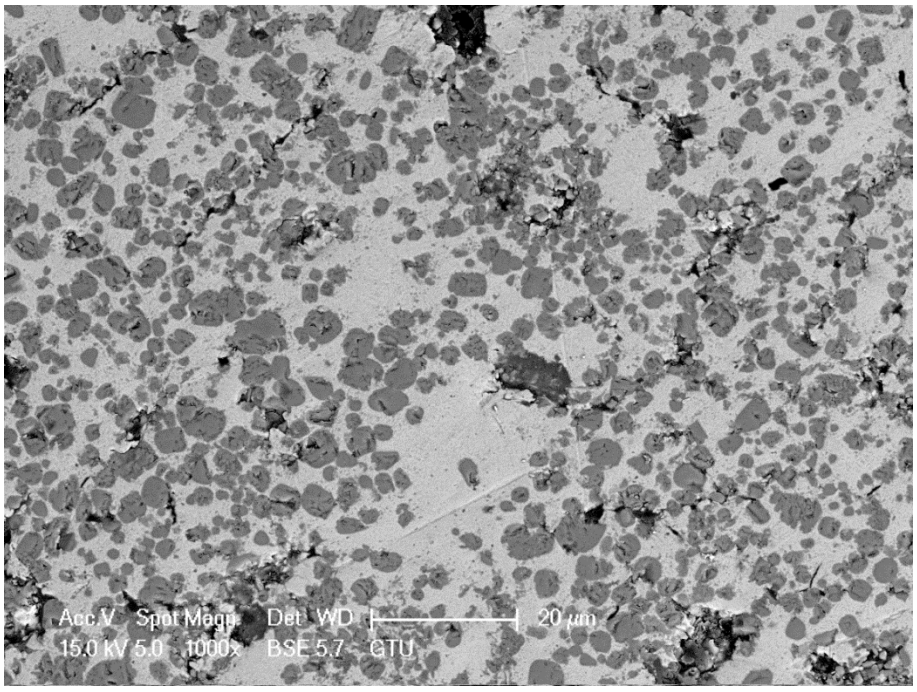


(a)

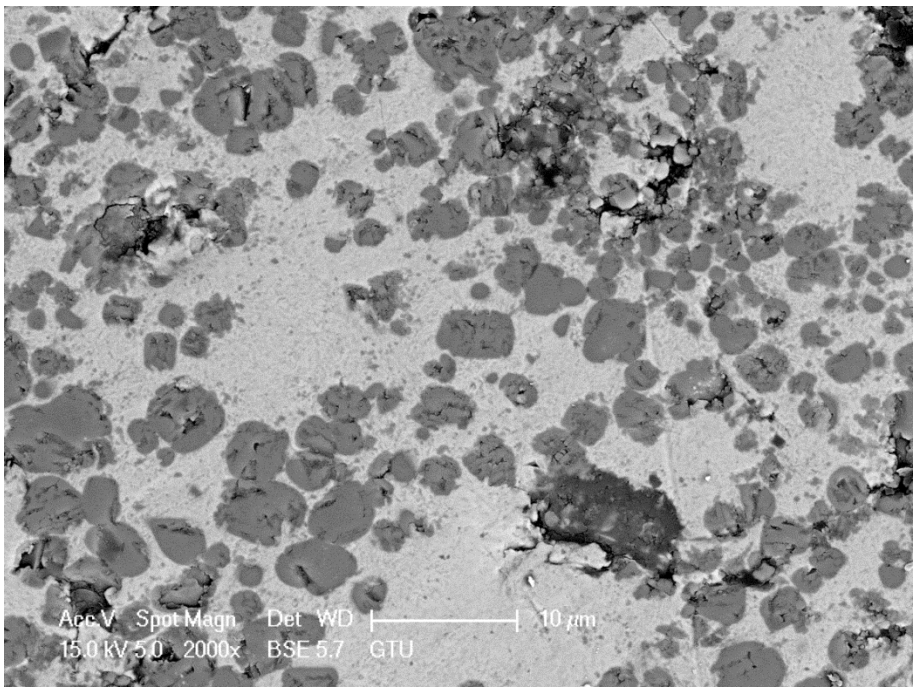


(b)

Figure 3.32. Micrographs of KB 1500-3 at a) 50X b) 500X c) 1000X d) 2000X e) 5000X and f) tipical particle sizes of TiCs at 5000X.

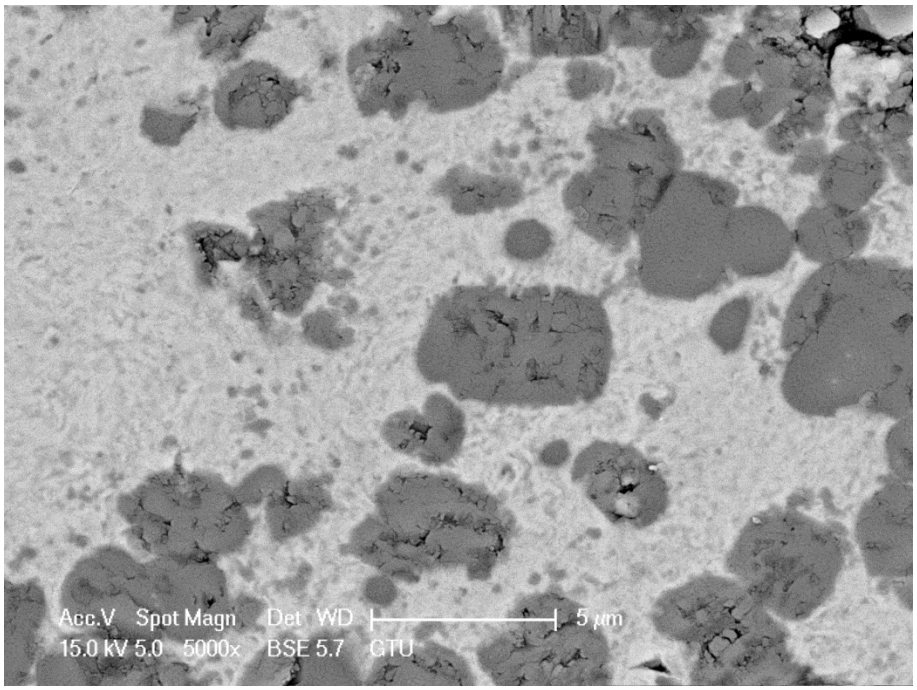


(c)

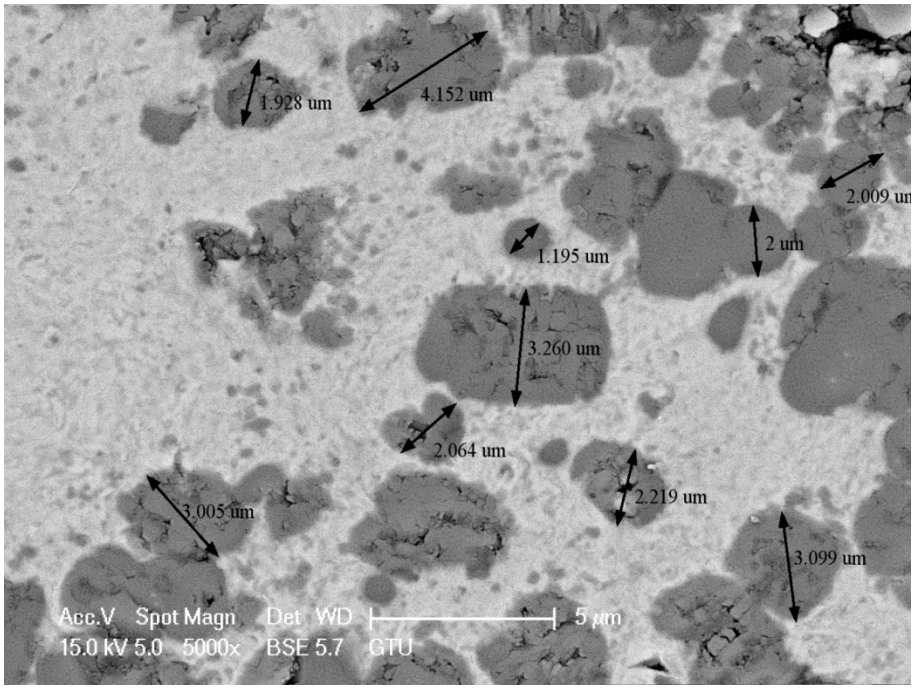


(d)

Figure 3.32. Micrographs of KB 1500-3 at a) 50X b) 500X c) 1000X d) 2000X e) 5000X and f) tipical particle sizes of TiCs at 5000X ((continuum).

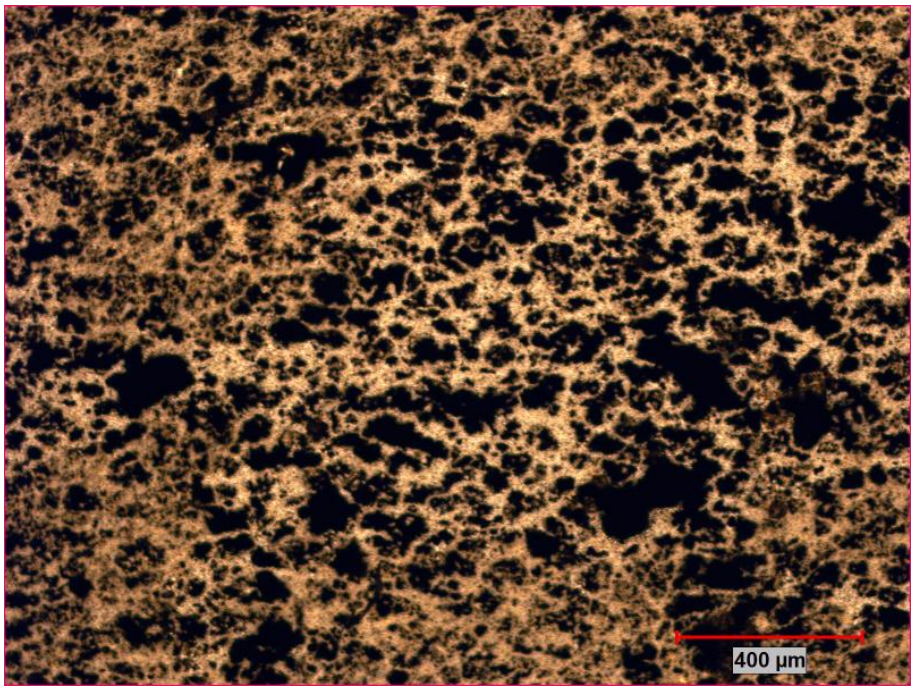


(e)

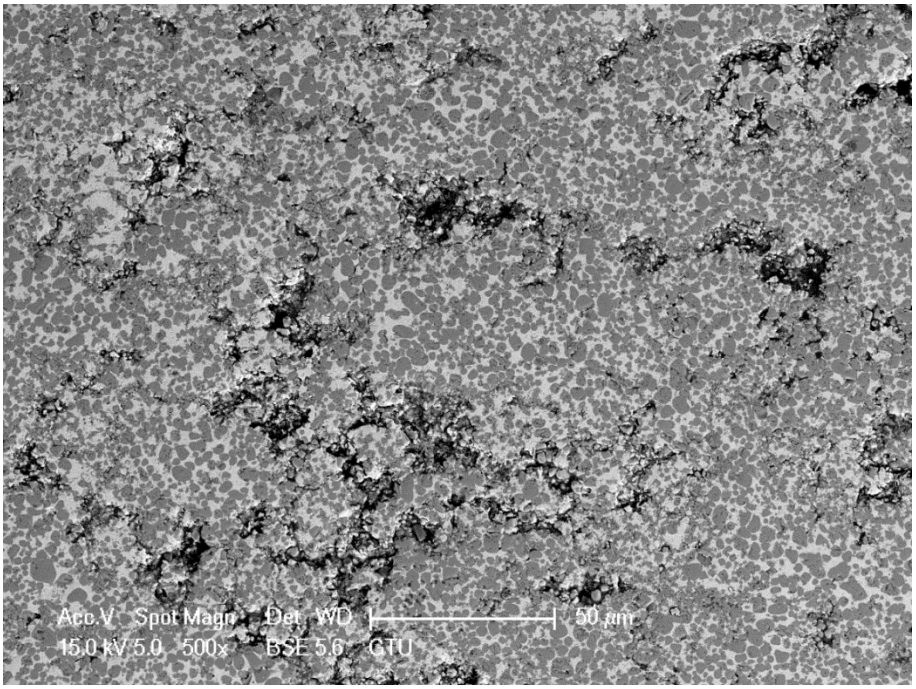


(f)

Figure 3.32. Micrographs of KB 1500-3 at a) 50X b) 500X c) 1000X d) 2000X e) 5000X and f) tipical particle sizes of TiCs at 5000X ((continuum).

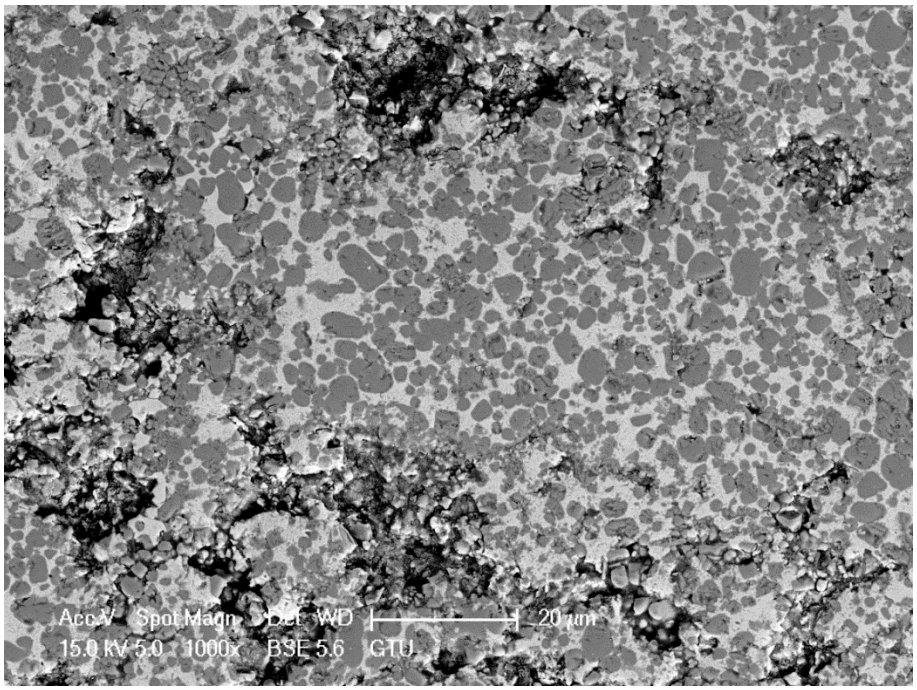


(a)

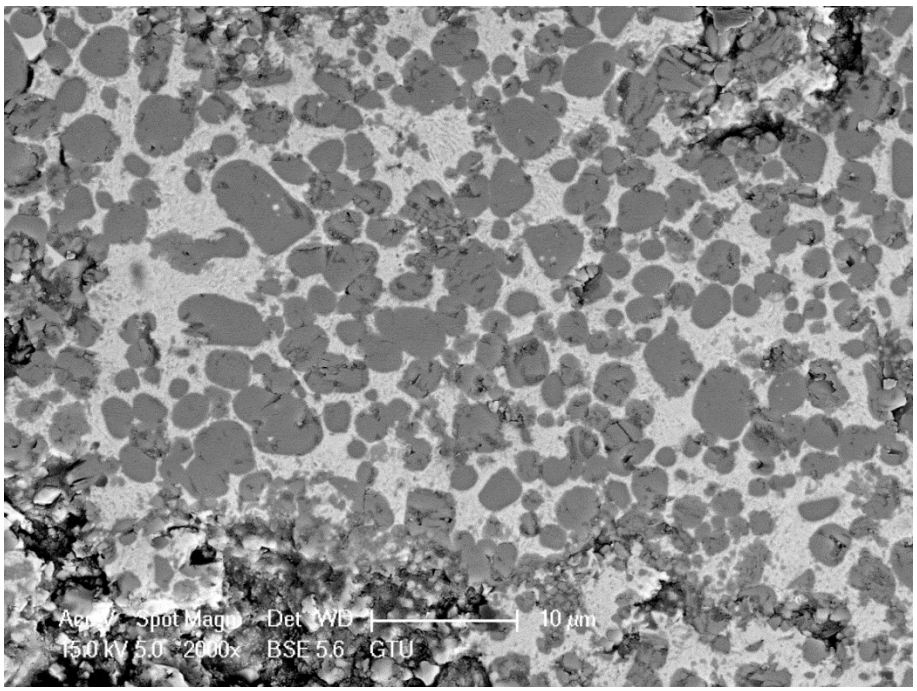


(b)

Figure 3.33. Micrographs of KB 1500-5 at a) 50X b) 500X c) 1000X d) 2000X e) 5000X and f) tipical particle sizes of TiCs at 5000X.

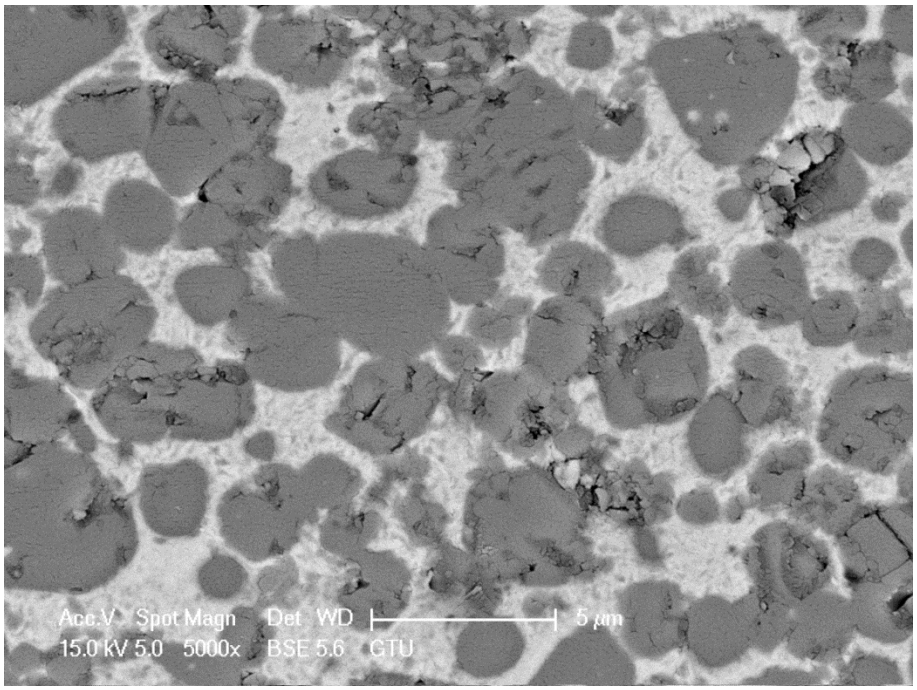


(c)

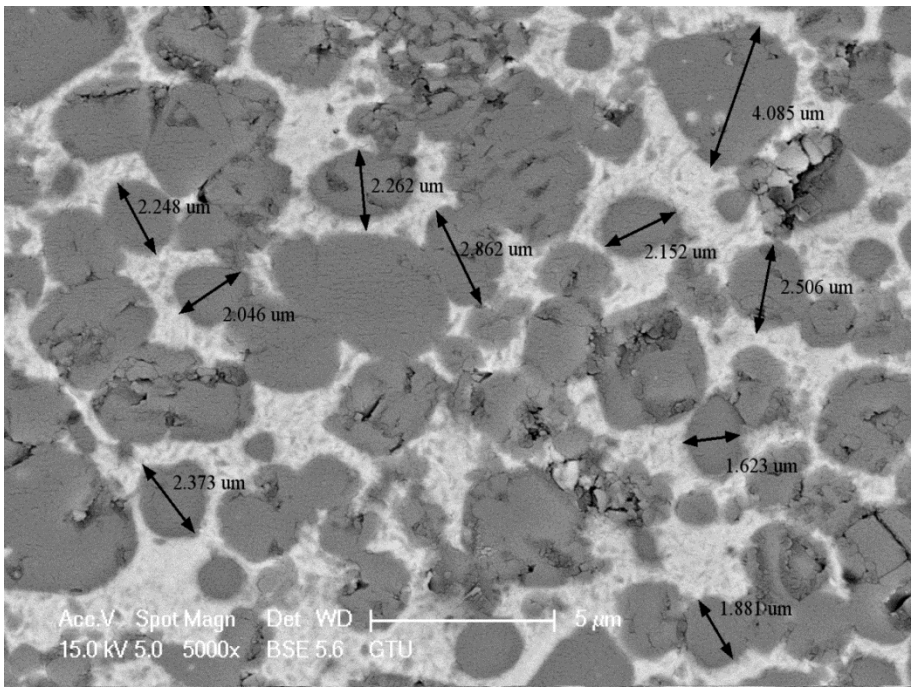


(d)

Figure 3.33. Micrographs of KB 1500-5 at a) 50X b) 500X c) 1000X d) 2000X e) 5000X and f) tipical particle sizes of TiCs at 5000X ((continuum).

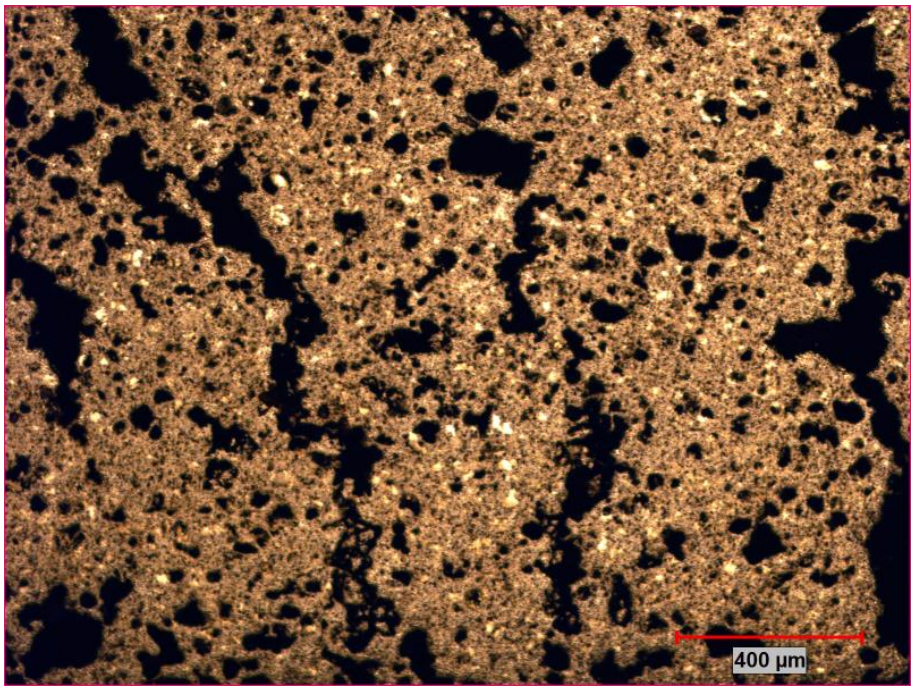


(e)

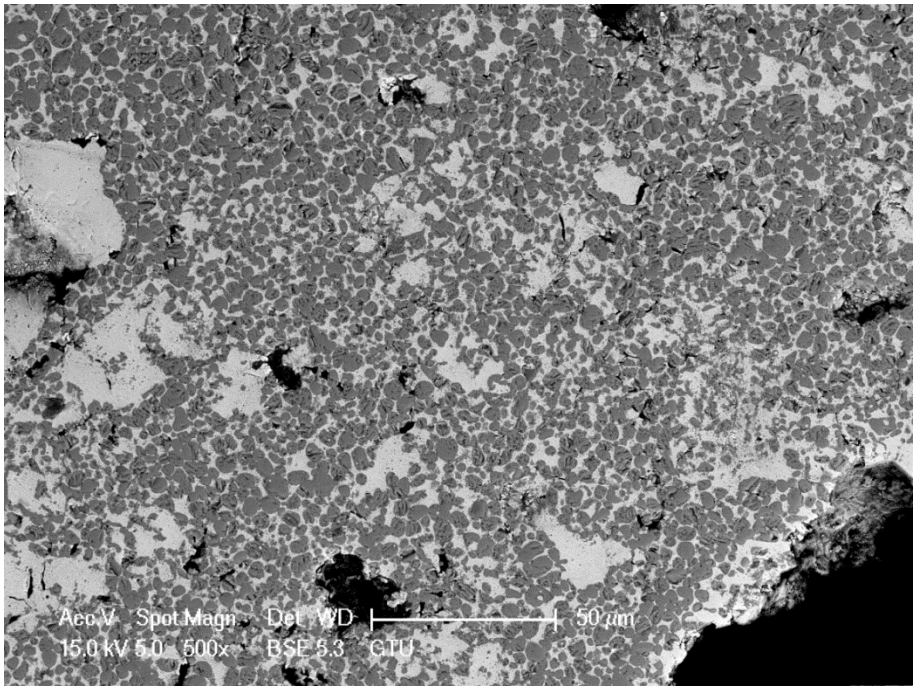


(f)

Figure 3.33. Micrographs of KB 1500-5 at a) 50X b) 500X c) 1000X d) 2000X e) 5000X and f) tipical particle sizes of TiCs at 5000X ((continuum).

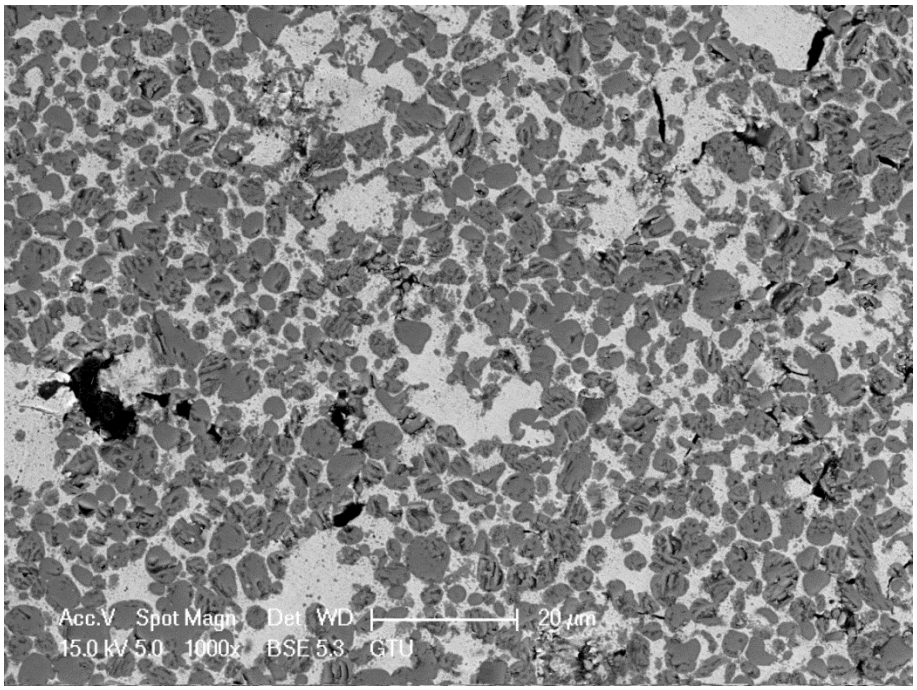


(a)

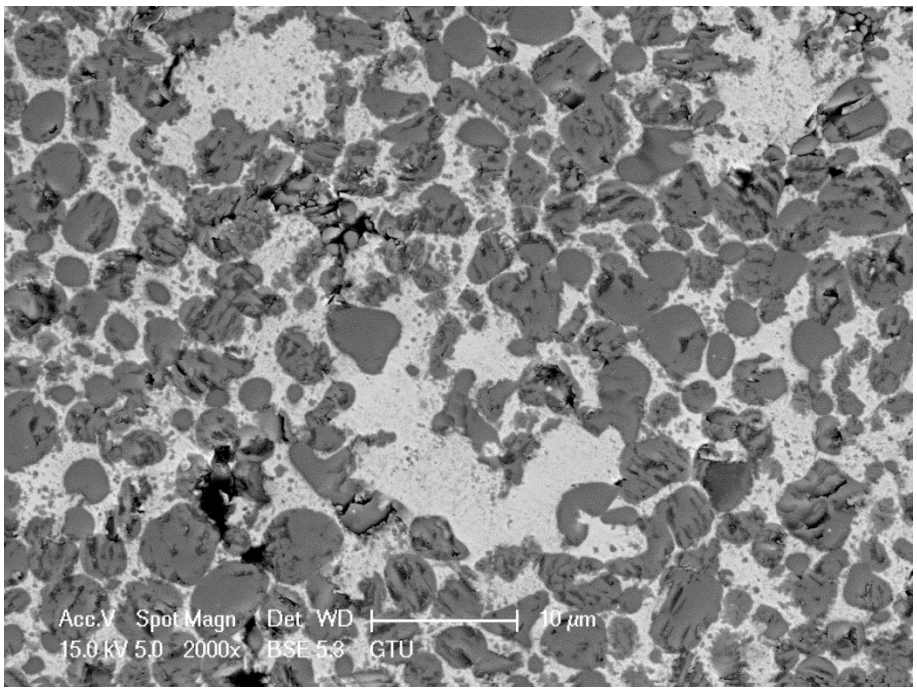


(b)

Figure 3.34. Micrographs of KB 1500-7 at a) 50X b) 500X c) 1000X d) 2000X e) 5000X and f) tipical particle sizes of TiCs at 5000X.

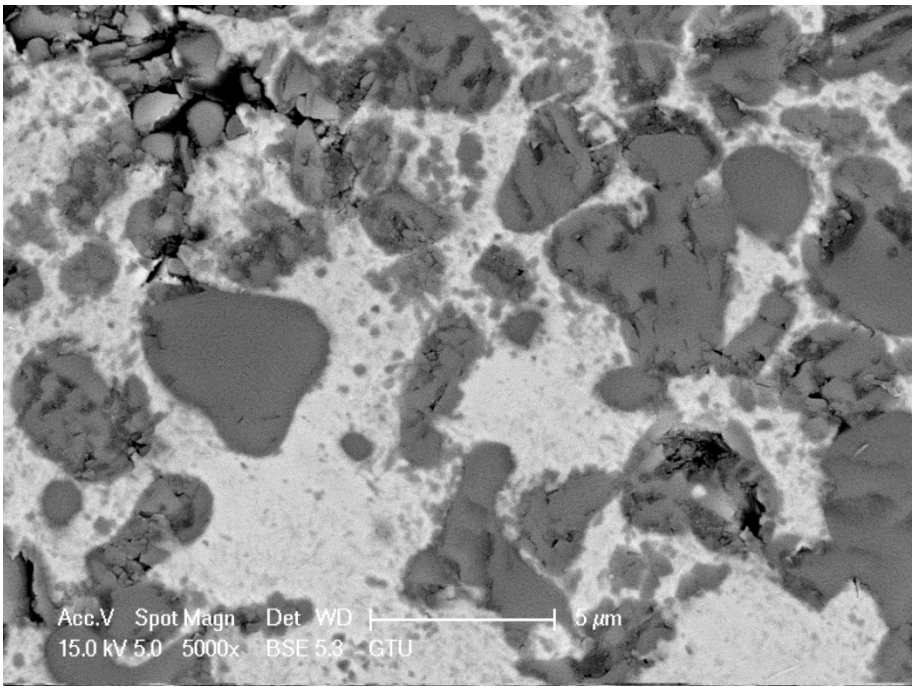


(c)

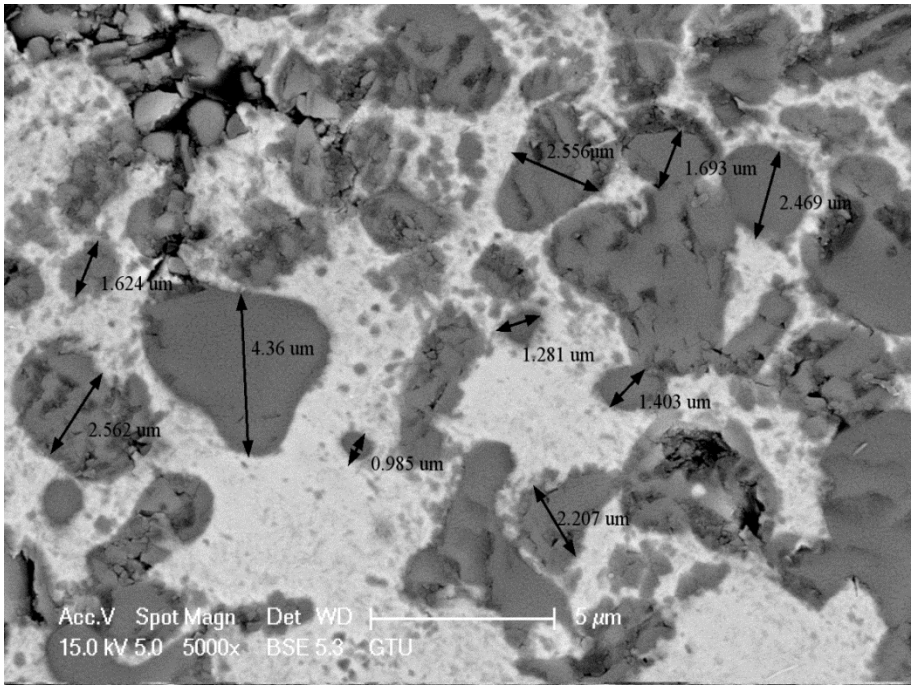


(d)

Figure 3.34. Micrographs of KB 1500-7 at a) 50X b) 500X c) 1000X d) 2000X e) 5000X and f) tipical particle sizes of TiCs at 5000X ((continuum).



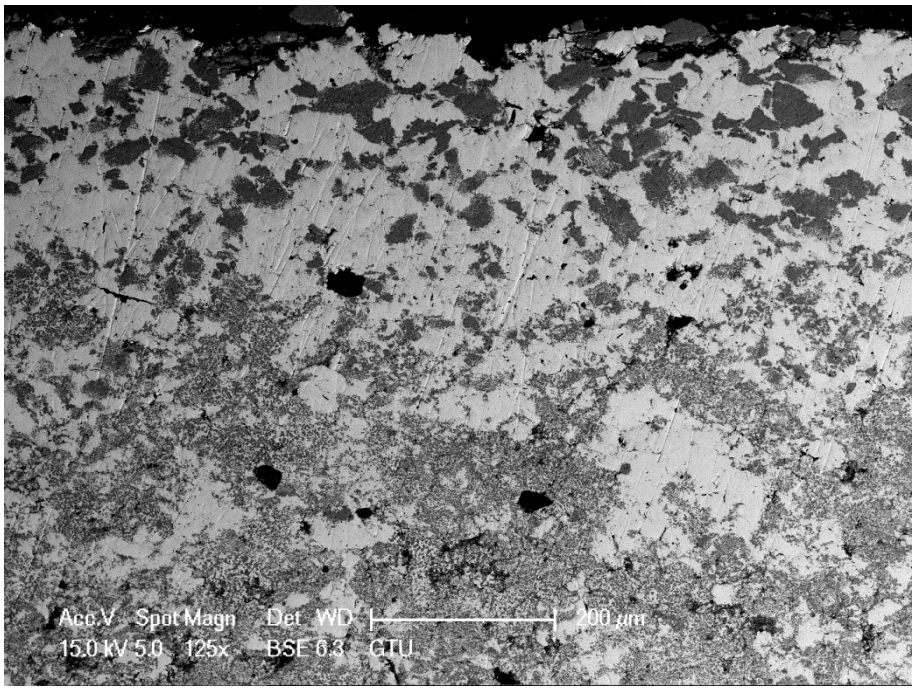
(e)



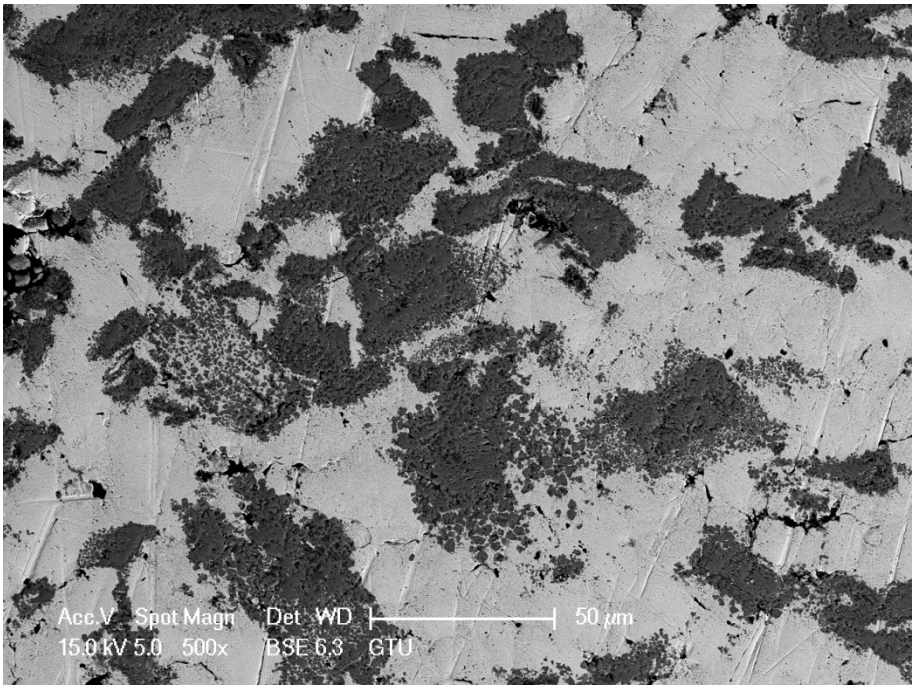
(f)

Figure 3.34. Micrographs of KB 1500-7 at a) 50X b) 500X c) 1000X d) 2000X e) 5000X and f) tipical particle sizes of TiCs at 5000X ((continuum).

Some microstructural changes were observed on the outer surfaces of cermets. These changes are mainly seen on the outer parts of the cermet as grain coarsening, formation, and enlargement of phase islets and it has been determined that especially these changes depend on the sintering temperature and the chemical composition. The ‘‘edge structure’’ was observed in cermets containing only 30% TiC sintered at 1350 ^{o}C (KB 1350-3, as seen Fig 3.35), and in compositions containing 30% and 50% TiC of cermets sintered at 1425 - 1500 ^{o}C (KB 1425-3, KB 1425-5, KB 1500-3 and KB 1500-5, as seen Fig 3.36, Fig 3.37, Fig 3.38 and Fig 3.39). When the edge structures of cermets containing 30% TiC are examined, it is seen that the increasing temperature does not only influence the size and structure of the phase islets, nevertheless helps to reduce the number and size of porosities. Due to the chemical composition difference, less enlargement of phase islands was observed in cermets containing 50% TiC than 30% TiC ones. The decrease in the porosity due to temperature increase was also observed in cermets in this composition. The various edge structures can be observed according to the temperature at which the cermet is sintered depending on the chemical composition.

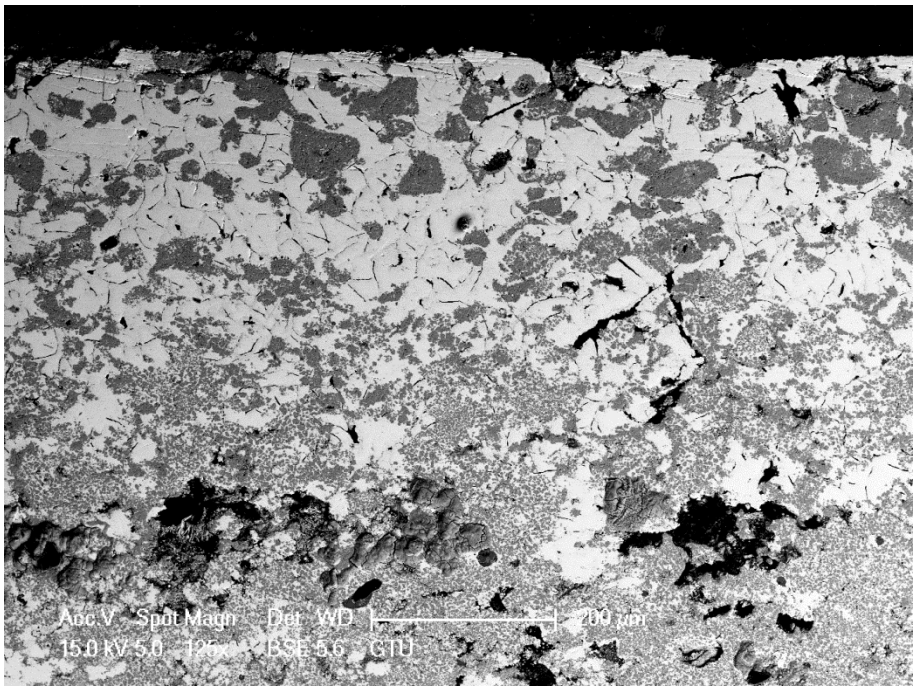


(a)

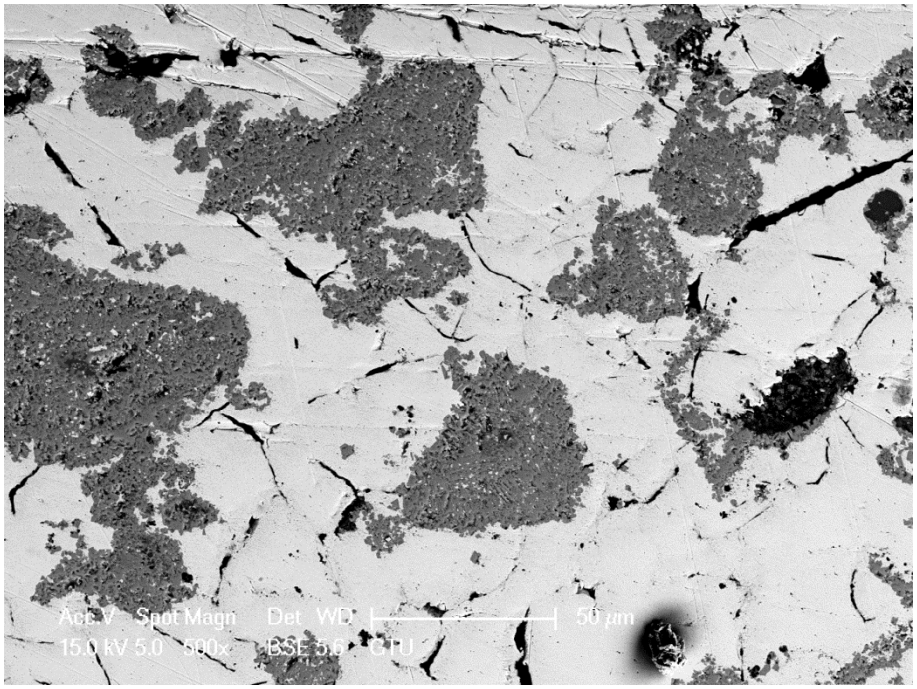


(b)

Figure 3.35. SEM micrographs from the outer surface of the KB 1350-3 at a) 125X b) 500X.

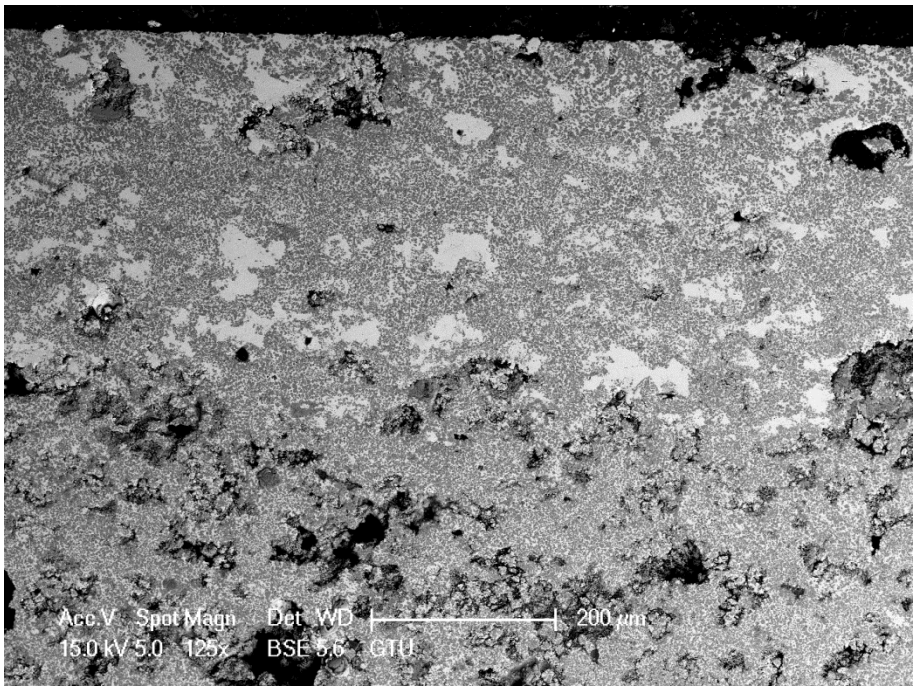


(a)

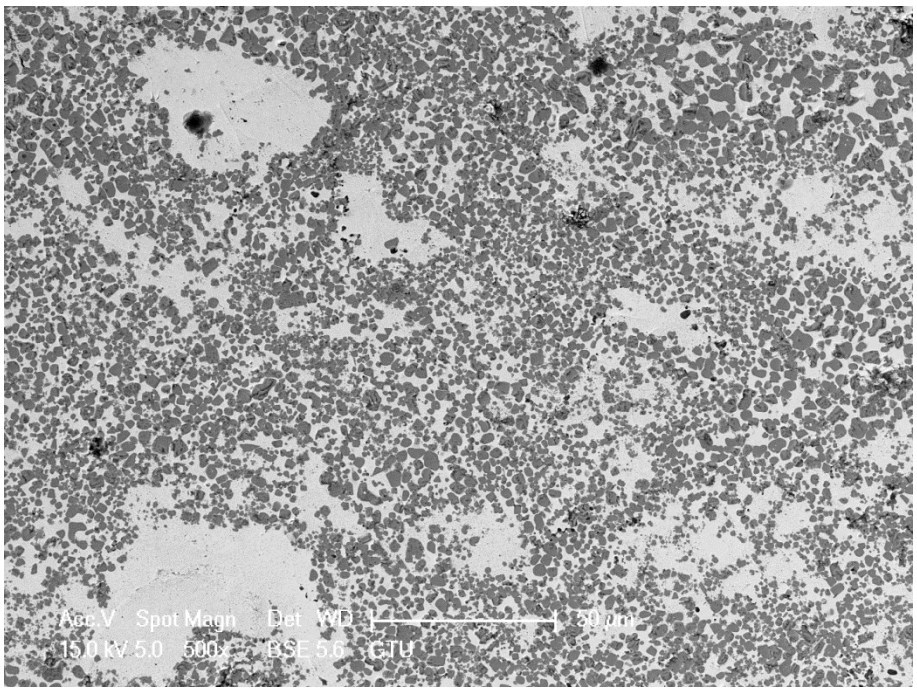


(b)

Figure 3.36. SEM micrographs from the outer surface of the KB 1425-3 at a) 125X b) 500X.

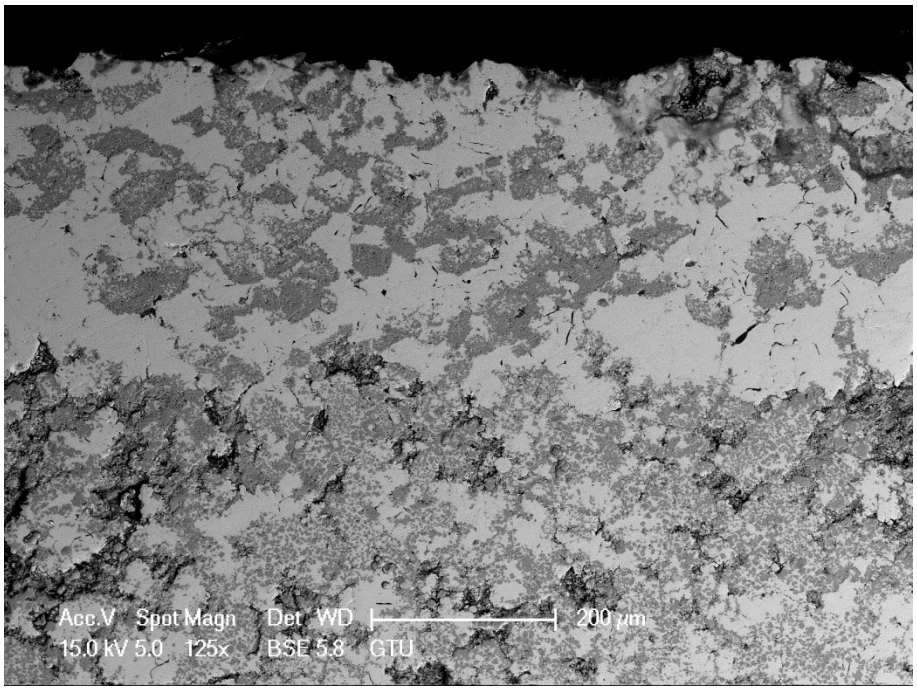


(a)

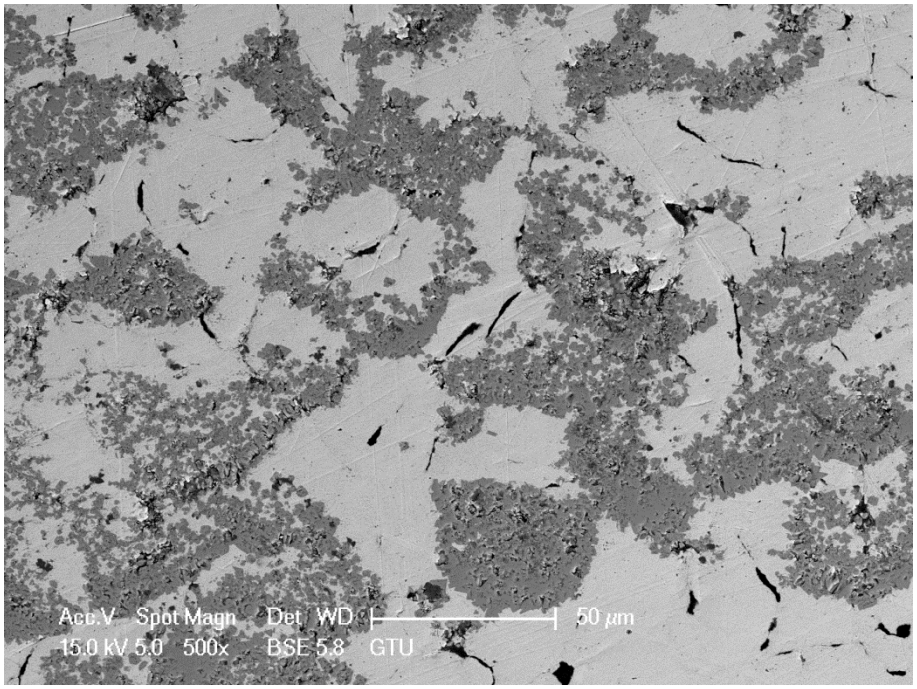


(b)

Figure 3.37. SEM micrographs from the outer surface of the KB 1425-5 at a) 125X b) 500X

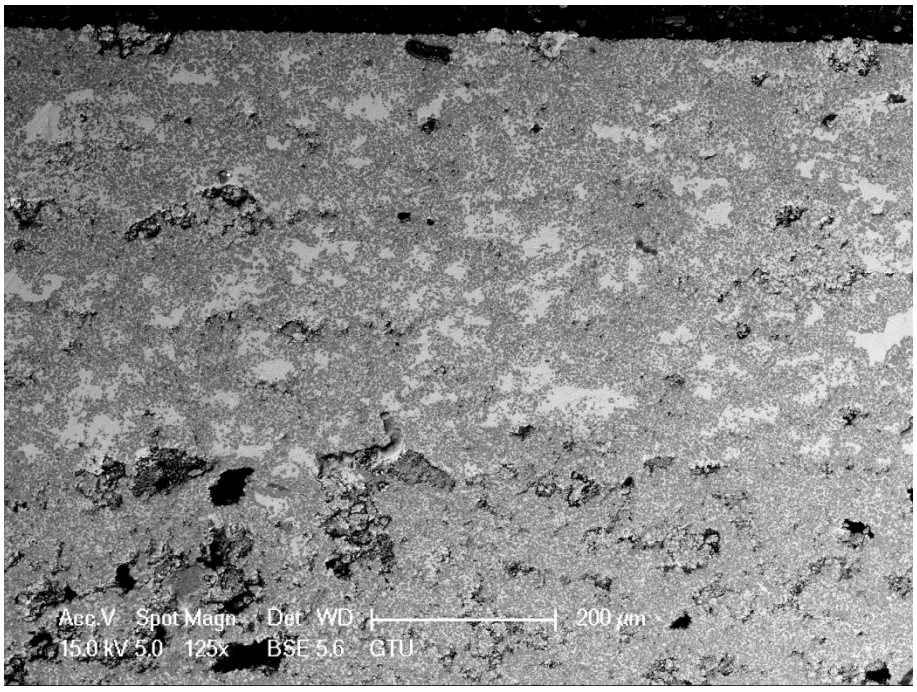


(a)

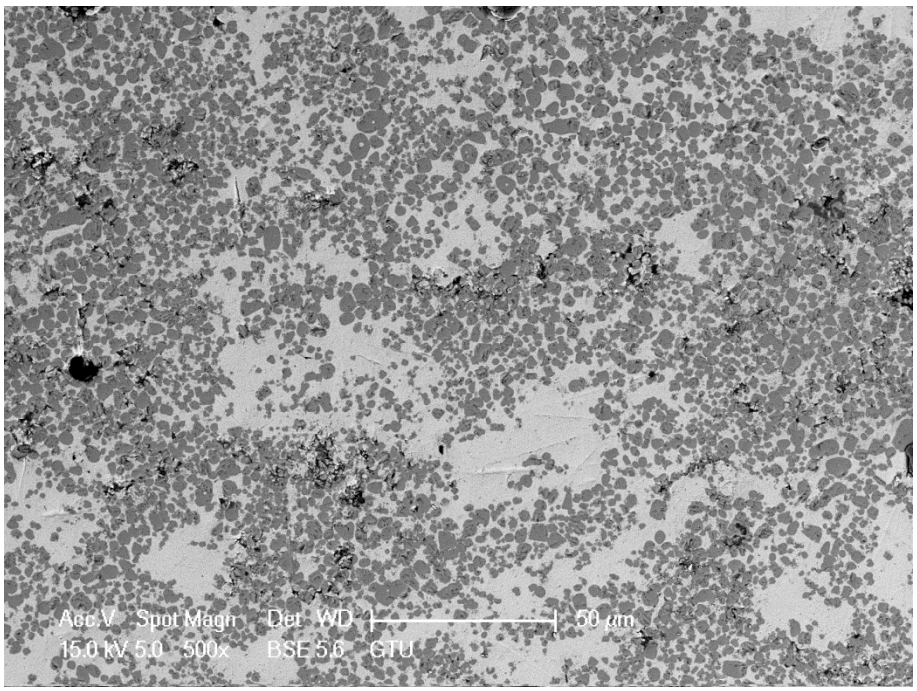


(b)

Figure 3.38. SEM micrographs from the outer surface of the KB 1500-3 at a) 125X b) 500X.



(a)



(b)

Figure 3.39. SEM micrographs from the outer surface of the KB 1500-5 at a) 125X b) 500X.

Table 3.3. Average particle sizes of TiC particles.

A.P.S. (μm)			
Sample Code	-3	-5	-7
KB 1200	1.872	2.388	2.509
KB 1275	1.900	2.111	2.811
KB 1350	1.806	2.210	3.006
KB 1425	2.344	2.061	2.965
KB 1500	2.493	2.404	2.114

Due to the decrease of the matrix in chemical composition, the increase in the average particle size of TiCs produced in-situ in cermets was determined. Increasing the amount of matrix in the cermet structure stabilizes the reaction between Ti and C. This stabilization affects the activity of the SHS reaction that takes place between Ti and C. Due to the decreasing reaction intensity, the crystallization parameters of TiC particles in the structure can change and as a result of this change, slowdown occurs in nucleation and growth processes. On the other hand, thanks to the effect of temperature on diffusion mechanism at high sintering temperatures, grain coarsening in the structure, formation, and growth of phase islands were indicated before in this study. It seems, this effect of high sintering temperature causes the invalidity of the concept which is an established relationship between the activation of reaction Ti and C and the average size of TiC particles.

Due to this negative effect of the increasing matrix metal, the percentage of Ti+C/TiC may be different between the reactant powder and the product, and the difference explained as the riched matrix by carbon. A similar situation was observed in the study conducted by Olejnik et al. As a result of their study, it was stated that when the matrix amount of cermets increased from 30% to 70%, the average particle size of TiC grains decreased from 0.8-1.6 μm to 0.4-1 μm [41]. The measured average particle sizes of in-situ TiC particles varied between 2-2.6 μm at all compositions and these values were obtained by using Ti (~ 50 μm) and graphite (~ 1 μm) with an

atomic ratio of 1:1. In the study carried out by Hu et al., the size of in-situ TiC particles obtained as the result of combustion synthesis during casting between reactants powders (28-65% FeTi (~ 25-53 μm) and graphite (~ ≤ 53 μm) were 2 μm [46]. As a result of the study using Ti (< 25 μm, % 99.50) and graphite (< 38 μm, 99.99%) powders with an atomic ratio of 1:1, Guan et al. explained that the average size of the in-situ TiC particles they obtained with the SHS method was approximately 2 μm [47].

Results showing chemical composition obtained from different phase regions by the SEM-EDS method are shown in Fig. A and Table A in Appendix A. In Table A., the chemical analysis results of all EDS points are given in percent weight and atomic ratio. The average of C/Ti ratios prepared according to the point chemical analysis taken from the areas that contain TiC as a result of the EDS analysis method is given in Table 3.4. As seen in Table 3.4., although The 1:1 atomic ratio of Ti:C was used in all cermet compositions, different stoichiometric ratios of TiC were obtained as the results of the SHS reaction. In the study published by Lee and his working group, based on the Ti-C phase equilibrium diagram, TiC can occur in a wide stoichiometric range is changing from 0.47 to 0.98 of the C/Ti ratio. It was also stated in the study that as the C/Ti value decreases, the elastic modulus and hardness value of TiC formed in-situ decreased sharply. It was explained by Lee et al., the C/Ti ratio also affects to the morphological properties of TiC. When C/Ti ≥ 0.8, spherical TiC is formed, otherwise angular TiC is formed and leads to local stress concentration. Besides, the amount of carbon over the TiC stoichiometry can dissolve in the matrix and may affect the mechanical properties of the composite structure [45]. Considering the results given in Table 3.4., it was observed that as the sintering temperature and reinforcement/matrix phase ratio increased, the ratio starting as C/Ti = 1 decreased until C/Ti = 0.5 as a result of the reaction.

Table 3.4. Average of C/Ti ratio at EDS points of TiC.

Average of C/Ti			
Samle Code	-3	-5	-7
KB 1200	1.501	1.160	0.962
KB 1275	1.009	1.231	0.868
KB 1350	0.958	0.826	0.586
KB 1425	0.725	0.807	0.749
KB 1500	0.506	0.682	0.751

The elemental distribution mapping of the KB 1500-5, which exhibits optimum properties in mechanical tests, surface examinations, and chemical analyzes, was given in Fig 3.40. The distribution of the elements on the map was measured as 1% C, 61% Ti, 38% Fe. The used reactant powders as 40 wt.% Ti, 10 wt.% C, and 50 wt.% Fe were almost equal to the distribution percentages of the elements on the mapping. Based on mapped image analysis, it can be explained that the element of Ti is homogeneously distributed in the Fe matrix, and the element C is concentrated especially in Ti-rich areas. At the same time, it is seen that some part carbon element detected in the green colored region representing the Fe matrix dissolves in the iron and forms the ferrite phase. This conclusion was reached by examining the 2Θ angles of the Fe peaks at XRD analysis.

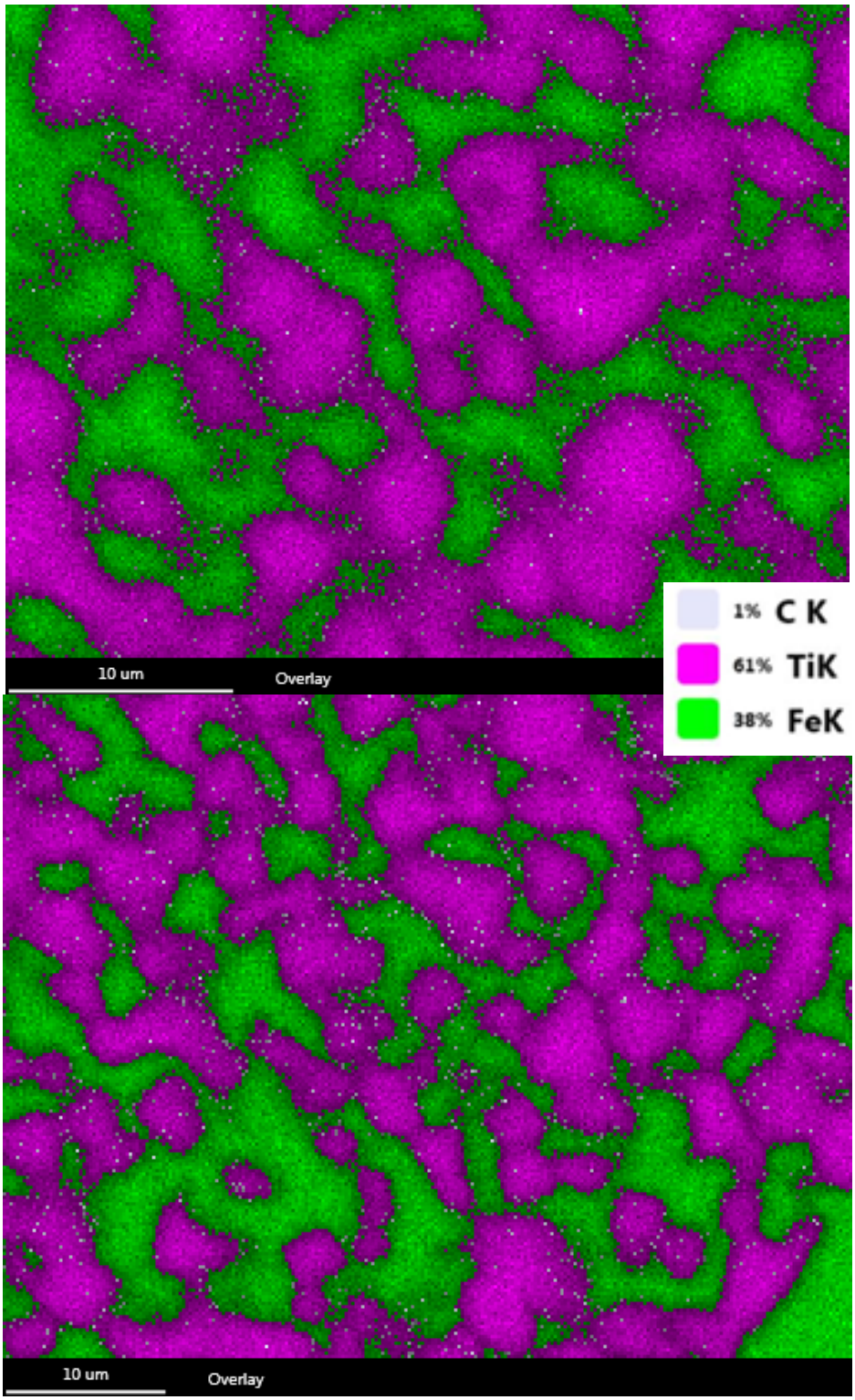


Figure 3.40. SEM-EDS results of KB 1500-5 sample in mapping mode.

4. CONCLUSION

In the scope of this thesis, reactive sintered cermet samples which have the structure of homogenous distributed in-situ TiC particles inside the iron-based matrix were produced with the result of the SHS reaction between Ti and C in different proportions. Examinations of cermets were done successfully based on aimed parameters and properties. the exhibited characteristic and structural properties of the reactive sintered cermets were summarized given below according to their chemical composition and sintering temperature. Additionally, it was touched briefly on the aspects of this study open for improvement. Finally, the advantages and suitability of the reactive sintered technique as used in the thesis in terms of industry were shortly discussed.

Predicted findings of thermochemical modeling studies were confirmed with obtained TiC as reinforcement and α-Fe as matrix phase structures on the result of sintering processes of all variations. In XRD patterns, it was determined that cermet samples were mainly composed of TiC and Fe phases and the ratio of intensities of these phases paralleled their chemical concentration ratios. It was concluded direct effects of increasing sintering temperature on measured and relative density values. The KB-1500-5 coded cermet sample is an example of the hardness and density values are balanced and the optimum mechanical properties are exhibited. Due to the decreasing matrix phase, the average particle size of the in-situ TiC particles was increased. It has been observed that the increase in temperature causes an increase in the size of TiC particles formed by the solution and precipitation mechanism. In all variations of the cermets, dimensions and shapes of formed in-situ TiC are enough suitable to provide expected mechanical properties, besides this opinion was also supported with literature. Depending on the chemical composition, grain coarsening was observed in the outer parts of some of the cermet structures when the sintering temperature is high. Theoretically, this situation is well-known to be negative on the mechanical properties, but with help of some arrangement on the sintering time and temperature, it can be useful to reduce porosity by compromising mechanical properties. With the help of SEM analysis, it has been concluded that the increasing sintering temperature has a positive effect on the decrease in the porosity amount. In the SEM-EDS results of TiC areas, although the initial ratio of C/Ti was equal to 1, it

was determined the final ratio of C/Ti ratio decreased due to the increase of the amount of reinforcement phase and the sintering temperature. Although the main reason for this situation is the dissolution of element C in the matrix, different reasons may also be effective.

The following aspects, which are related to the scope of this thesis, consider needs to improvements. A decrease in the final ratio of C/Ti can play the role in the morphological change of TiC and cause to lack of hardness. The two main reasons for lost carbon are predicted to happen as vaporization of graphite and dissolution in the matrix. Vaporization can be inhibited by using vacuum during sintering and also before the use of carbon source, the test of LOI (Loss of Ignition) can be preferred to apply. To avoid the diffusion of C and to resist alloying with C can be reasons for modifying matrix properties. Adding as excess at the beginning by calculating the amount of loss of C during sintering more precisely can be a feasible method to fix the final ratio of C/Ti to 1. Excess carbon may trigger the formation of Fe3C phases in the a-Fe matrix, which increases the hardness of the cermet but causes a sharp decrease in toughness values. Lack of densification is another aspect of this study that needs to improve. It is known that densification is influential directly on mechanical properties. Appling costly pretreatment such as mechanical alloying, turbula mixing, hot isostatic pressure (HIP), and spark plasma sintering (SPS) can provide specific benefits to reach cermet densification up to % 95. In this study, density was waived in order to make the costs suitable for bulk production, and so pretreatment processes were not applied. Liquid metal can infilter to the open porous of cermets during casting and it can help to wear resistance of positioned side of the cast. Oxidation of metallic powders may have had another detrimental effect on the mechanical properties of the cermets. Oxide particles can act as an inhibitor for reaction kinetic, and so bonds in the interface between matrix and reinforcement get weaken. Uniaxial dry mixing provides serious advantages, especially in bulk production, however, mixing under a controlled atmosphere can be helpful to obtain higher mechanical properties.

It is well known, the main advantage of reactive sintering compare to other traditional and industrial cermet production methods is needing fewer proceeding steps. Although the uncontrollable process and hard to standardizing properties are famous lacks of this technique, being cheap and suitable to bulk productions tend to occupy a large market share of wear resist tool or parts industry. Even though not

common, the examples of the cermets with excellent properties by reactive sintering are producing for metalworking, aviation, and other sophisticated industries.

REFERENCES

[1] Juhani K., (2009) Reactive Sintered Chromium and Titanium Carbide- Based Cermets, TALLINN UNIVERSITY OF TECHNOLOGY, 2009.

[2] Tjong S.., and Ma Z.Y., (2000) , "Microstructural and mechanical characteristics of in situ metal matrix composites" , Material Science and Engineering, 29 (July), 49–113.

[3] Li S.T.,Wang H.Y.,Lü S.J.,Sun S.L.,Li D.,and Jiang Q.C., (2008) , "Fabrication of steel matrix composite locally reinforced with in situ TiC particulate via SHS reaction of (Ti, Fe)-C system during casting" , ISIJ International, 48 (9), 1293–1298.

[4] Clyne T.W., (2001) Composites: Interfaces. in: Encycl. Mater. Sci. Technol., Elsevier, pp. 1382–1391.

[5] Ettmayer P., (1989) , "Hardmetals and Cermets" , Annual Review of Materials Science, 19 (1), 145–164.

[6] Prakash L., (2014) Fundamentals and General Applications of Hardmetals. Elsevier Ltd.

[7] Mari D., (2016) , "Cermets and Hardmetals" , Reference Module in Materials Science and Materials Engineering, (September 2015), 1–5.

[8] Plucknett K., (2018) , "Cermets and hardmetals" , Metals, 8 (11), 4–6.

[9] Akinribide O.J.,Obadele B.A.,Akinwamide S.O.,Bilal H.,Ajibola O.O.,Ayeleru O.O.,Ringer S.P.,and Olubambi P.A., (2019) , "Sintering of binderless TiN and TiCN-based cermet for toughness applications: Processing techniques and mechanical properties: A review" , Ceramics International, 45 (17), 21077–21090.

[10] Viljus M.,Pirso J.,Juhani K.,and Letunovitš S., (2012) , "Structure formation in Ti-C-Ni-Mo composites during reactive sintering" , Medziagotyra, 18 (1), 62–65.

[11] Tarraste M.,Juhani K.,Pirso J.,and Viljus M., (2014) , "Erosion wear of reactive sintered WC-TiC-Co cermets" , Key Engineering Materials, 604 63–66.

[12] Azadmehr A., and Taheri-Nassaj E., (2008) , "An in situ (W,Ti)C-Ni composite fabricated by SHS method" , Journal of Non-Crystalline Solids, 354 (27), 3225–3234.

[13] Korosteleva E.N.,Korzhova V. V.,and Krinitcyn M.G., (2017) , "Sintering behavior and microstructure of TiC-Me composite powder prepared by SHS" ,

Metals, 7 (8).

[14] Jõeleht M.,Pirso J.,Juhani K.,Viljus M.,and Traksmaa R., (2014) , "The formation of reactive sintered (Ti, Mo)C-Ni cermet from nanocrystalline powders" , International Journal of Refractory Metals and Hard Materials, 43 284–290.

[15] Zhao J., (2014) The use of ceramic matrix composites for metal cutting applications. Woodhead Publishing Limited.

[16] Hussainova I.,Kubarsepp J.,and Pirso J., (2001) , "Mechanical properties and features of erosion of cermets" , Wear, 250–251 (PART 1), 818–825.

[17] Humenik M., and Parikh N.M., (1954) , "Cermets: I, Fundamental Concepts Related to Micro- structure and Physical Properties of Cermet Systems" 23 37–40.

[18] Turan A.,Bugdayci M.,and Yucel O., (2015) , "Self-propagating High Temperature Synthesis of TiB2" , High Temperature Materials and Processes, 34 (2), 185–193.

[19] TURAN A., and BUĞDAYCI M., (2020) , "CoB Ön Alaşımlarının Alüminotermik Redüksiyon Yöntemiyle Üretilmesi ve Termokimyasal Modellenmesi" , El-Cezeri Fen ve Mühendislik Dergisi, 2020 (2), 436–447.

[20] Srivatsan T.S.,Sudarshan T.S.,and Lavernia E.J., (1995) Processing of discontinuously-reinforced metal matrix composites by rapid solidification.

[21] Harrigan W.C., (1998) , "Commercial processing of metal matrix composites" , Materials Science and Engineering A, 244 (1), 75–79.

[22] Sinclair I., and Gregson P.J., (1997) , "Structural performance of discontinuous metal matrix composites" , Materials Science and Technology, 13 (9), 709–726.

[23] Srivatsan T.S.,Ibrahim I.A.,Mohamed F.A.,and Lavernia E.J., (1991) , "Processing techniques for particulate-reinforced metal aluminium matrix composites" , Journal of Materials Science, 26 (22), 5965–5978.

[24] Mitra R., and Mahajan Y.R., (1995) , "Interfaces in discontinuously reinforced metal matrix composites: An overview" , Bulletin of Materials Science, 18 (4), 405–434.

[25] Arsenault R.J., (1993) , "Strengthening and deformation mechanisms of discontinuous metal matrix composites" , Proceedings of the International Conference on Advanced Composite Materials, 80 19–27.

[26] McKimpson M.G., and Scott T.E., (1989) , "Processing and properties of metal matrix composites containing discontinuous reinforcement" , Materials Science and Engineering A, 107 (c), 93–106.

[27] Koczak M.J., and Premkumar M.K., (1993) , “Emerging technologies for the in-situ production of MMCs” , Jom, 45 (1), 44–48.

[28] Bugdayci M.,Alkan M.,Turan A.,and Yücel O., (2018) , “Production of Iron Based Alloys from Mill Scale through Metallothermic Reduction” , High Temperature Materials and Processes, 37 (9–10), 889–898.

[29] Borovinskaya I.P.,Merzhanov A.G.,Novikov N.P.,and Filonenko A.K., (1974) , “Gasless combustion of mixtures of powdered transition metals with boron” , Combustion, Explosion, and Shock Waves, 10 (1), 2–10.

[30] CORBIN N.D., and McCAULEY J.W., (1986) , “Self-Propagating High-Temperature Synthesis (Shs): Current Status and Future Prospects.”

[31] Holt J.B., and Munir Z.A., (1986) , “Combustion synthesis of titanium carbide: Theory and experiment” , Journal of Materials Science, 21 (1), 251–259.

[32] Munir Z.A., and Lai W., (1993) , “The SHS Diagram for TiC” , Combustion Science and Technology, 88 (3–4), 201–209.

[33] Prabu R.,Ramesh S.,and Karunamoorthy L., (2016) , “4965 structure and properties of laser coated tic on ss316”.

[34] Pirso J.,Viljus M.,and Letunovitš S., (2006) , “Friction and dry sliding wear behaviour of cermets” , Wear, 260 (7–8), 815–824.

[35] Alvaredo P.,Mari D.,and Gordo E., (2013) , “High temperature transformations in a steel-TiCN cermet” , International Journal of Refractory Metals and Hard Materials, 41 115–120.

[36] Koc R., (1998) , “Kinetics and phase evolution during carbothermal synthesis of titanium carbide from ultrafine titania/carbon mixture” , Journal of Materials Science, 33 (4), 1049–1055.

[37] Raghunath C.,Bhat M.S.,and Rohatgi P.K., (1995) , “In situ technique for synthesizing Fe-TiC Composites” , Scripta Metallurgica et Materialia, 32 (4), 577–582.

[38] Jõeleht M.,Pirso J.,Juhani K.,Viljus M.,and Traksmaa R., (2015) , “The influence of high energy milling and sintering parameters on reactive sintered (Ti, Mo)C-Ni cermets” , Journal of Alloys and Compounds, 636 381–386.

[39] Ding L.,Xiang D.P.,Pan Y.L.,Zhang T.M.,and Wu Z.Y., (2016) , “In situ synthesis of TiC cermet by spark plasma reaction sintering” , Journal of Alloys and Compounds, 661 136–140.

[40] Wang Jing, and Wang Yisan, (2007) , “In-situ production of Fe-TiC composite” , Materials Letters, 61 (22), 4393–4395.

[41] Olejnik E.,Szymański,Batóg P.,Tokarski T.,and Kurtyka P., (2020) , “TiC-

FeCr local composite reinforcements obtained in situ in steel casting" , Journal of Materials Processing Technology, 275 (AOlejnik, E., Szymański, Batóg, P., Tokarski, T., Kurtyka, P. (2020). TiC-FeCr local composite reinforcements obtained in situ in steel casting. Journal of Materials Processing Technology, 275(April 2018), 116157. https://doi.org/10.1016/j.jmatprotec.20), 116157.

[42] Zhu H.,Dong K.,Wang H.,Huang J.,Li J.,and Xie Z., (2013) , "Reaction mechanisms of the TiC/Fe composite fabricated by exothermic dispersion from Fe-Ti-C element system" , Powder Technology, 246 456–461.

[43] Li B.,Liu Y.,Cao H.,He L.,and Li J., (2009) , "Rapid fabrication of in situ TiC particulates reinforced Fe-based composites by spark plasma sintering" , Materials Letters, 63 (23), 2010–2012.

[44] Yang Y.F.,Wang H.Y.,Liang Y.H.,Zhao R.Y.,and Jiang Q.C., (2008) , "Effect of C particle size on the porous formation of TiC particulate locally reinforced steel matrix composites via the SHS reaction of Ni-Ti-C system during casting" , Materials Science and Engineering A, 474 (1–2), 355–362.

[45] Lee J.,Lee D.,Song M.H.,Rhee W.,Ryu H.J.,and Hong S.H., (2018) , "In-situ synthesis of TiC/Fe alloy composites with high strength and hardness by reactive sintering" , Journal of Materials Science and Technology, 34 (8), 1397–1404.

[46] Hu S.W.,Zhao Y.G.,Wang Z.,Li Y.G.,and Jiang Q.C., (2013) , "Fabrication of in situ TiC locally reinforced manganese steel matrix composite via combustion synthesis during casting" , Materials and Design, 44 340–345.

[47] GUAN Q.F.,JIANG Q.J.,ZHAO Y.Q.,and LIU C.H., (2002) , "In Situ Production of Fe–TiC Composites by Self-propagative High-temperature Synthesis Reaction in Liquid Iron Alloy" , ISIJ International, 42 (6), 673–675.

BIOGRAPHY

I, Mammadhuseyn MAMMADZADA, was born on September 1, 1993 in Baku, Azerbaijan. In 2016, I completed my bachelor's degree in Metallurgy and Materials Engineering at Istanbul Technical University.

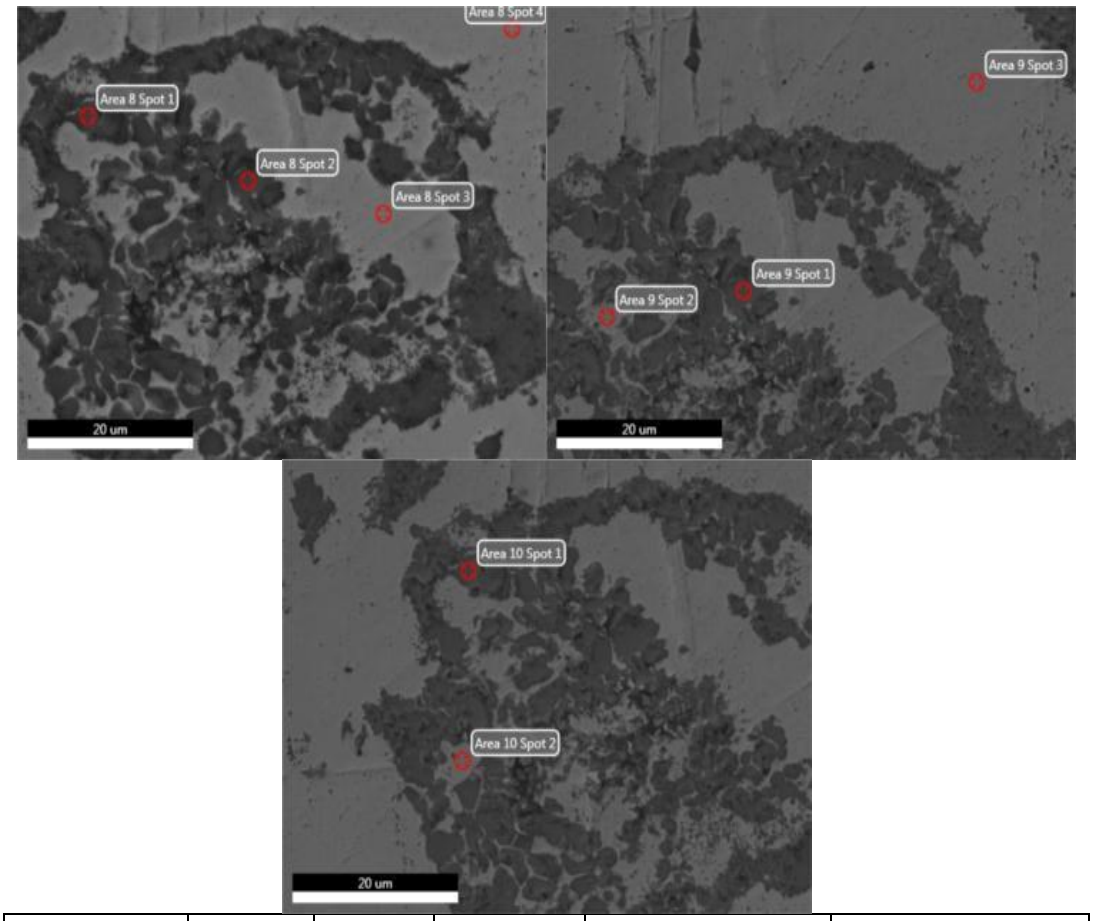
At same year, I started working in the company of KÖRFEZ DÖKÜM A.Ş. I am currently working in the R&D unit of same company as a senior engineer. I was active participate in the development and commercialization of various ceramic reinforced steel matrix composites conducted our company. I also undertaked important tasks in R & D and manufacturing processes of the TUBITAK supported project of " TiC-based steel matrix cermets" which commercially performed first time in Turkey.

In 2017, I started the Materials Science and Engineering master program at the Institute of Natural and Applied Sciences of Gebze Technical University. I am continuing my graduate education under the supervision of Prof. Dr. Mehmet TARAKÇI. During my graduate education, I have been studing on extending the wear life of steel cast parts with ceramic reinforcements, especially on obtaining with the TiC reinforcement phase during the casting process.

APPENDICES

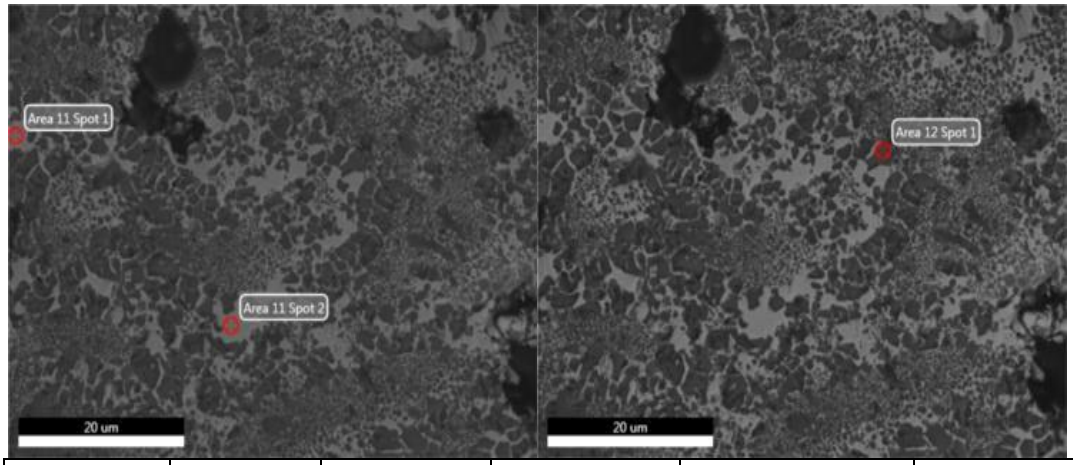
Appendix A: Chemical analysis results obtained from cermet samples with SEM EDS technique and SEM micrographs of analyzed points

Table A. Chemical compositions of SEM-EDS analysis points.

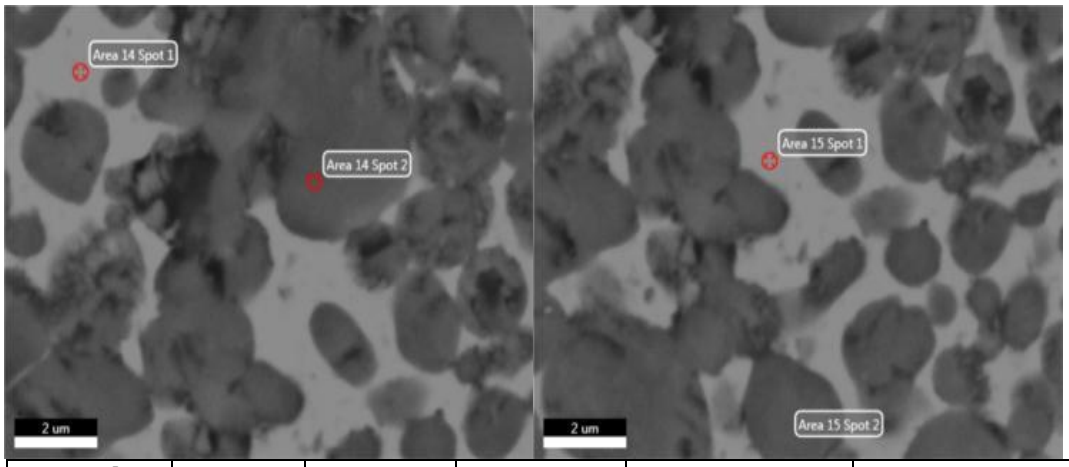


Sample Code	Area No:	Spot No:	Element	Weight (%)	Atomic (%)
KB 1200-3	8	1	C	17.72	48.38
			Ti	33.88	23.2
			Fe	48.4	28.42
		2	C	12.8	37.23
			Ti	79.38	57.88
			Fe	7.82	4.89
		3	C	4.93	19.24
			Ti	6.93	6.78
			Fe	88.14	73.98
		4	C	4.44	17.73
			Ti	1.16	1.16
			Fe	94.4	81.11
	9	1	C	15.08	41.55
			Ti	82.68	57.13
			Fe	2.24	1.33

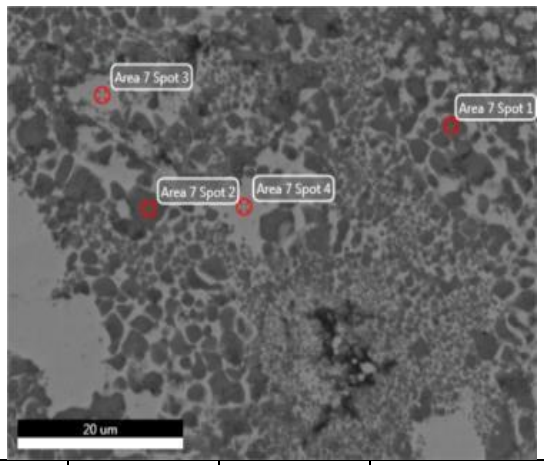
		2	C	18.01	48.76
			Ti	36.21	24.59
			Fe	45.78	26.66
		3	C	7.87	28.39
			Ti	0.85	0.77
			Fe	91.28	70.84
	10	1	C	15.46	42.26
			Ti	82.27	56.4
			Fe	2.27	1.33
		2	C	7.47	26.97
			Ti	9.26	8.38
			Fe	83.28	64.66



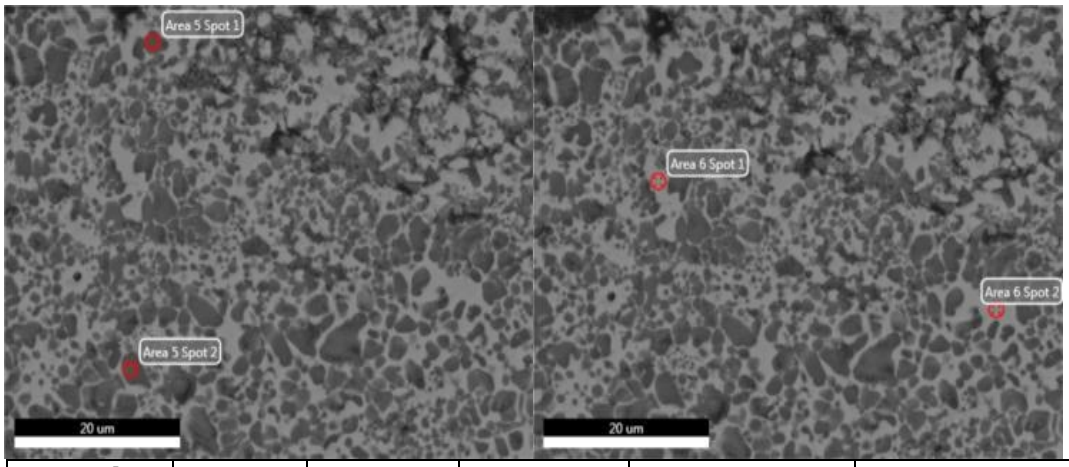
Sample Code	Area No:	Spot No:	Element	Weight (%)	Atomic (%)
KB 1200-5	11	1	C	7.26	26.58
			Ti	3.06	2.81
			Fe	89.68	70.61
		2	C	8.43	29.86
			Ti	2.76	2.45
			Fe	88.81	67.69
	12	1	C	21.07	51.89
			Ti	71.86	44.37
			Fe	7.07	3.74



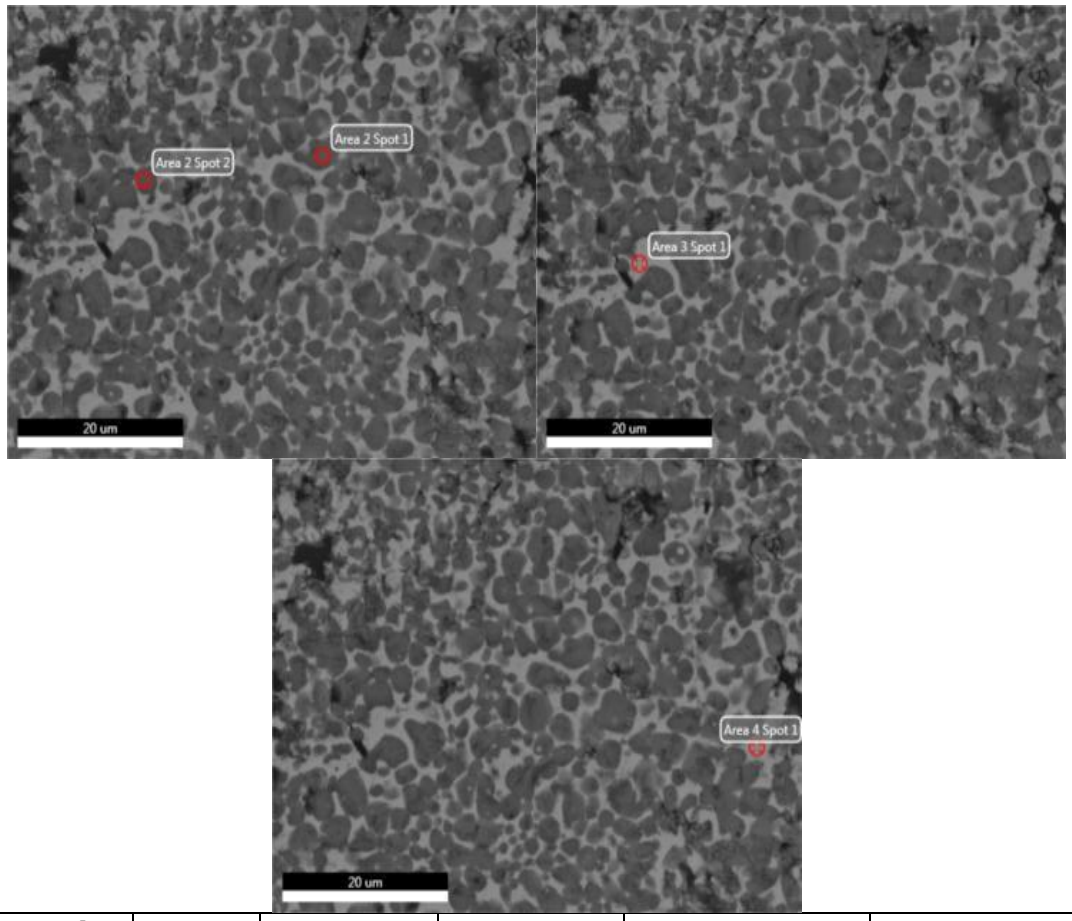
Sample Code	Area No:	Spot No:	Element	Weight (%)	Atomic (%)
KB 1200-7	14	1	C	5.13	19.96
			Ti	5.04	4.92
			Fe	89.83	75.13
		2	C	19.58	49.31
			Ti	79.55	50.22
			Fe	0.87	0.47
	15	1	C	18.83	48.12
			Ti	79.82	51.14
			Fe	1.35	0.74
		2	C	18.83	48.12
			Ti	79.82	51.14
			Fe	1.35	0.74



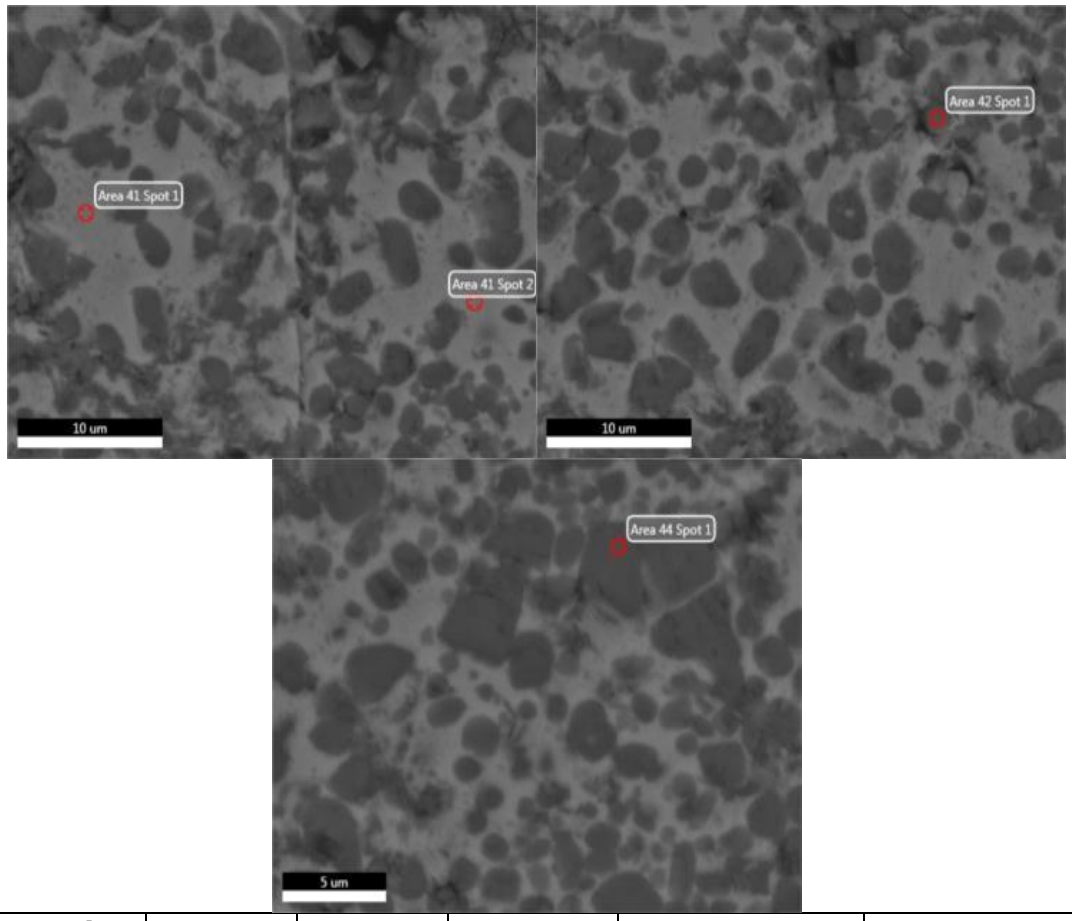
Sample Code	Area No:	Spot No:	Element	Weight (%)	Atomic (%)
KB 1275-3	7	1	C	16.99	46.09
			Ti	56.57	38.48
			Fe	26.44	15.42
		2	C	15.4	42.43
			Ti	75.61	52.24
			Fe	8.99	5.33
		3	C	6.35	23.67
			Ti	9.68	9.05
			Fe	83.96	67.28
		4	C	4.12	16.56
			Ti	3.78	3.81
			Fe	92.1	79.63



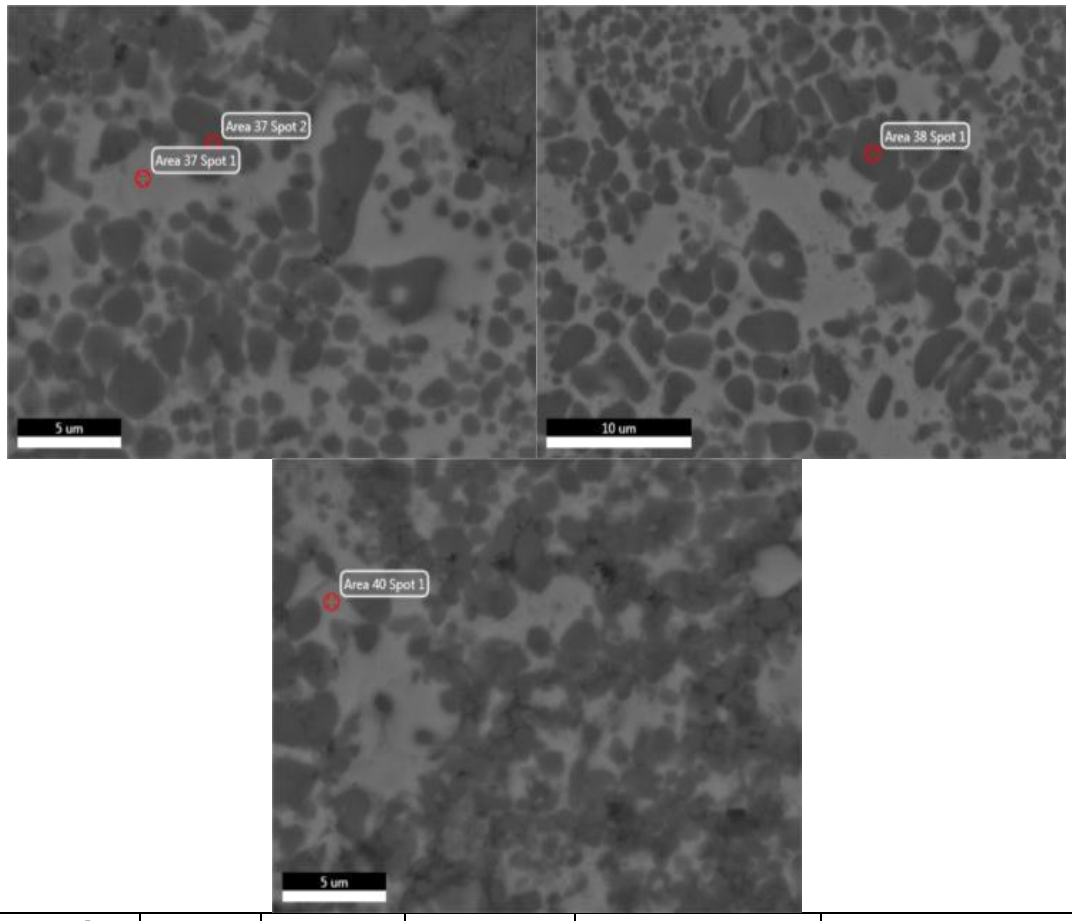
Sample Code	Area No:	Spot No:	Element	Weight (%)	Atomic (%)
KB 1275-5	5	1	C	18.03	48.08
			Ti	51.65	34.53
			Fe	30.32	17.38
		2	C	18.62	48.24
			Ti	69.39	45.08
			Fe	11.99	6.68
	6	1	C	9.07	31.18
			Ti	13.1	11.29
			Fe	77.83	57.54
		2	C	11.38	36.97
			Ti	9.73	7.92
			Fe	78.89	55.11



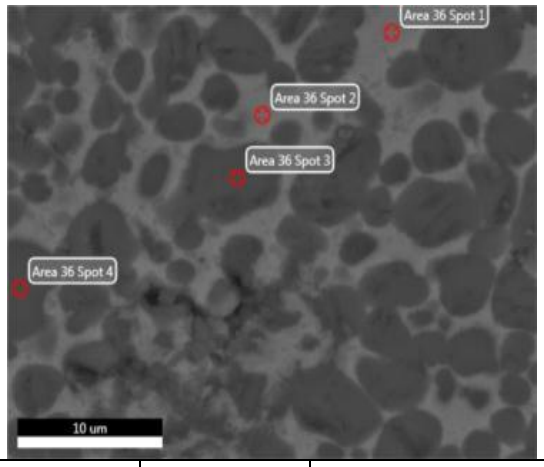
Sample Code	Area No:	Spot No:	Element	Weight (%)	Atomic (%)
KB 1275-7	2	1	C	14.82	41.49
			Ti	72.37	50.8
			Fe	12.81	7.71
		2	C	13.74	39.92
			Ti	59.62	43.44
			Fe	26.64	16.64
	3	1	C	4.81	18.86
			Ti	5.82	5.73
			Fe	89.37	75.41
	4	1	C	6.99	25.54
			Ti	10.26	9.4
			Fe	82.76	65.06



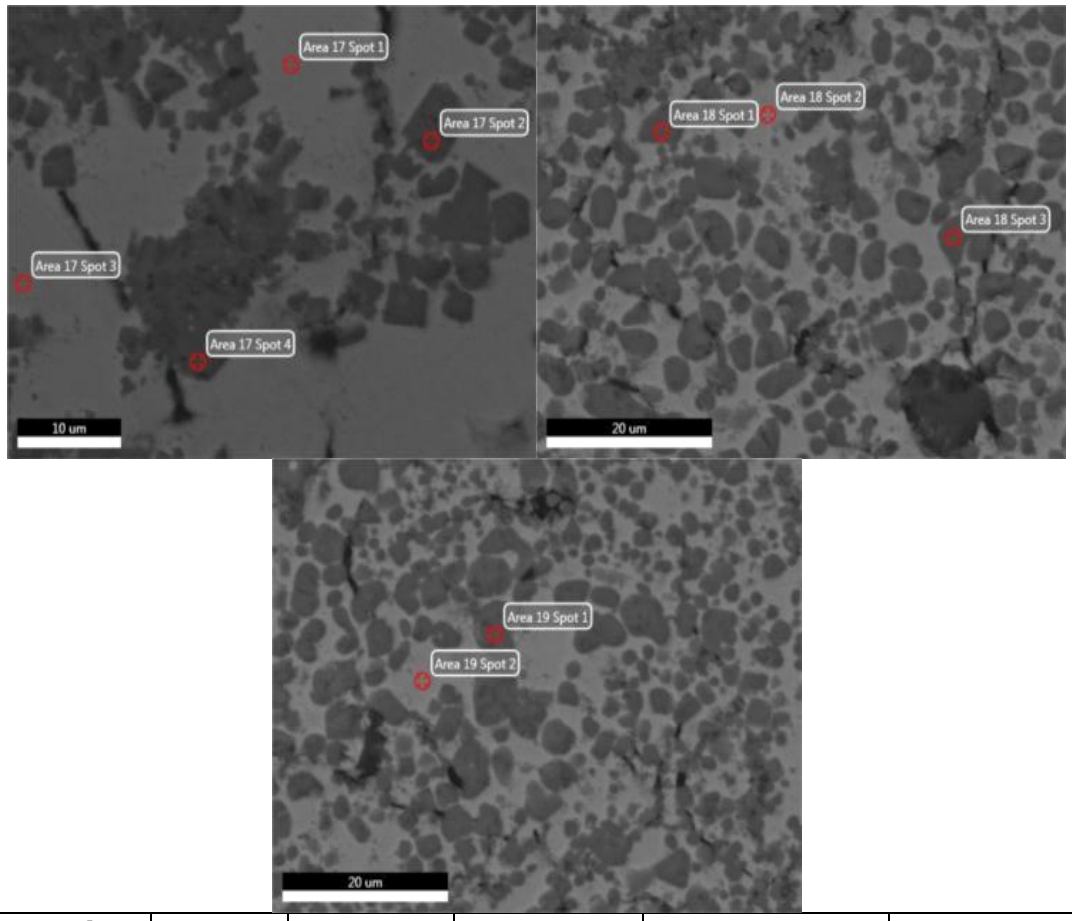
Sample Code	Area No:	Spot No:	Element	Weight (%)	Atomic (%)
KB 1350-3	41	1	C	4.87	19.11
			Ti	4.68	4.6
			Fe	90.45	76.29
		2	C	5.33	20.42
			Ti	11.01	10.59
			Fe	83.66	68.99
	42	1	C	17.63	46.94
			Ti	62.02	41.41
			Fe	20.35	11.65
	44	1	C	15.79	43.13
			Ti	76.09	52.1
			Fe	8.12	4.77



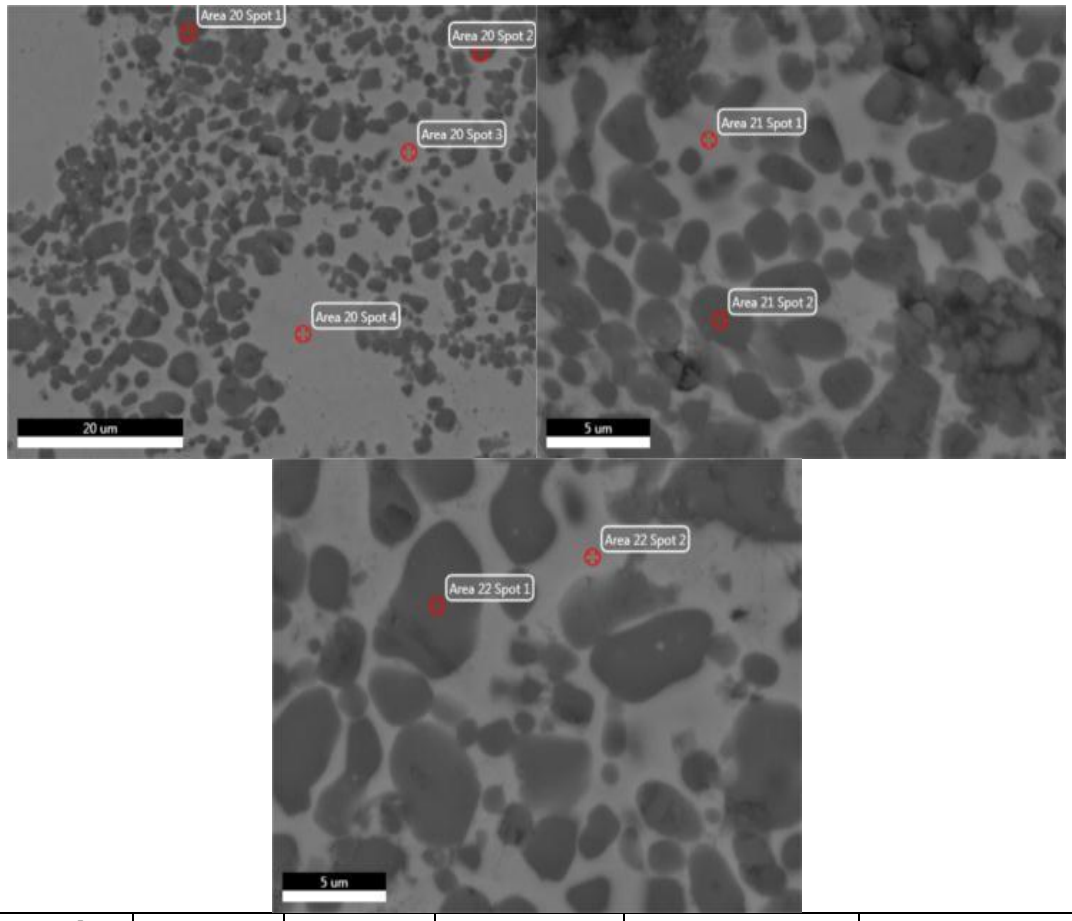
Sample Code	Area No:	Spot No:	Element	Weight (%)	Atomic (%)
KB 1350-5	37	1	C	7.01	25.78
			Ti	5.12	4.72
			Fe	87.87	69.5
		2	C	14.03	40.36
			Ti	62.79	45.3
			Fe	23.18	14.34
	38	1	C	14.09	40.02
			Ti	73.87	52.62
			Fe	12.04	7.36
	40	1	C	10.11	33.97
			Ti	8.76	7.38
			Fe	81.13	58.65



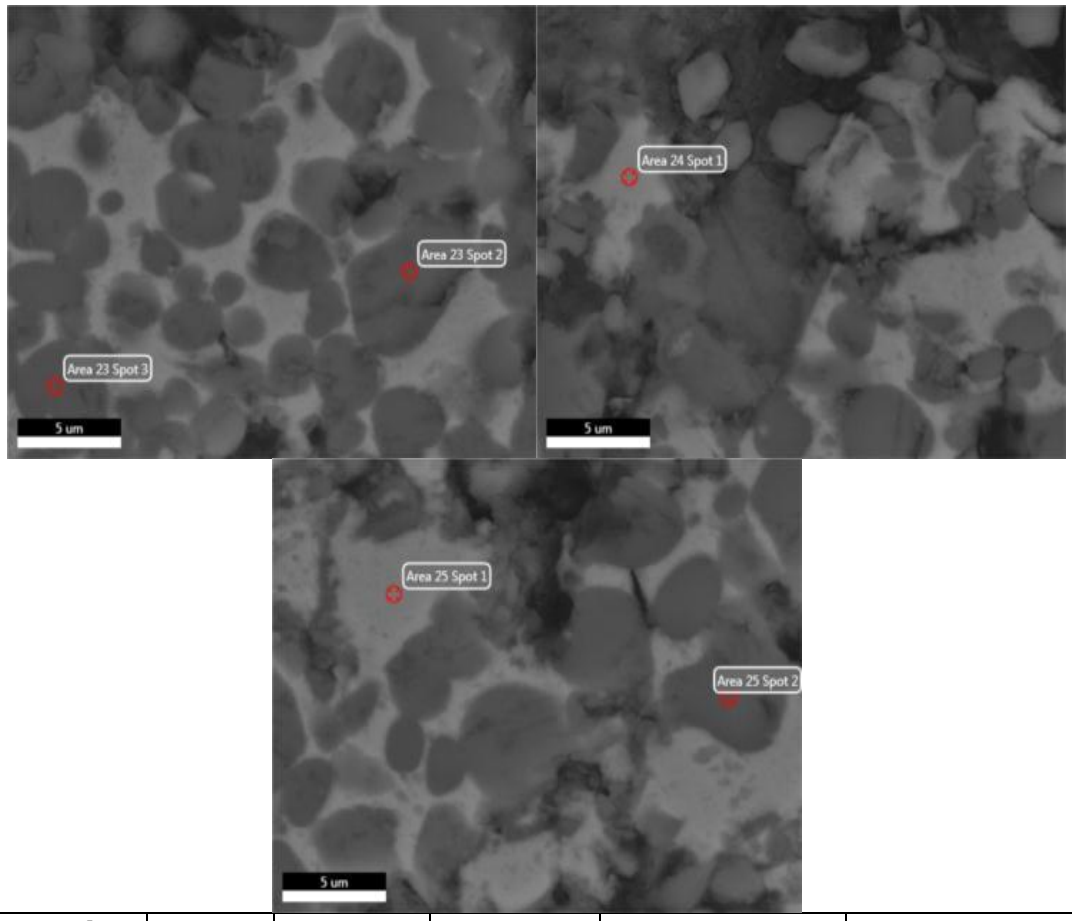
Sample Code	Area No:	Spot No:	Element	Weight (%)	Atomic (%)
KB 1350-7	36	1	C	7.29	26.57
			Ti	5.47	5
			Fe	87.24	68.42
		2	C	6.11	22.99
			Ti	8.05	7.59
			Fe	85.83	69.42
		3	C	10.62	32.6
			Ti	76.43	58.84
			Fe	12.95	8.55
		4	C	13	37.45
			Ti	84.09	60.74
			Fe	2.91	1.8



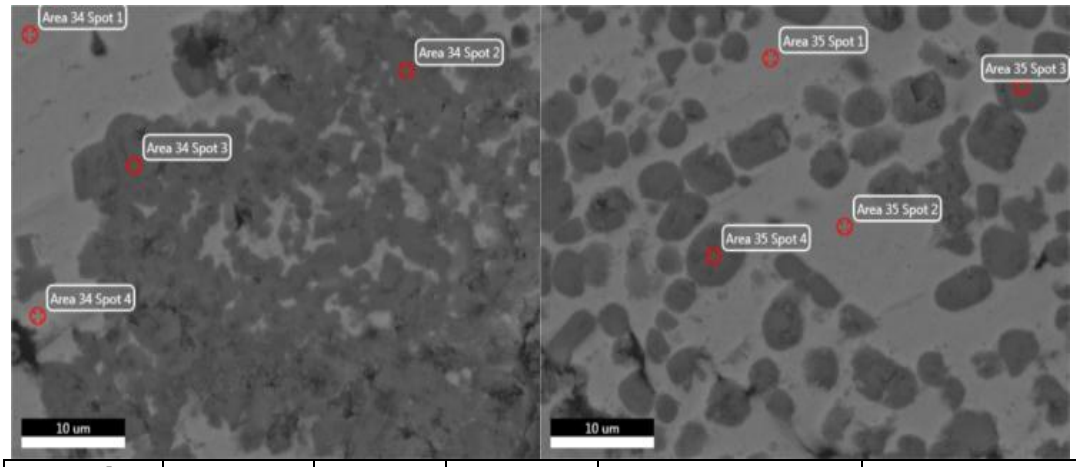
Sample Code	Area No:	Spot No:	Element	Weight (%)	Atomic (%)
KB 1425-3	17	1	C	4.01	16.24
			Ti	1.64	1.66
			Fe	94.35	82.1
		2	C	13.52	38.96
			Ti	72.39	52.31
			Fe	14.09	8.73
		3	C	4.33	17.35
			Ti	1.41	1.41
			Fe	94.26	81.24
		4	C	13.18	38.22
			Ti	73.64	53.56
			Fe	13.19	8.23
	18	1	C	15.09	42.22
			Ti	67.02	47.02
			Fe	17.89	10.76
		2	C	4.42	17.62
			Ti	2.34	2.35
			Fe	93.24	80.03
		3	C	12.26	36.06
			Ti	80.56	59.4
			Fe	7.18	4.54
	19	1	C	13.13	37.91
			Ti	79.19	57.32
			Fe	7.68	4.77
		2	C	3.86	15.66
			Ti	2.7	2.75
			Fe	93.44	81.59



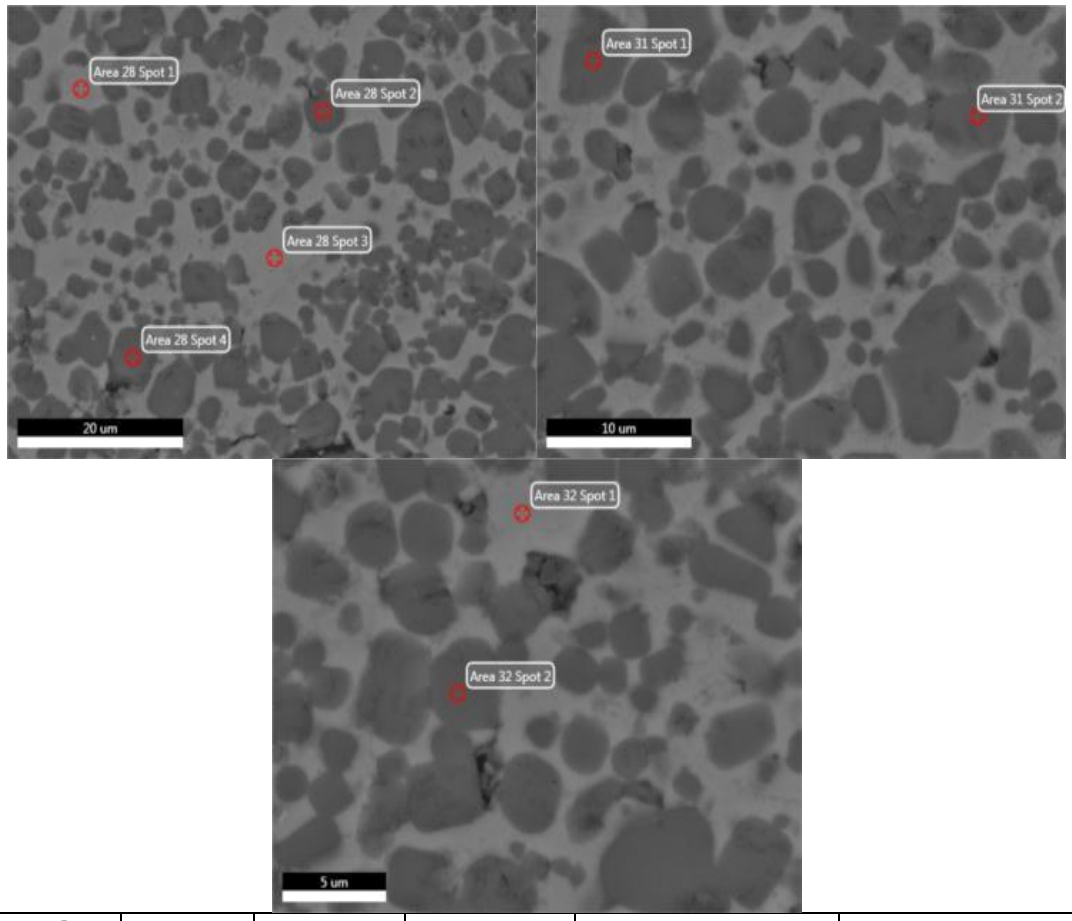
Sample Code	Area No:	Spot No:	Element	Weight (%)	Atomic (%)
KB 1425-5	20	1	C	11.64	34.65
			Ti	82.43	61.55
			Fe	5.93	3.8
		2	C	14.06	40.32
			Ti	65.22	46.9
			Fe	20.72	12.78
		3	C	6.96	25.63
			Ti	5.05	4.66
			Fe	88	69.71
		4	C	4.45	17.75
			Ti	1.6	1.6
			Fe	93.95	80.65
	21	1	C	14.8	41.86
			Ti	62.59	44.39
			Fe	22.61	13.76
		2	C	13.81	39.87
			Ti	64.13	46.43
			Fe	22.06	13.7
	22	1	C	14.64	41.17
			Ti	71.9	50.7
			Fe	13.46	8.14
		2	C	7.97	28.56
			Ti	4.03	3.62
			Fe	88.01	67.83



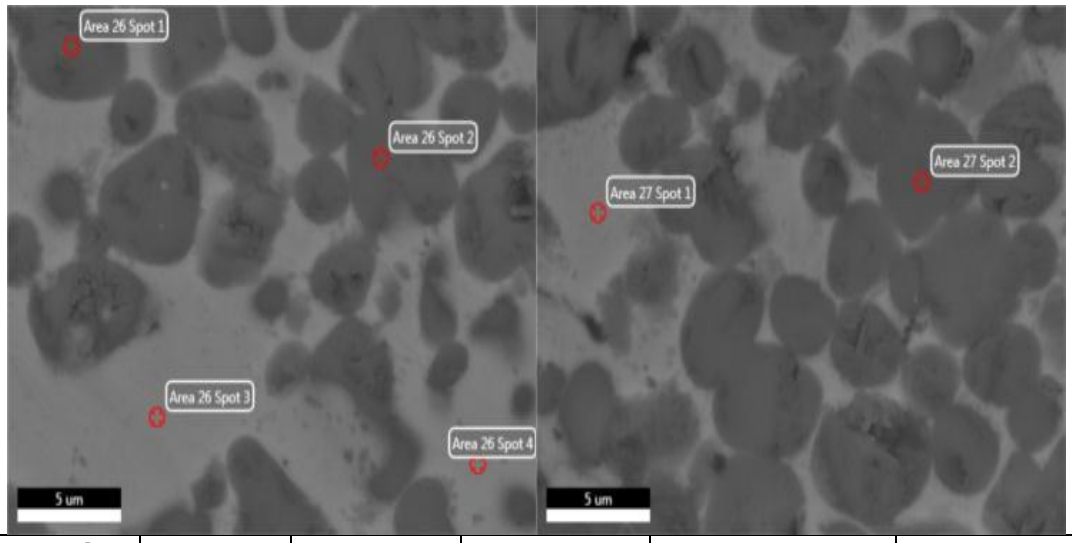
Sample Code	Area No:	Spot No:	Element	Weight (%)	Atomic (%)
KB 1425-7	23	1	C	14.95	41.41
			Ti	80.02	55.59
			Fe	5.03	3
		2	C	14.86	41.18
			Ti	81.44	56.61
			Fe	3.7	2.21
	24	1	C	5.57	21.34
			Ti	6.24	6
			Fe	88.19	72.66
	25	1	C	4.66	18.41
			Ti	4.25	4.21
			Fe	91.09	77.38
		2	C	15.69	42.74
			Ti	80.86	55.24
			Fe	3.45	2.02



Sample Code	Area No:	Spot No:	Element	Weight (%)	Atomic (%)
KB 1500-3	34	1	C	4.07	16.46
			Ti	1.03	1.04
			Fe	94.9	82.5
		2	C	10.83	32.75
			Ti	85.54	64.89
			Fe	3.63	2.36
		3	C	11.02	33.14
			Ti	86.93	65.54
			Fe	2.04	1.32
		4	C	6.35	23.92
			Ti	1.38	1.31
			Fe	92.27	74.77
	35	1	C	3.12	12.98
			Ti	2.47	2.58
			Fe	94.41	84.44
		2	C	2.68	11.31
			Ti	2.02	2.14
			Fe	95.3	86.55
		3	C	7.36	24.2
			Ti	87.61	72.24
			Fe	5.03	3.56
		4	C	6.92	23.01
			Ti	87.51	73
			Fe	5.57	3.99



Sample Code	Area No:	Spot No:	Element	Weight (%)	Atomic (%)
KB 1500-5	28	1	C	3.96	16.01
			Ti	3.25	3.3
			Fe	92.79	80.69
		2	C	12.3	36.03
			Ti	83.22	61.15
			Fe	4.48	2.82
		3	C	4.73	18.67
			Ti	2.68	2.65
			Fe	92.6	78.68
		4	C	10.9	32.86
			Ti	86.81	65.65
			Fe	2.29	1.49
	31	1	C	13.63	39.06
			Ti	75.59	54.3
			Fe	10.77	6.64
		2	C	14.18	40.35
			Ti	70.22	50.1
			Fe	15.6	9.55
	32	1	C	6.37	23.85
			Ti	5.6	5.25
			Fe	88.03	70.89
		2	C	13.31	38.56
			Ti	71.68	52.08
			Fe	15.02	9.36



Sample Code	Area No:	Spot No:	Element	Weight (%)	Atomic (%)
KB 1500-7	26	1	C	14.61	41.02
			Ti	74.12	52.17
			Fe	11.27	6.81
		2	C	13.99	39.61
			Ti	79.41	56.37
			Fe	6.6	4.02
		3	C	4.64	18.37
			Ti	3.27	3.25
			Fe	92.09	78.38
		4	C	3.89	15.68
			Ti	7.67	7.74
			Fe	88.44	76.58
	27	1	C	4.17	16.71
			Ti	4.29	4.31
			Fe	91.55	78.98
		2	C	14.47	40.7
			Ti	75.43	53.19
			Fe	10.1	6.11